DISSERTATION

SIMULTANEOUS FOUR-WAVE MIXING AND STIMULATED RAMAN SPECTROSCOPY: STARK AND DOPPLER BROADENING

Submitted by

Hans Moosmüller

Department of Physics

In partial fulfillment of the requirements

for the Degree of Doctor of Philosophy

Colorado State University

Fort Collins, Colorado

Summer 1988

COLORADO STATE UNIVERSITY

MAY 24, 1988

WE HEREBY RECOMMEND THAT THE DISSERTATION PREPARED UNDER OUR SUPERVISION BY HANS MOOSMÜLLER ENTITLED "SIMULTANEOUS FOUR-WAVE MIXING AND STIMULATED RAMAN SPECTROSCOPY: STARK AND DOPPLER BROADENING" BE ACCEPTED AS FULFILLING IN PART REQUIREMENTS FOR THE DEGREE OF DOCTOR OF PHILOSOPHY.

Committee on Graduate Work

Adviser

Department Head

ABSTRACT OF DISSERTATION

SIMULTANEOUS FOUR-WAVE MIXING AND STIMULATED RAMAN SPECTROSCOPY: STARK AND DOPPLER BROADENING

Spectral line shapes obtained with four-wave mixing Raman spectroscopy (FWMRS) and stimulated Raman spectroscopy (SRS) are investigated experimentally and theoretically. While both techniques are commonly used as high-resolution spectroscopies, the systematic differences in their spectra have not been well explored. Using an experimental setup capable of simultaneous measurement of coherent Stokes Raman spectroscopy and inverse Raman spectroscopy spectra, we are able to perform a direct comparison between both classes of Raman spectroscopies and to reveal even minor differences in the resulting spectra. Experimental spectra of several lines in the vibrational Q-branch of molecular nitrogen (N_2) are obtained for different experimental conditions. At low pump intensities, after deriving the effect of Doppler broadening in these spectroscopies and taking the influence of neighboring lines into account, we are able to explain why FWMRS yields broader lines with peaks shifted relative to the peaks of SRS.

At high pump intensities, we investigate the influence of optical Stark effect in focused Gaussian beams on both types of coherent Raman spectroscopy. Our experimental results demonstrate that SRS spectra

show more Stark shift and broadening than their FWMRS counterparts. Our theory of signal generation in focused Gaussian beams leads to the calculation of theoretical Stark broadened spectra for both spectroscopies. While SRS spectra show excellent agreement with the theoretical calculations, simultaneously measured FWMRS spectra do not perfectly agree with our theory. We demonstrate that this discrepancy can be partly reconciled by the inclusion of a resonant fifth-order process in the previously third-order theory of FWMRS. Additionally we discuss the theory of phase modulation induced by rapid Stark tuning of molecular transition frequencies and its influence on both types of coherent Raman spectroscopy. We further suggest possible experiments to test our theory.

Hans Moosmüller
Department of Physics
Colorado State University
Fort Collins, CO 80523
Summer 1988

Acknowledgements

While a Ph.D. thesis commonly has only one author, it is understood that many people contribute to its content, and I would like to mention at least a few of them. First of all I want to thank my adviser and mentor Prof. C.Y. She, who guided me through the lengthy process of finishing this dissertation. He used to come up with brilliant ideas, whenever I was stuck. Professors D.A. Krueger and S.B. Anderson helped a great deal in translating my usual hand waving arguments into mathematical formulas. Dr. G.C. (Zippy) Herring introduced me to the experimental aspects of coherent Raman spectroscopy. Furthermore, it is a pleasure to thank all members of my graduate committee for a critical reading of my dissertation and their signatures.

Table of Contents

Chapter 1

Introduction

1.1 Introduction

Since the first utilization of coherent Raman scattering as a general spectroscopic technique in 1974 [1.1], different kinds of coherent Raman spectroscopy (CRS) have been developed. These techniques offer dramatic advantages over spontaneous Raman scattering in terms of signal strength, spectral resolution and suppression of background light. They have been used extensively for spectroscopic and diagnostic purposes [1.2, 1.3].

We distinguish between two classes of two-beam CRS's. In four-wave mixing, which shows resonance enhancement when the difference frequency of the two laser beams coincides with the frequency of a Raman transition, one observes either Stokes shifted output, or simultaneously emitted anti-Stokes shifted output, corresponding to coherent Stokes Raman spectroscopy (CSRS), or coherent anti-Stokes Raman spectroscopy (CARS). In what follows we refer to this class of Raman spectroscopies as FWMRS (four-wave mixing Raman spectroscopy). The second class is commonly referred to as stimulated Raman spectroscopy (SRS) [1.3]. When the difference frequency of the two laser beams is in resonance with a Raman transition, the higher-frequency beam experiences a loss in intensity, while the lower-frequency beam shows

a corresponding gain in intensity. Observing the gain leads to stimulated Raman gain spectroscopy (SRGS), whereas the observation of the loss is referred to as inverse Raman spectroscopy (IRS) [1.3].

While line shape measurements with either class of CRS are widely used in diagnostic applications to deduce both pressure and temperature, no direct comparison of SRS and FWMRS line shapes and peak positions has come to our attention.

With the use of modern high power lasers, the optical Stark effect is likely to influence or even dominate CRS lineshapes. Its influence on CRS's in their most common form, when focused Gaussian beams are used, has, to our knowledge, not been investigated. Such an investigation may also serve as a quite sensitive test of existing theories for the FWMRS signal generation in focused Gaussian beams.

Simultaneous measurement of both the FWMRS and SRS processes, occurring in the same sample volume, has led to the first direct comparison of their spectra. This technique eliminates systematic errors that are due to different experimental conditions and enables us to detect even small differences between FWMRS and SRS. In the case of mildly focused laser beams, SRS and FWMRS spectra differ slightly due to the influence of neighboring lines [1.2] and inhomogeneous (Doppler) [1.4, 1.5] broadening. Focusing the laser beams more tightly results in a peak pump laser beam intensity of several GW/mm^2. Such a high intensity leads to a shift of molecular energy levels via the optical Stark effect. This effect together with the large intensity variation in focused laser beams can totally dominate the line shapes in CRS, resulting in very different spectra for SRS and FWMRS. While

the optical Stark effect has been previously investigated with the help of FWMRS [1.6, 1.7], little has been known about its influence on the line shapes of CRS's. None-the-less it should be mentioned that L. Li et al. [1.8] have investigated ac-Stark broadened line shapes in two-photon resonant multiphoton ionization, which closely resemble those in SRS. In our study, we simultaneously measure SRS and FWMRS spectra, alternating between tight (Stark effect) and mild focusing (no Stark effect) geometries. With the help of a sophisticated frequency reference scheme we are able to make direct comparisons between Stark broadened and non-Stark broadened SRS and FWMRS spectra. Furthermore we develop a theory to account for the Stark broadening in focused Gaussian beams for both SRS and FWMRS spectra. This theory is also modified to include higher order effects influencing FWMRS. All of our measurements have used the vibrational Q-branch transition v=0 → v=1 in molecular nitrogen. Nitrogen is an important example of a homonuclear diatomic molecule, whose vibrational rotational transitions can not be investigated with the usual methods of infra-red spectroscopy. Furthermore CRS in nitrogen has found many applications in combustion and flow diagnostics [1.9, 1.10, 1.11 and references therein].

Chapter 2 starts with a review of spontaneous and coherent Raman spectroscopy, calculating transition frequencies, cross section, gain coefficients and Stark coefficients for homonuclear diatomic molecules. We proceed to give a theoretical account of the effect of Doppler and pressure broadening on isolated lines, along with a discussion of interference effects between neighboring lines, for both

classes of Raman spectroscopy. Further we develop a theory for the signal generation in focused Gaussian beams for both SRS and FWMRS. This theory is then used to calculate Stark broadened spectra generated by focused Gaussian beams.

The experimental setup is described in the first part of chapter 3. The second part presents experimental results, including simultaneously measured CSRS and IRS spectra of both Stark broadened and non-Stark broadened lines in the $v=0 \rightarrow v=1$ Q-branch vibrational spectrum of molecular nitrogen. These spectra are compared with theoretical results developed in chapter 2.

Chapter 4 discusses two relevant new nonlinear optical effects. First we consider a new phase modulation effect introduced by rapid Stark tuning of the molecular transition frequency. We present theoretical spectra for a variety of experimental conditions and explain why this effect, which should be observable under certain experimental conditions, has not been observed in our experiments. We then discuss a fifth order nonlinear process which may affect the Stark broadened line shapes of FWMRS under our experimental conditions. These new effects are ideal candidates for future studies.

The thesis ends with a brief conclusion in chapter 5.

References Chapter 1

1.1 R.F. Begley, A.B. Harvey, and R.L. Byer, "Coherent Anti-Stokes Raman Spectroscopy," Appl. Phys. Lett. **25**, 387 (1974).

1.2 W.M. Tolles, J.W. Nibler, J.R. McDonald, and A.B. Harvey, "A Review of the Theory and Application of Coherent Anti-Stokes Raman Spectroscopy (CARS),"Appl. Spectrosc. **31**, 253 (1977).

1.3 P. Esherick and A. Owyoung, "High Resolution Stimulated Raman Spectroscopy," in Advances in Infrared and Raman Spectroscopy, R.J.H. Clark and R.E. Hestor eds. (Heyden & Son Ltd. London 1982), Vol.9.

1.4 M.A. Henesian, L. Kulevskii, R.L. Byer, and R.L. Herbst, "Cw High-Resolution CAR Spectroscopy of H_2, D_2, and CH_4,"Opt. Commun. **18**, 225 (1976).

1.5 M.A. Henesian and R.L. Byer, "High-Resolution CARS Line-Shape Function," J. Opt. Soc. Am. **68**, 648 (1978).

1.6 L.A. Rahn, R.L. Farrow, M.L. Koszykowski and P.L. Mattern, "Observation of an Optical Stark Effect on Vibrational and Rotational Transitions," Phys. Rev. Lett. **45**, 620 (1980).

1.7 R.L. Farrow and L.A. Rahn, "Optical Stark Splitting of Rotational Raman Transitions," Phys. Rev. Lett. **48**, 395 (1982).

1.8 L. Li, B.X. Yang and P.M. Johnson, "Alternating-Current Stark-Effect Line Shapes in Multiphoton Ionization Spectra," J. Opt. Soc. Am. B **2**, 748 (1985).

1.9 A.C. Eckbreth, G.M. Dobbs, J.H. Stufflebeam and P.A. Tellex, "CARS Temperature and Species Measurements in Augmented Jet Engine Exhausts," Appl. Opt. **23**, 1328 (1984).

1.10 E.J. Beiting, "Multiplex CARS Temperature Measurements in a Coal-Fired MHD Environment," Appl. Opt. **25**, 1684 (1986).

1.11 C.Y. She, H. Moosmüller and G.C. Herring, "Coherent Light Scattering Spectroscopy for Supersonic Flow Measurements," Appl. Phys. **B45**, to be published (1988).

Chapter 2

Theory of Raman Spectroscopy

2.1 Vibrational-Rotational Spectroscopy of Homonuclear Diatomic Molecules

This chapter reviews the vibrational-rotational spectroscopy of homonuclear diatomic molecules in the electronic ground state $^1\Sigma_g^+$ [2.1]. We use the frame work of polarizability theory [2.1, 2.2], which assumes that the polarizability, while being mediated by the electronic wave function, is only a function of the nuclear coordinates and their derivatives. Most of the time we assume further that electronic, vibrational and rotational wave functions can be factorized. The macroscopic state of the molecules is specified as a dilute gas (refractive index n=1), leading to the assumption of randomly oriented, non interacting molecules. Molecular nitrogen (N_2^{14}, electronic ground state $^1\Sigma_g^+$) is of special interest because it has been used for our experimental investigations. Most of the equations in sections 2.1.1 - 2.1.5 can be found in Herzberg's book "Spectra of Diatomic Molecules", [2.1] which is not explicitly referred to in these sections. An excellent treatment of spontaneous Rayleigh and Raman scattering is given by Placzek's review article "Rayleigh Streuung und Raman Effekt" [2.2].

2.1.1 Rotational Energy Levels

Homonuclear diatomic molecules can be modeled as two points of equal mass 2μ, connected by a rigid massless bar of length r_e. For this model, the reduced mass is μ and we can write the moment of inertia of the molecule as

$$I = \mu\, r_e^2. \tag{2.1}$$

While the classical angular momentum M_c is defined as

$$M_c = I\, \omega, \tag{2.2}$$

we can obtain the quantum mechanical expression, by solving the Schrödinger equation for a rigid rotator, as

$$M = \frac{h}{2\,\pi}\,[l(l+1)]^{0.5}, \tag{2.3}$$

with h being Planck's constant and l the rotational quantum number, which can have values of

$$l = 0,\ 1,\ 2,\ 3,\ \ldots. \tag{2.4}$$

The rotational energy E_{rot} is given by

$$E_{rot} = \frac{M^2}{2I} = \frac{h^2 l(l+1)}{8\pi^2\, I} = \frac{h^2 l(l+1)}{8\pi^2 r^2 \mu}. \tag{2.5}$$

After conversion to the usual spectroscopic units (cm^{-1}) the rotational energy term F(l) can be written as

$$F(l) = B_e\, l(l+1), \tag{2.6}$$

with the rotational constant B_e defined as

$$B_e = \frac{h}{8\pi^2 cI}, \tag{2.7}$$

where c stands for the speed of light. We can see from Eq. (2.6) that the spacing of the rotational energy levels is not equidistant, but increases with increasing l.

It is clear that the model of the rigid rotator is inadequate, because a molecule, which can vibrate can not be totally rigid. Therefore we have to replace the rigid bar connecting the atoms by a massless spring. For higher rotational frequencies we expect the centrifugal force to stretch the molecule, increasing the interatomic distance r_e and thus the moment of inertia I. This leads to a rotational constant B_e, which decreases with increasing rotational excitation, i.e. with increasing l, lowering the respective energy levels. To a very good approximation B_e can be replaced by $B_e[1-ul(l+1)]$, where u is a constant. This equation is usually rewritten as

$$F(l) = B_e l(l+1) - D_e l^2 (l+1)^2, \qquad (2.8)$$

with $D_e = uB_e$ always being positive. Under the assumption of Hookes law for the connecting spring, we can set the restoring force equal to the centrifugal force and thus calculate the rotational constant D_e as [2.1, p.103]

$$D_e = \frac{4B_e^3}{\omega^2}, \qquad (2.9)$$

where ω is the vibrational frequency in units of cm^{-1}.

2.1.2 Vibrational Energy Levels

The simplest possible model for the vibrational motion is the harmonic oscillator. The system of two points of equal mass 2μ connected by a massless spring with the elastic constant k_0, can easily be reduced to a simple one-dimensional harmonic oscillator with identical elastic constant and the reduced mass μ. According to classical theory this oscillator has a vibrational frequency ν_{osc} of

$$\nu_{osc} = (1/2\pi)(k_0/\mu)^{0.5}, \tag{2.10}$$

and a potential energy V of

$$V = 0.5k_0(r-r_e)^2, \tag{2.11}$$

where $(r-r_e)$ is the distance from the equilibrium position r_e. Quantum mechanics gives the energy of this oscillator as

$$E_{vib} = h\nu_{osc}(v+1/2), \tag{2.12}$$

where the vibrational quantum number can take only integral values v = 0, 1, 2, 3,.... By converting to spectroscopic units (cm^{-1}), we obtain the vibrational energy term G(v) as

$$G(v) = \omega_e(v+1/2), \tag{2.13}$$

where ω_e is the vibrational frequency ν_{osc} measured in cm^{-1} ($\omega_e = \nu_{osc}/c$). Equation (2.13) shows that the vibrational energy levels are, in this approximation, equidistantly spaced.

While the harmonic oscillator is a satisfactory approximation for small vibrational quantum numbers, anharmonicities become increasingly more important for higher quantum numbers. We can write the potential energy of the anharmonic oscillator, U, by adding higher order terms, as

$$U = \tfrac{1}{2} k_0(r-r_e)^2 - k_1(r-r_e)^3 + k_2(r-r_e)^4 + ... \tag{2.14}$$

For small anharmonicities ($\frac{1}{2}k_0 >> k_1(r-r_e) >> k_2(r-r_e)^2$) the vibrational energy term is given as

$$G(v) = \omega_e(v+1/2) - \omega_e x_e(v+1/2)^2 + \omega_e y_e(v+1/2)^3 + \omega_e z_e(v+1/2)^4 + ..., \tag{2.15}$$

with $\omega_e z_e << \omega_e y_e << \omega_e x_e << \omega_e$. For a positive k_1, $\omega_e x_e$ is always positive; this is the case for the usual asymmetry in molecular potentials (Morse potential).

2.1.3 Interaction between Vibration and Rotation

So far we have considered vibration and rotation separately, neglecting their interactions. Now we consider simultaneous vibration and rotation which leads to the vibrating rotator or rotating oscillator as a more refined model.

Due to the anharmonicity of the molecular potential, the mean value of the square of the atomic separation $\langle r^2 \rangle$ is no longer equal to the square of equilibrium value r_e^2, but in most cases (k_1 positive) larger ($\langle r^2 \rangle > r_e^2$). Because the period of rotation is usually much larger than the period of vibration, we can use $\langle r^2 \rangle$ for the calculation of a new rotational constant B_v, which is somewhat smaller than the equilibrium constant B_e. B_v can be written as

$$B_v = B_e - \alpha_e(v+1/2) + \gamma_e(v+1/2)^2 + \ldots, \qquad (2.16)$$

with $\gamma_e \ll \alpha_e \ll B_e$. Following the same argumentation we have to replace the rotational constant D_e by D_v, with

$$D_v = D_e + \beta_e(v+1/2) + \ldots, \qquad (2.17)$$

where β_e is small compared to D_e. With these corrections we can write the rotational energy term F_v of a given vibrational level v as

$$F_v(1) = B_v 1(1+1) - D_v 1^2(1+1)^2 + \ldots. \qquad (2.18)$$

The total energy term for the vibrating rotator can now be given as

$$T(v,1) = G(v) + F_v(1) = \omega_e(v+1/2) - \omega_e x_e(v+1/2)^2 + \omega_e y_e(v+1/2)^3 + \omega_e z_e(v+1/2)^4 + \ldots + B_v 1(1+1) - D_v 1^2(1+1)^2 + \ldots. \qquad (2.19)$$

The corresponding energy level diagram is shown in Fig. 2.1.

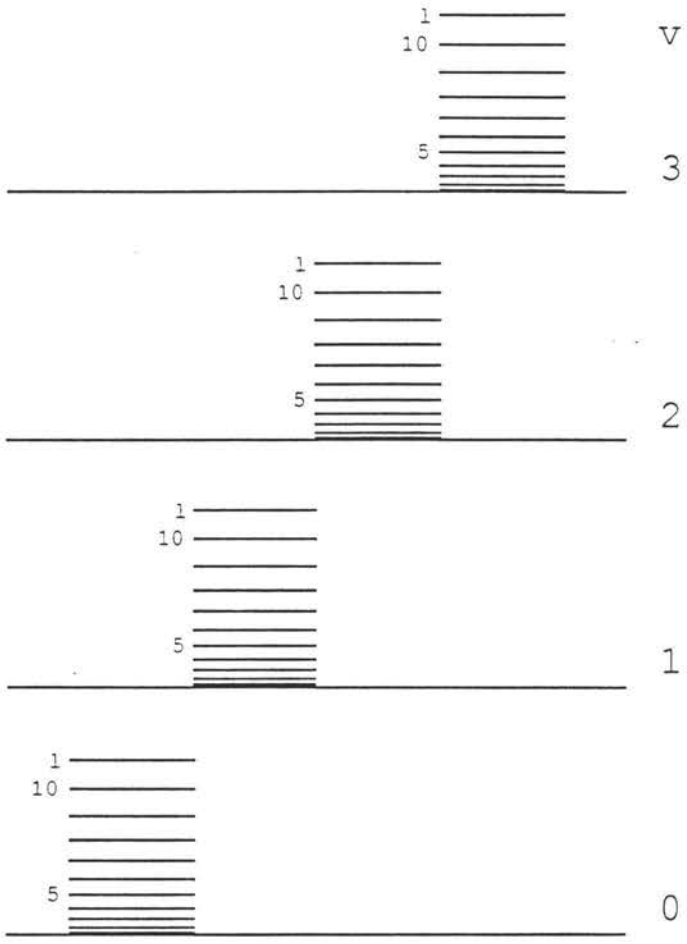

Fig. 2.1. Energy levels of the vibrating rotator

The spectroscopic constants needed to evaluate the total energy term can either be obtained from theoretical calculations, or, with higher precision, from vibrational-rotational spectra.Table 2.1 lists fairly recent values for N_2, as obtained by L. Rahn [2.3].

Table 2.1. Spectroscopic constants for N_2[2.3]

Vibrational constants:
$\omega_e = 2358.5141\text{cm}^{-1}$
$\omega_e x_e = 14.2935\text{cm}^{-1}$
$\omega_e y_e = 0.00592949\text{cm}^{-1}$
$\omega_e z_e = -0.00024\text{cm}^{-1}$

Rotational constants:
$B_e = 1.99826\text{cm}^{-1}$
$\alpha_e = 0.017322\text{cm}^{-1}$
$\gamma_e = -0.0000315361\text{cm}^{-1}$
$D_e = 0.00000576\text{cm}^{-1}$
$\beta_e = 0.0\text{cm}^{-1}$

2.1.4 Population of Vibrational-Rotational States

The relative population of the different molecular states is determined by the Boltzmann factor together with the statistical weight g_i as

$$\frac{n_i}{n_j} = \frac{g_i}{g_j} \exp\left(\frac{E_j - E_i}{kT}\right), \tag{2.20a}$$

where n, g, E are population, statistical weight and energy of a specific state i or j, and k, T are Boltzmann's constant and the absolute temperature. With $N = \sum_{j=1,\infty} n_j$ being the total population (number of molecules), we can write

$$n_i = N \frac{g_i \exp(-E_i/kT)}{Q}, \tag{2.20b}$$

where $Q = \sum_{j=1,\infty} g_j \exp(-E_j/kT)$ is the partition function.

The calculation of the vibrational state populations is especially straightforward because g_v is unity for all vibrational states. In the case of molecular nitrogen at room temperature Eq. (2.20a) results in

$$n_{v>1} \ll n_{v=1} = 1.4\ 10^{-5}\ n_{v=0}, \tag{2.21}$$

therefore the exited state population is negligible.

Rotational state populations can only be calculated after the degeneracies (statistical weights) of the individual states have been evaluated. The total degeneracy g_{rot} of a rotational state can be written as a function of rotational angular momentum 1 and nuclear degeneracy g_{nuc} as

$$g_{rot} = (21+1)g_{nuc}, \tag{2.22}$$

where 21+1 is the usual degeneracy of a state with angular momentum 1 and g_{nuc} is the nuclear degeneracy. In the case of N_2, each nitrogen nucleus (N^{14}) has the nuclear spin I=1. Therefore the nuclei are Bose particles and the molecule can have a total nuclear spin T of 0, 1 or 2. The corresponding statistical weights g_T are obtained from 2T+1 as 1, 3, 5. Now we have to figure out which values of the total nuclear spin T can coexist with certain values of the rotational angular momentum 1. Let us consider the symmetry operation of coordinate inversion, relative to the center of the molecule. This operation exchanges the nuclei in a diatomic homonuclear molecule, producing a new state, ψ_n, indistinguishable from the original state ψ_o. Therefore we have $|\psi_n|^2 = |\psi_o|^2$, consequently the original state is either symmetric with respect to this operation, resulting in $\psi_n = \psi_o$, or antisymmetric, resulting in $\psi_n = -\psi_o$. The total amplitude of two indistinguishable states is, for Bose particles, the sum of the

individual amplitudes: $\psi_{tot} = \psi_n + \psi_o$ [2.4], therefore only states which are symmetric with respect to exchange of the nuclei contribute. The symmetry of the wave function ψ_o is determined by its two factors, which can be either symmetric or antisymmetric: $\psi_{tot} \simeq \psi_{nuc}\psi_{rot}$. The symmetry of both the nuclear wave function ψ_{nuc} and the rotational wave function ψ_{rot} is identical to the symmetry of the spherical harmonics Y_l^m, with l corresponding to T or l, respectively. The symmetry of Y_l^m is $(-1)^l$ [2.5], symmetric for even l's, antisymmetric for odd l's. To achieve a symmetric ψ_{tot}, as required, we have to combine even l's with even T's and odd l's with odd T's. This determines the nuclear degeneracy for rotational states of N_2 as

$$g_{nuc} = g_0 + g_2 = 1 + 5 = 6, \text{ for even l's,} \tag{2.23a}$$

$$g_{nuc} = g_1 = 3, \text{ for odd l's.} \tag{2.23b}$$

Nuclear degeneracies for homonuclear diatomic molecules with different nuclear spin can be derived in similar manner. The resulting degeneracies can be expressed as

$$g_{nuc} = 2I^2 + 3I + 1 \quad \text{for} \begin{cases} \text{even l and Bose statistics, or} \\ \text{odd l and Fermi statistics.} \end{cases} \tag{2.24a}$$

$$g_{nuc} = 2I^2 + I \quad \text{for} \begin{cases} \text{even l and Fermi statistics, or} \\ \text{odd l and Bose statistics.} \end{cases} \tag{2.24b}$$

These equations are a special case of the general equation for linear molecules, as given by reference [2.6]. The population of a rotational state with the quantum number l relative to the total number of molecules N can now be written as

$$\frac{n_l}{N} = \frac{g_{nuc}(2l+1)}{Q} \exp\left[\frac{-E_l}{k\,T}\right]. \tag{2.25}$$

This population distribution is shown in Fig. (2.2) for N_2 at room temperature (T = 292K). The numerical value for the partition function Q is under these conditions Q = 458.5.

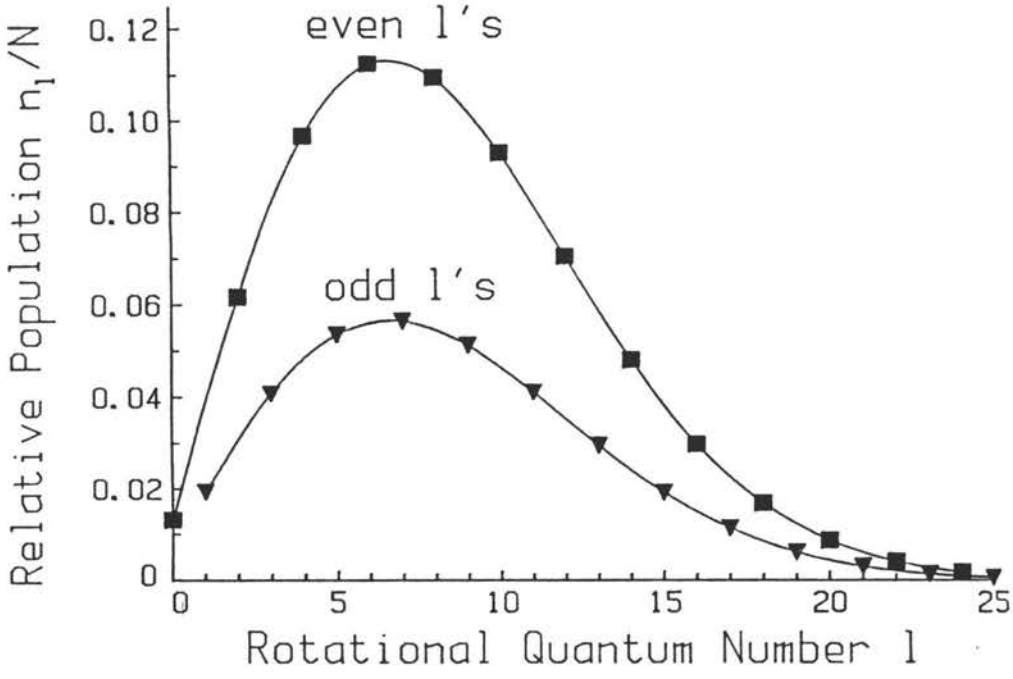

Fig. 2.2. Rotational population distribution for N_2 at room temperature (T=292K)

Distributions such as Eq. (2.25), which are based on the Boltzmann factor are only valid for ensembles of molecules in thermodynamic equilibrium. While for most degrees of freedom, thermodynamic equilibrium is achieved rapidly, transitions between states with symmetric and antisymmetric nuclear wave functions are strongly forbidden, with transition times in the order of weeks or months. This

has led to the designation of two modifications of N_2, ortho nitrogen has a symmetric nuclear wave function and an even rotational quantum numbers l, while para nitrogen corresponds to antisymmetric ψ_{nuc} and odd l's. At higher temperatures a large number of rotational levels is populated and the nuclear degeneracies g_{nuc} in Eq. (2.25) result in a two-to-one ratio for ortho and para nitrogen. If this mixture is cooled below roughly 5K, its two-to-one ratio no longer agrees with the thermodynamic equilibrium, given by Eq. (2.25). Because of the long relaxation time between ortho and para nitrogens, they are expected to maintain their ratio for a long time. Therefore Eq. (2.25) has to be applied with great care.

2.1.5 Vibrational-Rotational Spectra

The strongest spectral lines are generally caused by electric dipole transitions. The transition amplitude is proportional to the matrix element of the electric dipole moment $\langle v,l|\mu|v',l'\rangle$, which corresponds to the change of the electrical dipole moment μ with respect to the generalized coordinate q of the transition, i. e. $\frac{\partial \mu}{\partial q}$. For homonuclear diatomic molecules the permanent electric dipole moment μ is zero for all values of the rotational coordinate (angle) and for all values of the vibrational coordinate (interatomic separation), yielding derivatives which are also zero. This is due to the symmetry of the charge distribution relative to the center of the molecule. Therefore electric dipole transitions between vibrational and rotational levels are forbidden.

Lacking a permanent electric dipole moment, we have to consider the possibility of a dipole moment induced by the interaction of the electric field E with the molecule. Quantum mechanically this can be done by second order perturbation theory, which calculates molecular wave functions modified by the electrical field. Classically we can write the induced dipole moment p of a molecule as

$$p = \epsilon_0 \alpha E, \tag{2.26}$$

where ϵ_0 is the vacuum permittivity and the electrical field E can be defined as

$$E = \frac{E_0}{2} \left(e^{i(\omega t - \vec{k}\cdot\vec{r} + \phi)} + e^{-i(\omega t - \vec{k}\cdot\vec{r} + \phi)}\right). \tag{2.27a}$$

Combining Eq. (2.26) and Eq. (2.27a) suggests a similar definition for the induced dipole moment p

$$p = \frac{p_0}{2} \left[e^{i(\omega t - \vec{k}\cdot\vec{r} + \phi)} + e^{-i(\omega t - \vec{k}\cdot\vec{r} + \phi)}\right], \text{ with} \tag{2.27b}$$

$$p_0 = \epsilon_0 \alpha E_0. \tag{2.27c}$$

The polarizability α can be expanded as a Taylor series in the normal coordinates q

$$\alpha(q) = (\alpha)_0 + \left(\frac{\partial \alpha}{\partial q}\right)_0 q + \ldots. \tag{2.28}$$

Each term of this series corresponds to a different kind of light scattering. The first term, the permanent polarizability is independent of the coordinate q, i. e. independent of the vibrational-rotational state ψ_n. Therefore the molecular state does not change during the scattering process ($\langle \psi_m | \alpha_0 | \psi_n \rangle = \delta_{n,m}$) resulting in elastic (Rayleigh) scattering. The second term corresponds to the change of polarizability with the change of q, resulting in inelastic (Raman) scattering. After the scattering process the molecule can be either in

a state with higher or lower energy, corresponding to Stokes or anti-Stokes scattering. Energy conservation results in an equivalent energy loss or gain for the scattered photon (Fig. 2.3), which allows the determination of molecular energy levels by measuring the frequency shift of the scattered photon.

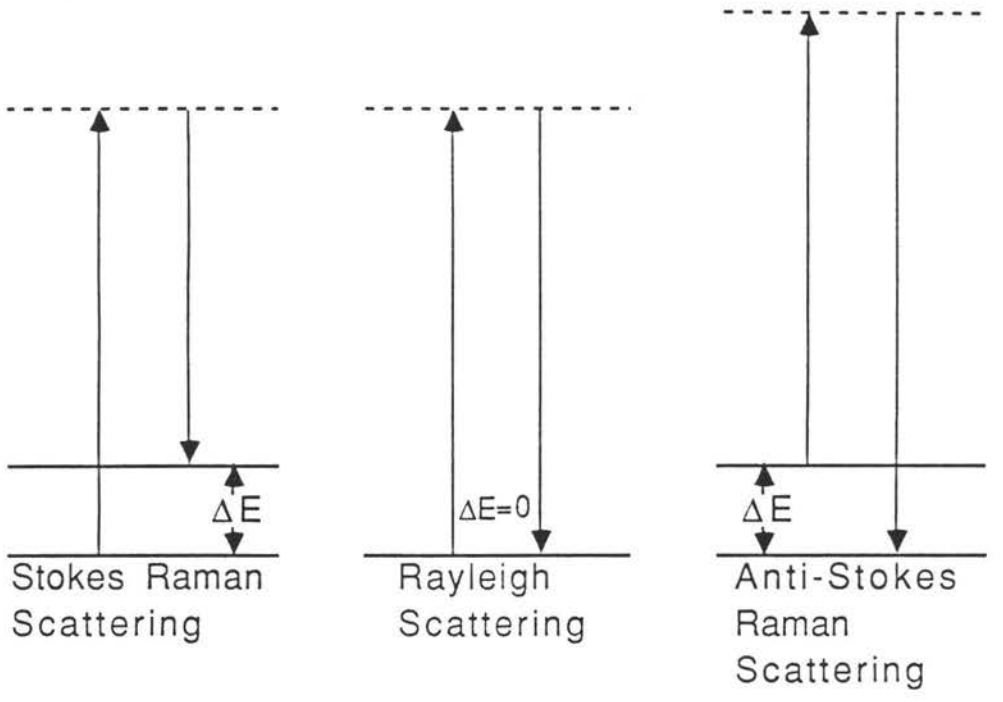

Fig. 2.3. Energy transfer and relative position of energy levels for Rayleigh and Raman (Stokes and anti-Stokes) scattering

This technique is generally called Raman spectroscopy. From the fact that Raman scattering is a two photon process, we can directly deduce the selection rule for the rotational quantum number. Each photon carries an angular momentum of one, therefore the exchange of two

photons can change the angular momentum of the molecule by -2, 0, or 2. For diatomic molecules this corresponds to the selection rule

$$\Delta l = \begin{cases} +2 & \text{S-branch} \\ 0 & \text{Q-branch,} \\ -2 & \text{O-branch} \end{cases} \qquad (2.29a)$$

where Δl is defined as $\Delta l = l_{\text{final state}} - l_{\text{initial state}}$. The equivalent selection rule for the vibrational quantum number v,

$$\Delta v = \begin{cases} +1 & \text{Stokes scattering} \\ -1 & \text{anti-Stokes scattering} \end{cases} \qquad (2.29b)$$

has been obtained by explicitly calculating the matrix elements of q with respect to the eigenfunctions of the linear harmonic oscillator [2.6]. For O- and S-branches the different l lines have in first approximation (rigid rotator, Eq. (2.6)) an equidistant energy spacing of $4B_e$. In the same approximation the Q-branch collapses to a single line. Taking the interaction between vibration and rotation into account, we can use Eq. (2.16), with $\gamma_e = 0$, to calculate the approximate distance between Q-branch lines. For the transition v=0 → v=1 this results in a spacing of $2\alpha_e(l+1)$ between the line l and l+1. For N_2, α_e is more than two orders of magnitude smaller than B_e, the Q-branch lines are therefore much more closely spaced than those of O- and S-branch.

2.1.6 Differential Cross Sections of Vibrational-Rotational Raman Transitions

In a light scattering process, such as Raman scattering, the oscillating electrical field $\vec{E}$ of a linearly polarized light wave, induces an oscillating molecular dipole of magnitude $\vec{p}_0 = \epsilon_0 \alpha \vec{E}_0$ (Eq. (2.27b)). According to electromagnetic theory, the power P radiated by

an oscillating dipole moment into a solid angle Ω, can be written as [2.7]

$$\frac{dP}{d\Omega} = \frac{c\pi^2 p_0^2}{2\epsilon_0 \lambda^4} \sin^2(\theta), \tag{2.30}$$

where θ is angle between dipole axis and direction of observation, while λ stands for the wavelength of the scattered light. If we use polarized detection, with $\hat{\epsilon}$ being the unit vector of the electrical field transmitted through our polarization analyser, we can rewrite Eq. (2.30) as

$$\frac{dP}{d\Omega} = \frac{c\pi^2}{2\epsilon_0 \lambda^4} (\vec{p}_0 \cdot \hat{\epsilon})^2. \tag{2.31}$$

In the following we consider only the case of linearly polarized incoming light and of linearly polarized detection. The equations for all other experimental situations can be deduced by adding up different linear polarizations. Equation (2.31) together with Eq. (2.27c) yields

$$\frac{dP}{d\Omega} = I_0 \frac{\pi^2}{\lambda^4} (\alpha \hat{\epsilon}_i \cdot \hat{\epsilon})^2, \text{ with} \tag{2.32a}$$

$$I_0 = \frac{1}{2} c \epsilon_0 E_0^2, \tag{2.32b}$$

and $\hat{\epsilon}_i$, being the intensity and the unit vector of polarization of the incoming wave, respectively. We can eliminate the intensity parameter by defining the differential scattering cross section $\frac{d\sigma}{d\Omega}$ as

$$\frac{d\sigma}{d\Omega} = \frac{1}{I_0} \frac{dP}{d\Omega} = \frac{\pi^2}{\lambda^4} (\alpha \hat{\epsilon}_i \cdot \hat{\epsilon})^2. \tag{2.33}$$

In the case of molecules with isotropic polarizability (for example CCl_4), α is a scalar and Eq. (2.33) completely describes the scattering process. For all other molecules we have to consider their

spatial orientation. We introduce a laboratory coordinate system with unit vectors $\hat{x}$, $\hat{y}$ and $\hat{z}$, and a coordinate system for an individual molecule with unit vectors $\hat{X}$, $\hat{Y}$ and $\hat{Z}$ (Fig. 2.4).

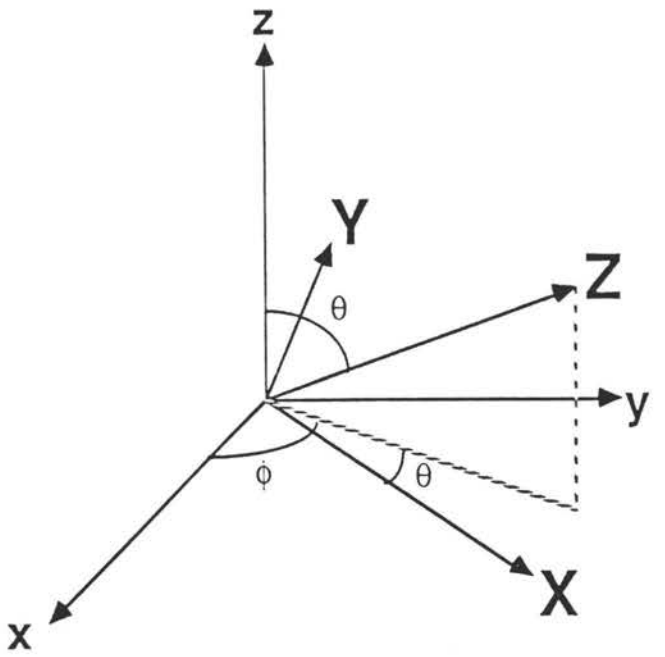

Fig. 2.4. Laboratory (x,y,z) and molecular (X,Y,Z) coordinate systems

The polarizability α is a second rank tensor, which can be written as a sum of its symmetric and its anti-symmetric part. The anti-symmetric part, which induces optical rotation [2.8], is for most molecules (all diatomic molecules) equal zero. By choosing an appropriate orientation of the molecular coordinate system, the symmetric part can be made diagonal. In the case of diatomic molecules, we choose $\hat{Z}$ parallel to the internuclear axis and designate α_Z as $\alpha_{\parallel}$. Due to the symmetry of diatomic molecules, the polarizability α is degenerate in the $\hat{X}$-$\hat{Y}$

plane and we designate $\alpha_X=\alpha_Y$ as $\alpha_\perp$. Therefore we write the polarizability tensor as

$$\alpha = \begin{pmatrix} \alpha_\perp & 0 & 0 \\ 0 & \alpha_\perp & 0 \\ 0 & 0 & \alpha_\parallel \end{pmatrix} \tag{2.34}$$

Because of the degeneracy in the $\hat{X}$-$\hat{Y}$ plane we are free to put the molecular $\hat{Y}$-axis into the $\hat{x}$-$\hat{y}$ plane and we don't have to use the full set of Euler angles (Fig. 2.4). Now we can write a vector either in the laboratory system as $\vec{r}$ or in the molecular system as $\vec{R}$. These two representations are connected by the following transformations

$$\vec{R} = \eta\, \vec{r} \quad \text{and} \tag{2.35a}$$

$$\vec{r} = \eta^{-1}\, \vec{R}. \tag{2.35b}$$

By using Fig. 2.4 and some basic trigonometry we can write the matrix η in terms of the direction cosines as

$$\eta = \begin{pmatrix} \cos(\theta)\cos(\phi) & \cos(\theta)\sin(\phi) & -\sin(\theta) \\ -\sin(\phi) & \cos(\phi) & 0 \\ \sin(\theta)\cos(\phi) & \sin(\theta)\sin(\phi) & \cos(\theta) \end{pmatrix} \tag{2.36}$$

Both of our coordinate systems are orthogonal, therefore η is an orthogonal matrix and its inverse η^{-1} is equal to its transpose $\tilde{\eta}$ [2.9]

$$\eta^{-1} = \tilde{\eta}. \tag{2.37}$$

With an incoming wave linearly polarized in the $\hat{z}$ direction, we can write the magnitude of the electrical field $\vec{E}_R$ in molecular coordinates as

$$\vec{E}_R = \eta\,\vec{E}_r = \eta \begin{pmatrix} 0 \\ 0 \\ E_0 \end{pmatrix} = E_0 \begin{pmatrix} -\sin(\theta) \\ 0 \\ \cos(\theta) \end{pmatrix} \tag{2.38}$$

and the magnitude of the induced dipole moment, written in molecular coordinates, is therefore (Eq. (2.27c))

$$\vec{P}_R = \epsilon_0 E_0 \begin{pmatrix} -\alpha_\perp \sin(\theta) \\ 0 \\ \alpha_\parallel \cos(\theta) \end{pmatrix} . \tag{2.39}$$

To relate to laboratory measurements we write the induced dipole moment in laboratory coordinates as

$$\vec{P}_r = \eta^{-1}\,\vec{P}_R = \epsilon_0 E_0 \begin{pmatrix} (\alpha_\parallel - \alpha_\perp)\cos(\theta)\sin(\theta)\cos(\phi) \\ (\alpha_\parallel - \alpha_\perp)\cos(\theta)\sin(\theta)\sin(\phi) \\ \alpha_\parallel \cos^2(\theta) + \alpha_\perp \sin^2(\theta) \end{pmatrix} , \tag{2.40}$$

where $\vec{P}_r$ is the dipole moment of a single molecule, with an orientation specified by the angle θ and ϕ. The power we detect from this radiating molecule is, according to Eq. (2.31), proportional to $(\vec{P}_r \cdot \hat{\epsilon})^2$. Now we have to consider that Raman scattering is normally performed on an ensemble of molecules, therefore we must add up the contribution of the individual molecules according to their orientation. At this point we will limit the discussion to dilute gases, where the individual molecules are randomly oriented. Therefore we calculate the average power, that we detect from one radiating molecule.

The classical procedure takes the orientational average $\langle(\vec{P}_r \cdot \hat{\epsilon})^2\rangle$ of $(\vec{P}_r \cdot \hat{\epsilon})^2$ by means of the definition

$$\langle f(\theta,\phi)\rangle = \frac{1}{4\pi}\int d\Omega \sin(\theta) f(\theta,\phi) = \frac{1}{4\pi}\int d\theta \sin(\theta)\int_0^{2\pi} d\phi f(\theta,\phi). \qquad (2.41)$$

$\langle(\vec{p}_r\cdot\hat{\epsilon})^2\rangle$ can be written as

$$\langle(\vec{p}_r\cdot\hat{\epsilon})^2\rangle = \langle(p_x\epsilon_x+p_y\epsilon_y+p_z\epsilon_z)^2\rangle = \langle(p_x^2\epsilon_x^2+p_y^2\epsilon_y^2+p_z^2\epsilon_z^2)\rangle, \qquad (2.42)$$

with all cross terms averaging to zero. Using Eq. (2.41) we calculate the following identities

$$\langle\cos^2(\theta)\rangle = 1/3, \qquad (2.43a)$$

$$\langle\cos^4(\theta)\rangle = 1/5 \text{ and} \qquad (2.43b)$$

$$\langle\cos^2(\theta)\sin^2(\theta)\cos^2(\phi)\rangle = 1/15. \qquad (2.43c)$$

These identities together with Eq. (2.27c) and Eq. (2.33) yield the final expression for the differential scattering cross section as

$$\frac{d\sigma}{d\Omega} = \frac{\pi^2}{\lambda^4}\left[\frac{1}{15}\gamma^2(\epsilon_x^2+\epsilon_y^2) + (a^2+\frac{4}{45}\gamma^2)\epsilon_z^2\right], \qquad (2.44)$$

where the invariants of the polarizability tensor, a and γ are defined as

$$a = (\alpha_{\parallel} + \alpha_{\perp})/3, \qquad (2.45a)$$

$$\gamma = \alpha_{\parallel} - \alpha_{\perp}. \qquad (2.45b)$$

Equation (2.44) is the classical expression for the light scattering cross section. In the classical limit ($l \to \infty$), O-, Q- and S-branches can no longer be distinguished and Eq. (2.44) stands therefore for the sum of the cross section of those branches. With this equation we can calculate scattered intensities for any direction and polarization; depolarization ratios can also be obtained directly.

Quantum mechanically we replace the classical orientational variables by the corresponding operators. Therefore we calculate the matrix elements of the dipole moment $\vec{p}_r$ (Eq. (2.40)) with respect to

the vibrational rotational wave function $|vlm\rangle$. Under the Born-Oppenheimer approximation, this wave function can be factorized as $|vlm\rangle = |v\rangle|lm\rangle$ and we can express the matrix elements of $\vec{p}_r$ as

$$\langle v'l'm'|\vec{p}_r|vlm\rangle = \langle l'm'| \langle v'|\vec{p}_r|v\rangle |lm\rangle \tag{2.46}$$

The eigenfunctions of the harmonic oscillator (Hermite's polynomials), commute with the spherical harmonics Y_1^m, therefore we evaluate only ([2.10] and Eq. (2.28))

$$a^v_{v'} = \langle v'|a|v\rangle = \langle v'|(a)_0|v\rangle + \langle v'|q|v\rangle\left(\frac{\partial a}{\partial q}\right)_0 \tag{2.47a}$$

$$= a^v_v\delta_{v,v'} + \left(\frac{h}{4\pi\mu\Delta}\right)^{0.5}\left((v+1)^{0.5}\delta_{v',v+1} + (v)^{0.5}\delta_{v',v-1}\right)\left(\frac{\partial a}{\partial q}\right)_0 \text{ and}$$

$$\gamma^v_{v'} = \langle v'|\gamma|v\rangle = \langle v'|(\gamma)_0|v\rangle + \langle v'|q|v\rangle\left(\frac{\partial \gamma}{\partial q}\right)_0 \tag{2.47b}$$

$$= \gamma^v_v\delta_{v,v'} + \left(\frac{h}{4\pi\mu\Delta}\right)^{0.5}\left((v+1)^{0.5}\delta_{v',v+1} + (v)^{0.5}\delta_{v',v-1}\right)\left(\frac{\partial \gamma}{\partial q}\right)_0,$$

where Δ is the vibrational frequency. The permanent components of a and γ, a^v_v and γ^v_v, result in Rayleigh and rotational Raman scattering, while the other terms result in Stokes and anti-Stokes vibrational-rotational Raman scattering, confirming the selection rule given in Eq. (2.29b). Using ab initio data of Langhoff et al. [2.11] and an RKR potential in the vibrational calculation, W. M. Huo has calculated a^0_0, a^1_1, a^0_1, γ^0_0, γ^1_1 and γ^0_1 for molecular nitrogen [2.12]. Her calculation includes vibrational-rotational interactions, and the resulting polarizabilities, listed in table 2.2, therefore depend on the rotational quantum number 1. The transition polarizabilities $a^0_1(1)$ and $\gamma^0_1(1)$ are listed only for the Q-branch, but a connection to O- and S-branch values can be found in reference [2.11].

Table 2.2. Isotropic and anisotropic, permanent and transition polarizabilities of N_2 [2.12], in units of $Å^3 = 10^{-30} m^3$.

l	$a_0^0(Å^3)$	$a_1^1(Å^3)$	$a_1^0(Å^3)$	$\gamma_0^0(Å^3)$	$\gamma_1^1(Å^3)$	$\gamma_1^0(Å^3)$
0	21.895220	22.080880	0.690539	8.621598	8.864717	0.753928
1	21.895360	22.081020	0.690545	8.621748	8.864854	0.753945
2	21.895630	22.081300	0.690563	8.622046	8.865132	0.753980
3	21.896040	22.081710	0.690589	8.622490	8.865545	0.754036
4	21.896580	22.082250	0.690625	8.623084	8.866098	0.754109
5	21.897270	22.082940	0.690671	8.623827	8.866789	0.754200
6	21.898090	22.083770	0.690727	8.624718	8.867620	0.754310
7	21.899040	22.084730	0.690790	8.625758	8.868587	0.754439
8	21.900130	22.085830	0.690856	8.626946	8.869696	0.754580
9	21.901360	22.087060	0.690936	8.628285	8.870944	0.754744
10	21.902730	22.088440	0.691025	8.629773	8.872333	0.754925
11	21.904220	22.089950	0.691124	8.631409	8.873861	0.755122
12	21.905860	22.091610	0.691230	8.633194	8.875531	0.755338
13	21.907640	22.093400	0.691345	8.635131	8.877344	0.755573
14	21.909550	22.095330	0.691470	8.637215	8.879299	0.755822

Next we evaluate $\vec{p}_r$ with respect to the rotational part of the wave function. Using the explicit expressions for the spherical harmonics Y_1^m [2.5] we can evaluate orientational averages of Eq. (2.40), and write $\vec{p}_r$ as

$$\vec{p}_r = \epsilon_0 E_0 \begin{pmatrix} (2\pi/15)^{0.5} \gamma_{v'}^{v} (Y_2^{-1} - Y_2^{1}) \\ i(2\pi/15)^{0.5} \gamma_{v'}^{v} (Y_0^{-1} + Y_2^{1}) \\ a_{v'}^{v} + \frac{4}{3} (\pi/5)^{0.5} \gamma_{v'}^{v} Y_2^{0} \end{pmatrix}. \qquad (2.48)$$

We calculate the matrix elements of the spherical harmonics in terms of Clebsch-Gordan coefficients, using the following equation [2.13]

$$\langle l_3 m_3 | Y_{l_2}^{m_2} | l_1 m_1 \rangle = \left[\frac{(2l_1+1)(2l_2+1)}{4\pi(2l_3+1)} \right]^{0.5} \langle l_1 l_2 00 | l_3 0 \rangle \langle l_1 l_2 m_1 m_2 | l_3 m_3 \rangle. \qquad (2.49)$$

With this equation and an explicit listing of the Clebsch-Gordan coefficients [2.14], we obtain the following matrix elements

<u>O-branch</u> ($l = l_1 = l_3+2$)

$$\langle v' l-2, m' | p_x | v l m \rangle = \frac{\epsilon_0 E_0}{2} \gamma_{v'}^{v} \left[-\delta_{m-1,m'} \left(\frac{(l^2-m^2)(l+m-1)(l+m-2)}{(2l-1)^2(2l+1)(2l-3)} \right)^{0.5} + \delta_{m+1,m'} \left(\frac{(l^2-m^2)(l-m-1)(l-m-2)}{(2l-1)^2(2l+1)(2l-3)} \right)^{0.5} \right] \qquad (2.50a)$$

$$\langle v' l-2, m' | p_y | v l m \rangle = -i\frac{\epsilon_0 E_0}{2} \gamma_{v'}^{v} \left[\delta_{m-1,m'} \left(\frac{(l^2-m^2)(l+m-1)(l+m-2)}{(2l-1)^2(2l+1)(2l-3)} \right)^{0.5} + \delta_{m+1,m'} \left(\frac{(l^2-m^2)(l-m-1)(l-m-2)}{(2l-1)^2(2l+1)(2l-3)} \right)^{0.5} \right] \qquad (2.50b)$$

$$\langle v' l-2, m' | p_z | v l m \rangle = \epsilon_0 E_0 \gamma_{v'}^{v} \delta_{m,m'} \left(\frac{(l^2-m^2)[(l-1)^2-m^2]}{(2l-1)^2(2l+1)(2l-3)} \right)^{0.5} \qquad (2.50c)$$

<u>Q-branch</u> ($l = l_1 = l_3$)

$$\langle v' l m' | p_x | v l m \rangle = \frac{\epsilon_0 E_0}{2} \gamma_{v'}^{v} \left[\delta_{m-1,m'} (2m-1) \frac{[(l-m+1)(l+m)]}{(2l-1)(2l+3)}^{0.5} \right.$$

$$+ \delta_{m+1,m'}(2m+1)\frac{[(l+m+1)(l-m)]^{0.5}}{(2l-1)(2l+3)}\Bigg] \qquad (2.51a)$$

$$\langle v'lm'|p_y|vlm\rangle = i\frac{\epsilon_0 E_0}{2}\gamma^v_{v'}\Bigg[\delta_{m-1,m'}(2m-1)\frac{[(l-m+1)(l+m)]^{0.5}}{(2l-1)(2l+3)}$$

$$- \delta_{m+1,m'}(2m+1)\frac{[(l+m+1)(l-m)]^{0.5}}{(2l-1)(2l+3)}\Bigg] \qquad (2.51b)$$

$$\langle v'lm'|p_z|vlm\rangle = \epsilon_0 E_0 \delta_{m,m'}\left[a^v_{v'} - \frac{2}{3}\gamma^v_{v'}\frac{3m^2-l(l+1)}{(2l-1)(2l+3)}\right] \qquad (2.51c)$$

S-branch ($l = l_1 = l_3-2$)

$$\langle v'l+2,m'|p_x|vlm\rangle = \frac{\epsilon_0 E_0}{2}\gamma^v_{v'}\Bigg[\delta_{m-1,m'}\left[\frac{[(l+1)^2-m^2](l-m+2)(l-m+3)}{(2l+1)(2l+3)^2(2l+5)}\right]^{0.5}$$

$$- \delta_{m-1,m'}\left[\frac{[(l+1)^2-m^2](l+m+2)(l+m+3)}{(2l+1)(2l+3)^2(2l+5)}\right]^{0.5}\Bigg] \qquad (2.52a)$$

$$\langle v'l+2,m'|p_y|vlm\rangle = i\frac{\epsilon_0 E_0}{2}\gamma^v_{v'}\Bigg[\delta_{m-1,m'}\left[\frac{[(l+1)^2-m^2](l-m+2)(l-m+3)}{(2l+1)(2l+3)^2(2l+5)}\right]^{0.5}$$

$$+ \delta_{m-1,m'}\left[\frac{[(l+1)^2-m^2](l+m+2)(l+m+3)}{(2l+1)(2l+3)^2(2l+5)}\right]^{0.5}\Bigg] \qquad (2.52b)$$

$$\langle v'l+2,m'|p_z|vlm\rangle = \epsilon_0 E_0 \gamma^v_{v'}\delta_{m,m'}\left[\frac{[(l+2)^2-m^2][(l+1)^2-m^2]}{(2l+1)(2l+3)^2(2l+5)}\right]^{0.5}. \qquad (2.52c)$$

All other matrix elements are zero, confirming the selection rule for the rotational quantum number (Eq. (2.29a)). Equivalent to the classical orientational average of p^2, we sum the squared matrix elements over all initial and final orientational (magnetic) quantum numbers m, m' and dividing by the number of initial states (2l+1) we obtain the average molecular cross section of a dilute gas as

$$\frac{d\sigma}{d\Omega} = \frac{\pi^2}{\lambda^4} \frac{1}{2l+1} \sum_{j=x,y,z} \sum_{m} \sum_{m'} |\epsilon_j \langle v'l'm'|p_j|vlm\rangle|^2 \quad . \tag{2.53}$$

An evaluation of the explicit expressions in Eq.'s (2.50-2.52) yields

$$\frac{d\sigma}{d\Omega} = \frac{\pi^2}{\lambda^4}\left(\frac{1}{15} b_{l'}^{l} (\gamma_{v'}^{v})^2 (\epsilon_x^2+\epsilon_y^2) + (\delta_{l,l'} (a_{v'}^{v})^2 + \frac{4}{45} b_{l'}^{l} (\gamma_{v'}^{v})^2)\epsilon_z^2\right), \tag{2.54}$$

where the Placzek-Teller coefficients $b_{l'}^{l}$, are given by above calculation as

<u>O-branch</u>

$$b_{l-2}^{l} = \frac{3}{2} \frac{l(l-1)}{(2l+1)(2l-1)} , \tag{2.55a}$$

<u>Q-branch</u>

$$b_{l}^{l} = \frac{l(l+1)}{(2l-1)(2l+3)} \qquad \text{and} \tag{2.55b}$$

<u>S-branch</u>

$$b_{l+2}^{l} = \frac{3}{2} \frac{(l+1)(l+2)}{(2l+1)(2l+3)} . \tag{2.55c}$$

These results are a special case of the more general results for symmetric top molecules, which can be found in references [2.6] and [2.15]. Further, we note that the sum of the O-, Q- and S-branch cross sections, for $l \to \infty$, converges towards the classical cross section, given by Eq. (2.44). Equations (2.54) and (2.55) give the average cross section of a single vibrational-rotational line, which corresponds to the sum over the cross sections of all initial and final m levels, divided by the number of initial levels (Eq. (2.53)). In the presence of a strong electrical field the (2l+1)-fold degeneracy of the rotational states is lifted with the exception of the ± m two-fold degeneracy. Therefore we have to use Eq.'s (2.50 - 2.52) to calculate cross sections for the individual m sublevels. In this context it makes sense to define the fractional cross section $F_{v'l'm'}^{vlm}$ as the ratio of the cross section of an individual transition

$v'l'm' \leftarrow vlm$ over the total cross section of the unresolved line $v'l' \leftarrow vl$. The fractional cross section can be written as

$$F^{vlm}_{v'l'm'} = \frac{\sum_{j=x,y,z} |\epsilon_j \langle v'l'm'|p_j|vlm\rangle|^2}{\sum_{j=x,y,z} \sum_m \sum_{m'} |\epsilon_j \langle v'm'|p_j|vlm\rangle|^2}, \tag{2.56a}$$

with

$$\sum_m \sum_{m'} F^{vlm}_{v'l'm'} = 1. \tag{2.56b}$$

With the help of Eq.'s (2.50 - 2.52) and (2.54, 2.55), Eq. (2.56a) can be easily evaluated for any combination of transition and detected polarization direction $\hat{\epsilon}$. Therefore we will give explicit expressions only for $\hat{\epsilon} = (0, 0, \epsilon_z)$, i. e. parallel to the polarization of the incoming light, as needed for our experiments. In this case we have $\Delta m = 0$, and the fractional cross sections for the degenerate levels +m and -m are identical ($F^{vlm}_{v'l'm} = F^{vl,-m}_{v'l',-m}$) (Eq.'s (2.50c, 2.51c and 2.52c)). Taking advantage of these degeneracies we define a new fractional cross section $Fs^{vlm}_{v'l'm'}$ as

$$Fs^{vlm}_{v'l'm'} = F^{vlm}_{v'l'm} + F^{vl,-m}_{v'l',-m} = 2F^{vlm}_{v'l'm}. \tag{2.57}$$

The explicit calculation for the different Raman branches yields with $\hat{\epsilon} = (0, 0, \epsilon_z)$

<u>O-branch</u>

$$Fs^{l,m}_{l-2,m} = \frac{15(2-\delta_{m,0})}{2} \frac{(l^2-m^2)[(l-1)^2-m^2]}{l(l-1)(2l-3)(4l^2-1)} \tag{2.58a}$$

<u>Q-branch</u>

$$Fs^{vlm}_{v'lm} = \frac{(2-\delta_{m,0})}{2l+1} \frac{[\alpha^v_{v'} - \frac{2}{3}\gamma^v_{v'} \frac{3m^2-l(l+1)}{(2l-1)(2l+3)}]^2}{(a^v_{v'})^2 + \frac{4}{45}(\gamma^v_{v'})^2 \frac{l(l+1)}{(2l-1)(2l+3)}}. \tag{2.58b}$$

S-branch

$$Fs^{l,m}_{l+2,m} = \frac{15(2-\delta_{m,0})}{2} \frac{[(l+2)^2-m^2)][(l+1)^2-m^2]}{(l+1)(l+2)(2l+1)(2l+3)(2l+5)}. \qquad (2.58c)$$

The resulting numerical values for the Q-branch are listed in table 2.3. Equations (2.58a-c) agree with those given by W.M. Huo [2.12], with the exception of the sign in front of the $\frac{2}{3}$ in Eq. (2.58b).

The total power P from a single vibrational-rotational transition $v',l' \leftarrow v,l$, which is observed in a solid angle Ω with an analyser polarization $\hat{\epsilon}$ can now be written as

$$\frac{dP}{d\Omega} = n_{vl} I_0 \frac{d\sigma}{d\Omega}, \qquad (2.59)$$

where n_{vl}, the number of molecules in the initial state $|v,l\rangle$ in the observation region, can be calculated from Eq. (2.20b) and the differential cross section $\frac{d\sigma}{d\Omega}$ is given by Eq. (2.54). If we are only interested in the transition between two orientational sublevels, the right side of Eq. (2.59) has to be multiplied by the appropriate coefficient $F^{vlm}_{v'l'm}$, (Eq. (2.56a)).

Table 2.3. Stark coefficients $\beta^{0,1,m}_{1,1,m}(mm^2J^{-1})$ and relative transition strengths $Fs^{0,1,m}_{1,1,m}$ for some lines in the Q-branch of N_2.

l	m	$\beta^{0,1,m}_{1,1,m}\left[\frac{mm^2}{J}\right]$	$Fs^{0,1,m}_{1,1,m}$	l	m	$\beta^{0,1,m}_{1,1,m}\left[\frac{mm^2}{J}\right]$	$Fs^{0,1,m}_{1,1,m}$
0	0	-0.46731	1.00000	9	0	-0.57008	0.07181
1	0	-0.63050	0.53309	9	1	-0.56665	0.14214
1	1	-0.38573	0.46691	9	2	-0.55639	0.13774
2	0	-0.58386	0.28326	9	3	-0.53928	0.13057
2	1	-0.52559	0.47319	9	4	-0.51533	0.12084
2	2	-0.35077	0.24355	9	5	-0.48453	0.10889
3	0	-0.57609	0.19810	9	6	-0.44689	0.09513
3	1	-0.54890	0.36466	9	7	-0.40241	0.08007
3	2	-0.46733	0.27786	9	8	-0.35109	0.06430
3	3	-0.33138	0.15938	9	9	-0.29292	0.04851
4	0	-0.57326	0.15289	10	0	-0.56990	0.06495
4	1	-0.55737	0.29137	10	1	-0.56711	0.12879
4	2	-0.50971	0.25022	10	2	-0.55872	0.12554
4	3	-0.43027	0.18859	10	3	-0.54475	0.12020
4	4	-0.31906	0.11693	10	4	-0.52519	0.11292
5	0	-0.57189	0.12463	10	5	-0.50005	0.10390
5	1	-0.56144	0.24148	10	6	-0.46931	0.09338
5	2	-0.53007	0.21888	10	7	-0.43298	0.08167
5	3	-0.47781	0.18368	10	8	-0.39107	0.06914
5	4	-0.40463	0.13958	10	9	-0.34357	0.05620
5	5	-0.31055	0.09176	10	10	-0.29048	0.04332
6	0	-0.57111	0.10524	11	0	-0.56977	0.05928
6	1	-0.56370	0.20580	11	1	-0.56745	0.11773
6	2	-0.54146	0.19209	11	2	-0.56047	0.11525
6	3	-0.50441	0.17029	11	3	-0.54885	0.11117
6	4	-0.45254	0.14198	11	4	-0.53258	0.10559
6	5	-0.38584	0.10935	11	5	-0.51165	0.09862
6	6	-0.30432	0.07526	11	6	-0.48608	0.09043
7	0	-0.57063	0.09109	11	7	-0.45586	0.08121
7	1	-0.56509	0.17915	11	8	-0.42099	0.07118
7	2	-0.54850	0.17022	11	9	-0.38146	0.06062
7	3	-0.52084	0.15584	11	10	-0.33729	0.04981
7	4	-0.48212	0.13678	11	11	-0.28847	0.03911
7	5	-0.43234	0.11410	12	0	-0.56967	0.05453
7	6	-0.37150	0.08917	12	1	-0.56770	0.10840
7	7	-0.29959	0.06366	12	2	-0.56181	0.10647
8	0	-0.57030	0.08030	12	3	-0.55199	0.10329
8	1	-0.56602	0.15854	12	4	-0.53823	0.09892
8	2	-0.55315	0.15240	12	5	-0.52055	0.09343
8	3	-0.53171	0.14244	12	6	-0.49894	0.08694
8	4	-0.50170	0.12906	12	7	-0.47341	0.07958
8	5	-0.46311	0.11283	12	8	-0.44394	0.07148
8	6	-0.41594	0.09447	12	9	-0.41054	0.06283
8	7	-0.36020	0.07487	12	10	-0.37322	0.05382
8	8	-0.29589	0.05509	12	11	-0.33197	0.04467
				12	12	-0.28678	0.03563

2.1.7 Stark Effect

The influence of strong electrical fields, either dc (external field) or at optical frequencies (laser field), on molecules leads to Stark effect, i. e. a shift of molecular energy levels as a function of the electrical field. As discussed in section 2.1.5, homonuclear molecules do not have a permanent electrical dipole moment and the first order Stark effect is zero. Therefore we must consider the magnitude of the induced dipole moment $p_0 = \epsilon_0 \alpha E_0$ (Eq. (2.27c)). We calculate the energy of the molecule in a dc electrical field with the help of

$$W = -\epsilon_0 \alpha \int_0^{E_{dc}} E \, dE, \tag{2.60}$$

to be

$$W = -\frac{1}{2}\epsilon_0 \alpha E_{dc}^2. \tag{2.61}$$

For an optical electrical field we replace E_{dc}^2 with the average of the squared electrical field $\langle E^2 \rangle = \frac{1}{2} E_0^2$ (Eq. (2.27a)) and obtain (Eq. (2.27c))

$$W = -\frac{1}{4} \vec{p}_0 \cdot \vec{E}_0 = -\frac{1}{4} p_z E_z, \tag{2.62}$$

recalling that $\vec{E} = (0, 0, E_z)$ (Eq. (2.38)).

Quantum mechanically we have to replace p_z by the corresponding matrix element $\langle vlm|p_z|vlm \rangle$, which has been calculated previously (Eq. (2.51c)). Remembering $I = \frac{1}{2} c \epsilon_0 E_0^2$ (Eq. (2.32b)), we can write the resulting shift of the energy level W as

$$W = \frac{-I}{2c} \left[a_v^v - \frac{2}{3} \gamma_v^v \frac{3m^2 - l(l+1)}{(2l-1)(2l+3)} \right], \tag{2.63}$$

in disagreement with W.M. Huo's result [2.12]. This disagreement seems to be due to an inconsistent definition of a in Huo's work. As one can see from Eq. (2.63), the Stark shift is proportional to the square of the electrical field or intensity, we are dealing with quadratic, or second order Stark effect. For a transition from a lower energy level v,l,m to a higher level v',l',m' the resulting shift of the transition frequency is

$$\Delta\nu = \frac{1}{h}(W_{v',l',m'} - W_{v,l,m})$$
$$= \frac{-I}{2hc}\left[a_{v'}^{v'} - a_{v}^{v} - \frac{2}{3}\gamma_{v'}^{v'}\frac{3m'^2-l'(l'+1)}{(2l'-1)(2l'+3)} + \frac{2}{3}\gamma_{v}^{v}\frac{3m^2-l(l+1)}{(2l-1)(2l+3)}\right], \quad (2.64)$$

where h is Planck's constant. For the Q-branch this equation simplifies to

$$\Delta\nu = \frac{-I}{2hc}\left[a_{v'}^{v'} - a_{v}^{v} - \frac{2}{3}\left(\gamma_{v'}^{v'} - \gamma_{v}^{v}\right)\frac{3m^2-l(l+1)}{(2l-1)(2l+3)}\right]. \quad (2.65)$$

Now we define the Stark coefficient β as

$$\beta_{v'l'm'}^{vlm} = \frac{\Delta\nu}{I}, \quad (2.66)$$

and the resulting Stark coefficients β_{11m}^{01m} for non-depolarized ($\vec{\epsilon} = (0,0,\epsilon_z)$) Q-branch transitions in molecular nitrogen are listed in table 2.3.

2.2 Coherent Raman Spectroscopy

In section 2.1 we assume that the susceptibility χ is independent of the electrical field strength. For large fields (lasers) this assumption is no longer justified and we expand χ in terms of the electrical field as

$$\chi = \chi^{(1)} + \chi^{(2)}E + \chi^{(3)}E^2 + \ldots, \quad (2.67)$$

where the n^{th} order term $\chi^{(n)}$ is a tensor of rank n+1. The first order term $\chi^{(1)}$ is related to its microscopic equivalent, the previously used linear polarizability α by

$$\chi^{(1)} = N \alpha, \tag{2.68}$$

where $N = N_g - N_e$, is the difference between the molecular number density in the ground state N_g and the excited state N_e. $\chi^{(1)}$ is the origin of various physical processes leading to spontaneous light scattering (Raman, Rayleigh, etc), absorption and refraction. The second order of χ is associated with various nonlinear effects related to second harmonic generation. $\chi^{(2)}$, however, equals zero for all media which exhibit inversion symmetry, such as gases, liquids and many solids [2.16]. The third order nonlinear susceptibility $\chi^{(3)}$ is associated with high frequency phenomena arising from electronic motion, such as third harmonic generation, two photon absorption, and with low frequency phenomena arising from nuclear motion, such as the various types of coherent light scattering. In what follows we exclusively discuss the slow phenomena, exemplified by coherent Raman scattering.

2.2.1 Basic Theory

First we derive the third order nonlinear polarization and its associated third order nonlinear susceptibility $\chi^{(3)}$ in terms of the linear polarizability α [2.16]. Making use of the summation convention (implicit summation over repeated indices) we write the induced linear molecular dipole moment p (Eq. (2.26)) in vector and tensor components as

$$p_k = \epsilon_0 \alpha_{kl} E_l . \tag{2.69}$$

The interaction energy W of this molecular dipole with an electrical field E_k is

$$W = -\frac{1}{2} p_k E_k = -\frac{1}{2} \epsilon_0 \alpha_{kl} E_k E_l . \tag{2.70}$$

In the case of a Raman process, α has to be replaced by $(\partial\alpha/\partial q)q$ (Eq. (2.28)). A force, acting upon the generalized coordinate q, is associated with the interaction energy W and can be written as

$$F = -\frac{\partial W}{\partial q} = \frac{1}{2} \epsilon_0 \alpha'_{kl} E_k E_l , \tag{2.71}$$

where α' is defined as $\alpha' = (\partial\alpha/\partial q)$. Now consider an electrical field consisting of two frequency components

$$E_i(t) = \frac{1}{2}\left[E_i(\omega_1)\, e^{-i\omega_1 t} + E_i(\omega_2)\, e^{-i\omega_2 t} + \text{c.c.} \right], \tag{2.72}$$

where $\omega_2 > \omega_1$ and c.c. stands for complex conjugate terms. Substituting this expression into Eq. (2.71) and keeping only the low frequency (Raman) terms at $\pm(\omega_2 - \omega_1)$, which drive the molecular oscillation, the force becomes

$$F = \frac{1}{4} \epsilon_0 \alpha'_{kl} \left[E_k^*(\omega_1) E_l(\omega_2)\, e^{-i(\omega_2 - \omega_1)t} + \text{c.c.} \right]. \tag{2.73}$$

We model the molecule by a damped harmonic oscillator with a characteristic frequency Δ and a damping constant 2γ, driven by the force F. For an oscillator of unit mass the equation of motion becomes

$$\frac{\partial^2 q}{\partial t^2} + 2\gamma \frac{\partial q}{\partial t} + \Delta^2 q = F. \tag{2.74}$$

The ansatz

$$q(t) = \frac{1}{2}\left[q_0\, e^{-i\omega t} + q_0^*\, e^{i\omega t} \right], \quad \omega = \omega_2 - \omega_1, \quad \omega_2 > \omega_1, \tag{2.75}$$

and replacing $\omega + \Delta$ by 2Δ yields

$$q_0 = \frac{\epsilon_0}{4\Delta}\,\alpha'_{kl}\left[\frac{E_k^*(\omega_1)E_l(\omega_2)}{(\Delta - \omega) - i\gamma}\right]. \tag{2.76}$$

Substituting Eq. (2.72) and Eq. (2.75) into Eq. (2.69), with $\alpha_{kl} = \alpha'_{kl}q$, results in

$$p_i(t) = \frac{\epsilon_0}{2}\,\alpha'_{ij}\Big[q_0^*E_j(\omega_1)e^{-i(2\omega_1-\omega_2)t} + q_0E_j(\omega_1)e^{-i\omega_2 t} + q_0E_j(\omega_2)e^{-i(2\omega_2-\omega_1)t} + q_0^*E_j(\omega_2)e^{-i\omega_1 t} + \text{c.c.}\Big]. \tag{2.77}$$

With a molecular dipole moment $p_i(t)$ written as

$$p_i(t) = \frac{1}{2}\left[\sum_n p_i(\omega_n)\,e^{-i\omega_n t} + \text{c.c.}\right], \qquad n = 1, 2, 3, 4 \tag{2.78}$$

we find amplitudes $p_i(\omega_n)$ at four different frequencies ω_1, ω_2, $\omega_3 = 2\omega_1-\omega_2$, $\omega_4 = 2\omega_2-\omega_1$ as

$$p_i(\omega_1) = \frac{\epsilon_0^2}{8\Delta}\,\alpha'_{ij}\alpha'_{kl}\,\frac{E_j(\omega_2)E_k(\omega_1)E_1^*(\omega_2)}{(\Delta - \omega) + i\gamma}\,, \tag{2.79a}$$

$$p_i(\omega_2) = \frac{\epsilon_0^2}{8\Delta}\,\alpha'_{ij}\alpha'_{kl}\,\frac{E_j(\omega_1)E_k^*(\omega_1)E_1(\omega_2)}{(\Delta - \omega) - i\gamma}\,, \tag{2.79b}$$

$$p_i(\omega_3) = \frac{\epsilon_0^2}{8\Delta}\,\alpha'_{ij}\alpha'_{kl}\,\frac{E_j(\omega_1)E_k(\omega_1)E_1^*(\omega_2)}{(\Delta - \omega) + i\gamma} \quad \text{and} \tag{2.79c}$$

$$p_i(\omega_4) = \frac{\epsilon_0^2}{8\Delta}\,\alpha'_{ij}\alpha'_{kl}\,\frac{E_j(\omega_2)E_k^*(\omega_1)E_1(\omega_2)}{(\Delta - \omega) - i\gamma}\,. \tag{2.79d}$$

These equations express the polarization of a single molecule in terms of the derivative of the linear molecular polarizability tensor α', written in laboratory coordinates. The tensor α' is given for a diatomic molecule in molecular coordinates by Eq. (2.34). We use Eq.'s (2.35-2.37) for the transformation into laboratory coordinates

$$\alpha'_{lab} = \eta^{-1}\alpha'_{mol}\eta, \tag{2.80}$$

yielding the explicit expression for α' as

$$\alpha' = \tag{2.81}$$

$$\begin{pmatrix} (\alpha'_{\parallel}-\alpha'_{\perp})\sin^2\theta\cos^2\phi+\alpha'_{\perp} & (\alpha'_{\parallel}-\alpha'_{\perp})\sin^2\theta\sin\phi\cos\phi & (\alpha'_{\parallel}-\alpha'_{\perp})\sin\theta\cos\theta\cos\phi \\ (\alpha'_{\parallel}-\alpha'_{\perp})\sin^2\theta\sin\phi\cos\phi & (\alpha'_{\parallel}-\alpha'_{\perp})\sin^2\theta\sin^2\phi+\alpha'_{\perp} & (\alpha'_{\parallel}-\alpha'_{\perp})\sin\theta\cos\theta\sin\phi \\ (\alpha'_{\parallel}-\alpha'_{\perp})\sin\theta\cos\theta\cos\phi & (\alpha'_{\parallel}-\alpha'_{\perp})\sin\theta\cos\theta\sin\phi & (\alpha'_{\parallel}-\alpha'_{\perp})\cos^2\theta+\alpha'_{\perp} \end{pmatrix},$$

where the angles θ and ϕ are defined by Eq. (2.36) and Fig. 2.5. For dilute gases we can define the macroscopic third order nonlinear polarization per unit volume $P_i^{(3)}$ as the sum of the individual polarizations divided by the volume

$$P_i^{(3)} = \frac{1}{V} \sum_{m=1,n} p_{i_m}, \tag{2.82}$$

where n is the number of molecules contained in the volume V. Similarly we define a macroscopic third order nonlinear susceptibility per unit volume $\chi^{(3)}$ as

$$\chi_{ijkl}^{(3)} = \frac{\epsilon_0}{8\Delta} [(\Delta - \omega) - i\gamma]^{-1} \frac{1}{V} \sum_{m=1,n} \alpha'_{ij_m} \alpha'_{kl_m}, \tag{2.83a}$$

where $\omega = \omega_2 - \omega_1$ is positive. This $\chi_{ijkl}^{(3)}$ is a result of our specific model and is related to the general definition [2.17] of the third order nonlinear susceptibility by

$$\begin{aligned} \chi_{ijkl}^{(3)} &= \chi_{ijkl}^{(3)*}(-\omega_1,\omega_2,\omega_1,-\omega_2) = \chi_{ijkl}^{(3)}(-\omega_2,\omega_1,-\omega_1,\omega_2) \\ &= \chi_{ijkl}^{(3)*}(-\omega_3,\omega_1,\omega_1,-\omega_2) = \chi_{ijkl}^{(3)*}(-\omega_4,\omega_2,-\omega_1,\omega_2). \end{aligned} \tag{2.83b}$$

The macroscopic third order nonlinear polarization can now be written as

$$P_i(t) = \frac{1}{2}\left[\sum_n P_i(\omega_n)\, e^{-i\omega_n t} + \text{c.c.}\right], \qquad n = 1, 2, 3, 4 \tag{2.84a}$$

$$P_i^{(3)}(\omega_1) = \epsilon_0\, \chi_{ijkl}^{(3)*}\, E_j(\omega_2) E_k(\omega_1) E_l^*(\omega_2), \tag{2.84b}$$

$$P_i^{(3)}(\omega_2) = \epsilon_0\, \chi_{ijkl}^{(3)}\, E_j(\omega_1) E_k^*(\omega_1) E_l(\omega_2), \tag{2.84c}$$

$$P_i^{(3)}(\omega_3) = \epsilon_0 \chi_{ijkl}^{(3)*} E_j(\omega_1) E_k(\omega_1) E_l^*(\omega_2), \tag{2.84d}$$

$$P_i^{(3)}(\omega_4) = \epsilon_0 \chi_{ijkl}^{(3)} E_j(\omega_2) E_k^*(\omega_1) E_l(\omega_2), \tag{2.84e}$$

where $\omega_3 = 2\omega_1 - \omega_2$ and $\omega_4 = 2\omega_2 - \omega_1$. Again we limit the discussion to dilute gases with randomly oriented molecules.

Classically we obtain $\chi^{(3)}$ by taking the orientational average $\langle \alpha'_{ij} \alpha'_{kl} \rangle$ according to Eq. (2.41) and setting

$$\frac{1}{V} \sum_{m=1,n} \alpha'_{ij_m} \alpha'_{kl_m} = N \langle \alpha'_{ij} \alpha'_{kl} \rangle, \tag{2.85}$$

with $N = n/V$. $\chi^{(3)}$ can now be written as

$$\chi_{ijkl}^{(3)} = A \langle \alpha'_{ij} \alpha'_{kl} \rangle, \tag{2.86}$$

with $A = N \frac{\epsilon_0}{8\Delta} [(\Delta - \omega) - i\gamma]^{-1}$. $\chi^{(3)}$ is a fourth rank tensor in three dimensions and has therefore 81 elements. The explicit calculation of these 81 elements in terms of α' (Eq. (2.81)) yields 21 non-vanishing elements, some of which are given by

$$\chi_{1111}^{(3)} = A \left(a^2 + \frac{4}{45} \gamma^2\right), \tag{2.87a}$$

$$\chi_{1122}^{(3)} = A \left(a^2 - \frac{2}{45} \gamma^2\right), \tag{2.87b}$$

$$\chi_{1212}^{(3)} = \chi_{1221}^{(3)} = A \frac{1}{15} \gamma^2, \tag{2.87c}$$

with $a = (\alpha_{\parallel} + 2\alpha_{\perp})/3$ and $\gamma = \alpha_{\parallel} - \alpha_{\perp}$ (Eq. (2.45)). The other non-zero elements are related to $\chi_{1111}^{(3)}$, $\chi_{1122}^{(3)}$, $\chi_{1212}^{(3)}$ and $\chi_{1221}^{(3)}$ by

$$\chi_{1111}^{(3)} = \chi_{2222}^{(3)} = \chi_{3333}^{(3)}, \tag{2.88a}$$

$$\chi_{1122}^{(3)} = \chi_{1133}^{(3)} = \chi_{2211}^{(3)} = \chi_{2233}^{(3)} = \chi_{3311}^{(3)} = \chi_{3322}^{(3)}, \tag{2.88b}$$

$$\chi_{1212}^{(3)} = \chi_{1313}^{(3)} = \chi_{2121}^{(3)} = \chi_{2323}^{(3)} = \chi_{3131}^{(3)} = \chi_{3232}^{(3)} \tag{2.88c}$$

$$\chi_{1221}^{(3)} = \chi_{1331}^{(3)} = \chi_{2112}^{(3)} = \chi_{2332}^{(3)} = \chi_{3113}^{(3)} = \chi_{3223}^{(3)}. \tag{2.88d}$$

These relations (2.88) can be obtained alternatively from symmetry considerations for isotropic media [2.18]. These considerations also yield the condition [2.18]

$$\chi^{(3)}_{1111} = \chi^{(3)}_{1122} + \chi^{(3)}_{1212} + \chi^{(3)}_{1221}, \qquad (2.89)$$

which is obviously fulfilled by our results. Compared to the relations derived from symmetry conditions (2.88, 2.89), our model yields an additional equality, $\chi^{(3)}_{1212} = \chi^{(3)}_{1221}$ as given in Eq. (2.87c). This additional condition equates the tensor elements in Eq. (2.88c) to those in Eq. (2.88d), making all 21 non-zero elements expressible in terms of two independent elements instead of three for general isotropic media. Physically, this additional condition is a consequence of the fact that our α' tensor is symmetric and our medium is not optically active. This result is in agreement with the corresponding nonlinear susceptibility tensor components for purely optical effects under the Born-Oppenheimer approximation, as discussed by R.W. Hellwarth [2.19].

Quantum mechanically the orientational average is replaced by a summation over the orientational (magnetic) sublevels m of the respective rotational quantum number l (m = -l, -l+1,..., l-1, l). This procedure has been outlined in section 2.1.6 and will not be duplicated here. As a result of the quantum mechanical calculation, $\chi^{(3)}$ is modified by the Placzek-Teller coefficients and its components may be written as

$$\chi^{(3)}_{1111} = A\,(a^2 + \frac{4}{45}\, b^1_1,\gamma^2), \qquad (2.90a)$$

$$\chi^{(3)}_{1122} = A\,(a^2 - \frac{2}{45}\, b^1_1,\gamma^2), \qquad (2.90b)$$

$$\chi^{(3)}_{1212} = \chi^{(3)}_{1221} = A\,\frac{1}{15}\, b^1_1,\gamma^2, \qquad (2.90c)$$

where the Placzek-Teller coefficients b^1_1, are given by Eq. (2.55). Since there are only two independent elements, the above formulae may be checked easily by comparison with Eq. (2.53) and Eq. (2.54), which

effectively calculate $\chi^{(3)}_{1111}$ and $\chi^{(3)}_{1212}$. To calculate $\chi^{(3)}$ for vibrational Raman scattering, we have to remember that for Raman scattering a and γ have to be replaced by $\frac{\partial a}{\partial q}$ and $\frac{\partial \gamma}{\partial q}$, respectively. These quantities may be related to $a^{v}_{v'}$, $\gamma^{v}_{v'}$ (see Table 2.2) via Eq. (2.47), which yields an explicit expression for $\chi^{(3)}$

$$\chi^{(3)}_{1111} = \frac{\pi N \epsilon_0}{2h(\Delta\omega - i\gamma)} \left[(a^{v}_{v'})^2 + \frac{4}{45} b^{1}_{1'} (\gamma^{v}_{v'})^2 \right], \tag{2.90d}$$

where $a^{v}_{v'}$ and $\gamma^{v}_{v'}$ can be found in table 2.2 for the $v = 0 \rightarrow v = 1$ vibrational transition in molecular nitrogen.

To derive coherent Raman signals for plane waves from the induced polarizations, we write the one dimensional wave equation as

$$\frac{\partial^2 E_i(t)}{\partial z^2} - \frac{1}{c^2} \frac{\partial^2 E_i(t)}{\partial t^2} = \frac{1}{\epsilon_0 c^2} \frac{\partial^2 P^{(3)}_i(t)}{\partial t^2} \tag{2.91}$$

with $P^{(3)}_i(t) = P^{(3)}_i(\omega_n)\, e^{i(k_p z - \omega_n t)}$, $E_i(t) = E_i(\omega_n, z)\, e^{i(k_n z - \omega_n t)}$, $\frac{\partial^2 E_i(t)}{\partial z^2} = e^{i(k_n z - \omega_n t)} \left(\frac{\partial^2}{\partial z^2} + 2ik_n \frac{\partial}{\partial z} - k_n^2 \right) E_i(\omega_n, z)$, where k_p is the wave vector of the induced polarization. Using the slowly varying amplitude approximation

$$\frac{\partial^2 E}{\partial z^2} \ll k_n \frac{\partial E}{\partial z} \ll k_n^2 E \tag{2.92}$$

we neglect the second spatial derivative of the electrical field $\frac{\partial^2 E_i(\omega_n, z)}{\partial z^2}$ and write the result as

$$\frac{\partial E_i(\omega_n, z)}{\partial z} = \frac{ik_n}{2\epsilon_0} P^{(3)}_i(\omega_n)\, e^{i(k_p - k_n)z}. \tag{2.93}$$

First we deal with polarizations at the frequencies ω_1 and ω_2, for which $k_p = k_n$. Expressing the derivative of the intensity I (Eq.

(2.32b)) as $\frac{\partial I}{\partial z} = \frac{1}{2}\,\epsilon_0 c\left[E^* \frac{\partial E}{\partial z} + E \frac{\partial E^*}{\partial z}\right]$, we can write the intensity change as

$$\frac{\partial}{\partial z} I_i(\omega_n,z) = i \frac{ck_n}{4\epsilon_0} (E_i^* P_i - E_i P_i^*), \qquad n = 1, 2. \tag{2.94}$$

where we do not use the summation convention for the index i in Eq. (2.94) to Eq. (2.100). Inserting the explicit expressions for the polarization of the medium (Eq. (2.84b,c)) this becomes

$$\frac{\partial}{\partial z} I_i(\omega_1,z) = i \frac{ck_1\epsilon_0}{4} \left[\chi^{(3)*}_{ijkl} E_i^*(\omega_1) E_j(\omega_2) E_k(\omega_1) E_l^*(\omega_2) - \text{c.c.}\right], \tag{2.95a}$$

$$\frac{\partial}{\partial z} I_i(\omega_2,z) = i \frac{ck_2\epsilon_0}{4} \left[\chi^{(3)}_{ijkl} E_i^*(\omega_2) E_j(\omega_1) E_k^*(\omega_1) E_l(\omega_2) - \text{c.c.}\right]. \tag{2.95b}$$

For two polarization directions of the electrical field, one at ω_1 and one at ω_2 these equations simplify to

$$\frac{\partial}{\partial z} I_i(\omega_1,z) = \frac{2k_1}{c\epsilon_0} \chi''_{ijij} I_i(\omega_1) I_j(\omega_2) \text{ and} \tag{2.96a}$$

$$\frac{\partial}{\partial z} I_i(\omega_2,z) = -\frac{2k_1}{c\epsilon_0} \chi''_{ijji} I_i(\omega_2) I_j(\omega_1), \tag{2.96b}$$

with $\chi''_{ijij} = \chi''_{ijji}$. The third order nonlinear susceptibility $\chi^{(3)}$ has been written as the sum of real (χ') and imaginary part (χ'')

$$\chi^{(3)} = \chi' + i\,\chi'', \tag{2.97}$$

where χ'' takes the following form (Eq. (2.83a))

$$\chi'' = B \frac{\gamma}{(\Delta-\omega)^2 + \gamma^2}, \tag{2.98a}$$

$$\text{with} \quad B = \frac{\epsilon_0}{8V\Delta} \sum_{m=1,n} \alpha'_{ij_m} \alpha'_{kl_m}. \tag{2.98b}$$

Equations (2.96a,b) can easily be integrated with the assumption of no pump depletion, i.e. $I(\omega_2)$ is constant for Eq. (2.96a) and $I(\omega_1)$ is constant for Eq. (2.96b). The integration from z = 0 to z = l yields

$$I_i(\omega_1,l) = I_i(\omega_1,0) \exp[G_1 I_j(\omega_2) l], \tag{2.99a}$$

where l is the interaction length, $G_1 = \frac{2k_1}{c\epsilon_0}\chi''_{iijj}$ is the gain per unit length, and

$$I_i(\omega_2,l) = I_i(\omega_2,0)\ \exp[-G_2 I_j(\omega_1)l], \qquad (2.99b)$$

with $G_2 = \frac{2k_2}{c\epsilon_0}\chi''_{iijj}$

Under the small gain approximation ($G \ll 1$) the exponentials may be expanded as power series and Eq.'s (2.99a,b) become

$$I_i(\omega_1,l) = I_i(\omega_1,0)\ (1 + G_1 I_j(\omega_2)l) \qquad (2.100a)$$

$$I_i(\omega_2,l) = I_i(\omega_2,0)\ (1 - G_2 I_j(\omega_1)l) \qquad (2.100b)$$

Equations (2.100a) and (2.100b) describe a gain in intensity at ω_1, and a loss in intensity at ω_2, whose observation corresponds to stimulated Raman gain spectroscopy (SRGS) and inverse Raman spectroscopy (IRS), respectively. Both of these spectroscopies, which are often referred to as SRS (stimulated Raman spectroscopy), reveal the frequency dependence of the imaginary part of $\chi^{(3)}_{iijj}$; two independent elements, $\chi^{(3)}_{1111}$ and $\chi^{(3)}_{1122}$, can be measured with pump and probe beam polarized parallel or perpendicular to each other. Using more than one linear polarization per beam (elliptical polarization) leads us into the field of polarization Raman gain spectroscopies, which will not be treated in this thesis. Further information may be obtained from references [2.20, 2.21, 2.22].

Now we proceed to the polarizations at the frequencies $\omega_3=2\omega_1-\omega_2$ and $\omega_4=2\omega_2-\omega_1$ (Eq. (2.84d,e)). Integrating Eq. (2.93) under the assumption of undepleted laser beams from z = 0 to z = l results in

$$E_i(\omega_n,l) = \frac{k_n}{2\epsilon_0} P^{(3)}_i(\omega_n)\ \frac{e^{i(k_p-k_n)l}-1}{(k_p-k_n)l}\ l, \qquad n=3,4 \qquad (2.101)$$

where $k_p = 2k_1 - k_2$ for n = 3 and $k_p = 2k_2 - k_1$ for n=4. We take the absolute square and obtain the intensity I_i generated after an interaction length l as

$$I_i(\omega_3) = \frac{k_3^2}{c^2\epsilon_0^2} l^2 I_j(\omega_1)I_k(\omega_1)I_l(\omega_2) |\chi^{(3)}_{ijkl}|^2 \frac{\sin^2(\Delta kl/2)}{(\Delta kl/2)^2}, \qquad (2.102a)$$

with $\Delta k = k_p - k_3 = 2k_1 - k_2 - k_3$, and

$$I_i(\omega_4) = \frac{k_4^2}{c^2\epsilon_0^2} l^2 I_j(\omega_2)I_k(\omega_1)I_l(\omega_2) |\chi^{(3)}_{ijkl}|^2 \frac{\sin^2(\Delta kl/2)}{(\Delta kl/2)^2}, \qquad (2.102b)$$

with $\Delta k = k_p - k_4 = 2k_2 - k_1 - k_4$ and $\omega_2 > \omega_1$. In the case of strong dispersion the phase mismatch Δk is non-zero and the generated intensity oscillates and stays rather small for long interaction lengths. Phase matching ($\Delta k = 0$) occurs in dilute gases for parallel laser beams, while in the case of dispersive media the crossing angle of the laser beams has to be adjusted [2.23]. Equations (2.102a,b) both describe the generation of new beams at $\omega_3 = 2\omega_1 - \omega_2$ and $\omega_4 = 2\omega_2 - \omega_1$, corresponding to coherent Stokes Raman spectroscopy (CSRS) and coherent anti-Stokes Raman spectroscopy (CARS), respectively. Both spectroscopies are based on four-wave mixing processes and therefore dubbed four-wave mixing Raman spectroscopy (FWMRS). The signal is in both cases proportional to $\left|\chi^{(3)}_{ijkl}\right|^2$ and the absolute square of the individual tensor components may be measured.

2.2.2 Doppler Broadened Lineshapes

Coherent Raman signals are generated by the interaction of two laser beams with the third-order nonlinear susceptibility $\chi^{(3)}$ of a material. For an isolated Raman resonance, we have modeled the

associated vibrational mode by a damped harmonic oscillator with a resonance frequency Δ and a damping constant 2γ (Eq. (2.74)). The damping gives rise to a homogeneously broadened line with Lorentzian shape. Driving the oscillator at the difference frequency $(\omega_2-\omega_1)$ of the two laser beams, we have derived the Lorentzian spectrum of $\chi_L^{(3)}$ as (Eq. (2.86))

$$\chi_L^{(3)} = \frac{B}{\Delta\omega - i\gamma} , \tag{2.103}$$

where B is a constant (Eq. (2.98b)) and $\Delta\omega$ is defined as $\Delta\omega = \Delta - \omega = \Delta - (\omega_2 - \omega_1)$. Under the small-gain approximation, SRS signals are proportional to χ'', the imaginary part of $\chi^{(3)}$ (Eq. (2.99)), while FWMRS signals are proportional to the absolute square of $\chi^{(3)}$ (Eq. (2.102)). With the definition $\chi^{(3)}=\chi'+i\chi''$ (Eq. (2.97)) we can write

$$\chi_L' = B\frac{\Delta\omega}{\Delta\omega^2+\gamma^2} , \tag{2.104a}$$

$$\chi_L'' = B\frac{\gamma}{\Delta\omega^2+\gamma^2} , \tag{2.104b}$$

$$|\chi_L^{(3)}|^2 = B^2\frac{1}{\Delta\omega^2+\gamma^2} . \tag{2.104c}$$

The real and imaginary parts of $\chi_L^{(3)}$ are shown as solid curves in Fig. 2.5. As one can see, χ_L' has the shape of a typical dispersion curve with maxima and minima of $\pm\frac{B}{2\gamma}$ at $\Delta\omega = \gamma$, while χ_L'' has a Lorentzian line shape with a maximum of $\frac{B}{\gamma}$ at $\Delta\omega = 0$ and a half width at half maximum of γ (HWHM = γ). In these plots the peak height of χ_L'' is normalized to one. It is clear that χ_L'' is proportional to $|\chi_L^{(3)}|^2$, and therefore isolated SRS and FWMRS lines have identical Lorentzian shapes in the case of pure pressure (or homogeneous) broadening.

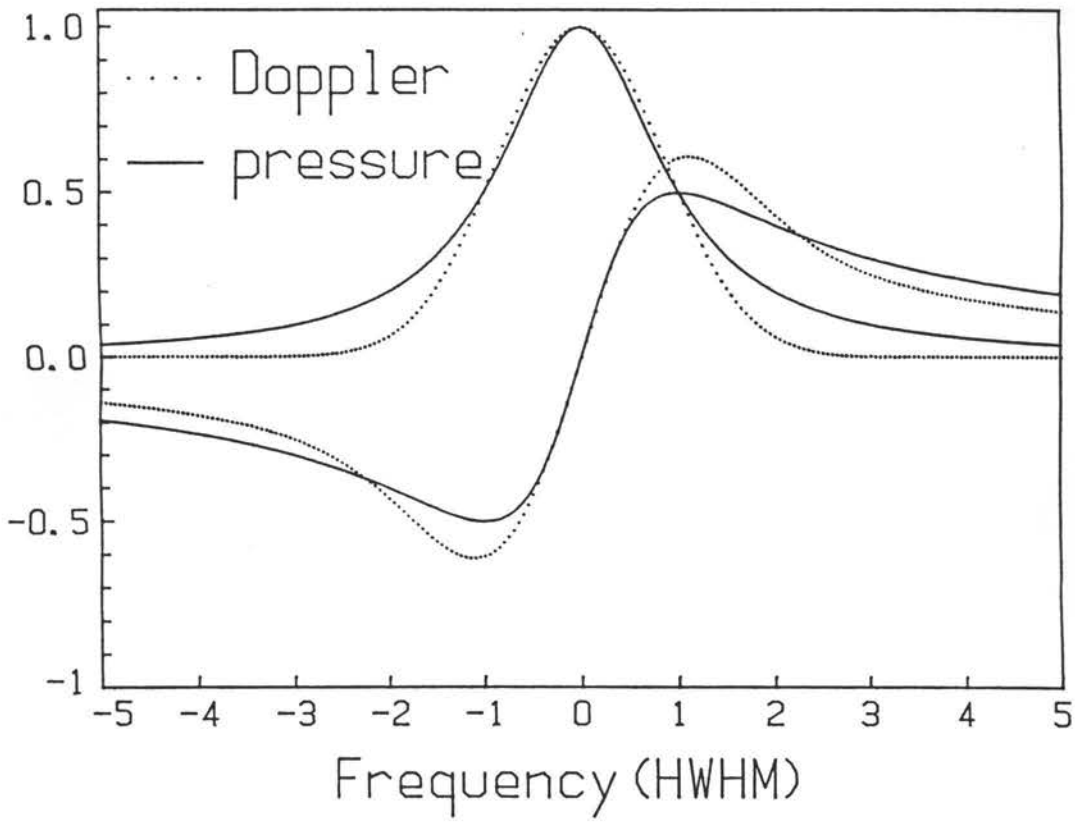

Fig. 2.5. Plots of the real (dispersion-shaped) and imaginary part of the third order nonlinear susceptibility for Doppler (dotted curves) and pressure (solid curves) broadening as a function of $\Delta\omega$

Now let us discuss the influence of Doppler broadening, using the Gaussian distribution

$$G(\omega-\omega_0) = e^{-a(\omega-\omega_0)^2}, \qquad (2.105)$$

with $a=\ln(2)/\delta\omega_D^2$, $\delta\omega_D$ being the HWHM (half-width at half maximum) of G. To calculate the correct line shapes, including both Doppler and

pressure broadening, we convolute the Lorentzian $\chi_L^{(3)}$ with the Gaussian G

$$\chi' = \chi_L' * G, \tag{2.106a}$$

$$\chi'' = \chi_L'' * G. \tag{2.106b}$$

The convolution integrals can be evaluated only numerically, with χ'' being described by the frequently used Voigt profile. We can gain some more insight into the effect of Doppler broadening on $\chi^{(3)}$ by considering the general expression (Eq. (2.106)) in the limit of zero pressure broadening, i.e., $\gamma \to 0$. In this case the Voigt profile of χ'' takes the Gaussian shape G, because the properly normalized χ_L'' is a δ function for $\gamma = 0$. To evaluate χ' in this limit of $\gamma = 0$ is more involved; it may be done using the techniques of Fourier transform. Since a convolution of two functions f*g is, in Fourier space, the multiplication of their Fourier transforms FT(f) FT(g), we can write

$$\chi' = FT^{-1}[FT(\chi_L') \; FT(G)]. \tag{2.107}$$

Defining the Fourier transforms as

$$H(\omega) = 1/2 \int_{-\infty}^{+\infty} h(t) e^{i\omega t} \, dt, \tag{2.108a}$$

$$h(t) = 1/\pi \int_{-\infty}^{+\infty} H(\omega) e^{-i\omega t} \, d\omega, \tag{2.108b}$$

we get

$$FT(\chi_L') = A \; sgn(t) \; e^{-|\gamma t|}, \tag{2.109}$$

with sgn = -1 for $t < 0$ and sgn = +1 for $t > 0$. In the case of no lifetime broadening, we obtain

$$FT(\chi_L') = A \; sgn(t), \quad \text{for } \gamma = 0. \tag{2.110}$$

The Fourier transform of the Gaussian (Eq. (2.105)) can be written as

$$FT(G) = (a\pi)^{-1/2} e^{-t^2/(4a)}, \tag{2.111}$$

and we can transform $FT(\chi_L')$ $FT(G)$ back and obtain

$$\chi' = A(a\pi)^{-1/2} \int_0^\infty e^{-t^2/(4a)} \sin(\omega t) dt. \tag{2.112}$$

This integral can be related to the error function with a purely imaginary argument [2.24], which in turn can be approximated by a rapidly (n = 25) converging series [2.25]. Therefore we have

$$\chi' = (2A/\pi^{1/2})\, e^{-a\omega^2} \int_0^{a^{0.5}\omega} dt\ e^{t^2}, \text{ or} \tag{2.113}$$

$$\chi' = 2A/\pi e^{-a\omega^2} \left[\frac{a^{0.5}\omega}{2} + \sum_{n=1}^{\infty} \frac{e^{-n^2/4} \sinh(a^{0.5} n\omega)}{n} \right], \tag{2.114}$$

in the limit of pure Doppler broadening. The spectral shapes of the Doppler broadened χ' and χ'' are plotted as dotted curves in Fig. 2.5, in comparison with the pressure broadened χ_L' and χ_L'' (solid curves). Using Eq. (2.105) and Eq. (2.114) we obtain the spectral line shape of the Doppler-broadened FWMRS signal as

$$|\chi^{(3)}|^2 = A^2 e^{-2a\omega^2} \left[\frac{4}{\pi^2} \left(\frac{\omega(a)^{0.5}}{2} + \sum_{n=1}^{\infty} \frac{e^{-n^2/4} \sinh(n\omega(a)^{0.5})}{n} \right)^2 + 1 \right], \tag{2.115}$$

which can be compared to the Doppler-broadened SRS signal

$$\chi'' = A e^{-a\omega^2}. \tag{2.116}$$

As one can see from Fig. 2.6, the purely Doppler-broadened FWMRS signal (solid curve) does not have a Gaussian shape (dotted curve). This is in contrast to SRS and most other spectroscopies, which yield Gaussian line shapes for pure Doppler broadening. In general, a FWMRS line is wider, and it has a different shape than its SRS counterpart.

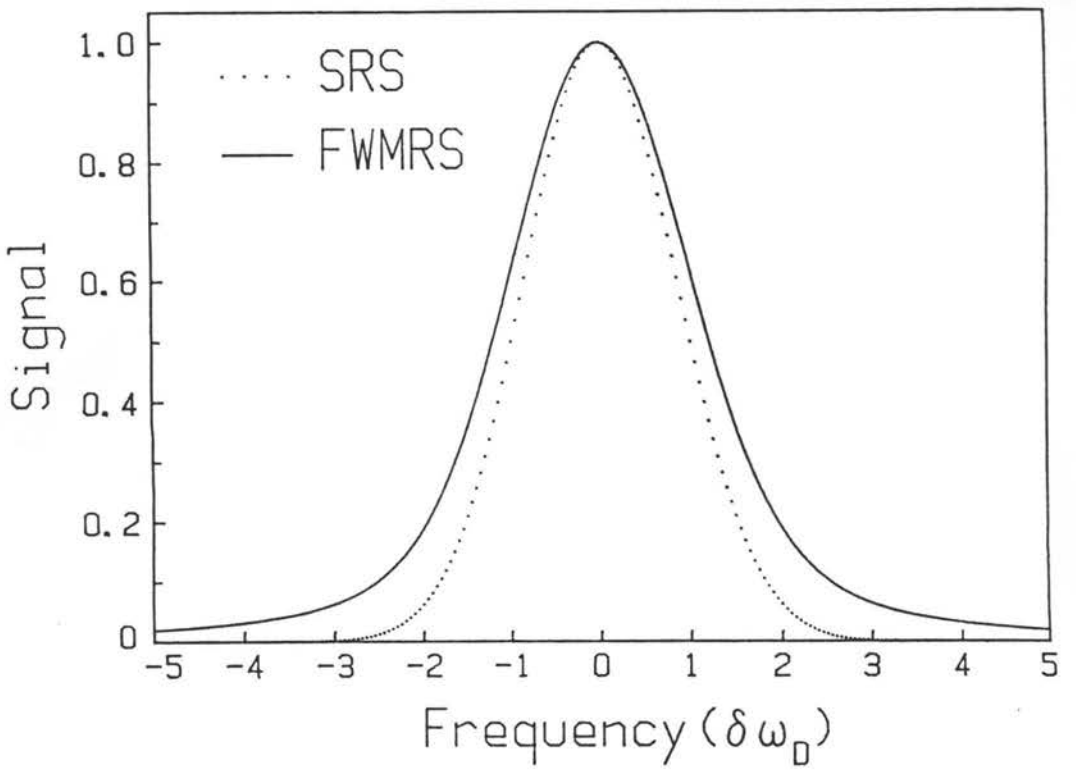

Fig. 2.6. Doppler broadened line shapes of SRS (Gaussian; dotted curve) and FWMRS (non-Gaussian, solid curve)

For pure Doppler broadening the ratio of the HWHM of SRS lines to the HWHM of FWMRS lines is calculated to be 0.827, whereas, in the case of pure pressure broadening, the line shapes and linewidths of SRS and FWMRS are identical. The general case of both Doppler and pressure broadening was investigated by solving the convolution integrals numerically, and we plotted the ratio of SRS to FWMRS linewidth versus the ratio of Doppler width to pressure-broadened width in Fig. 2.7. As one can see in this figure, the ratio of SRS to FWMRS width changes smoothly from the case of pure pressure broadening (1.0) to the case

of pure Doppler broadening (0.827). Physically, the decreasing of this ratio from unity, with the increasing importance of Doppler broadening is the result of interference between different velocity subgroups, which broadens the FWMRS spectrum.

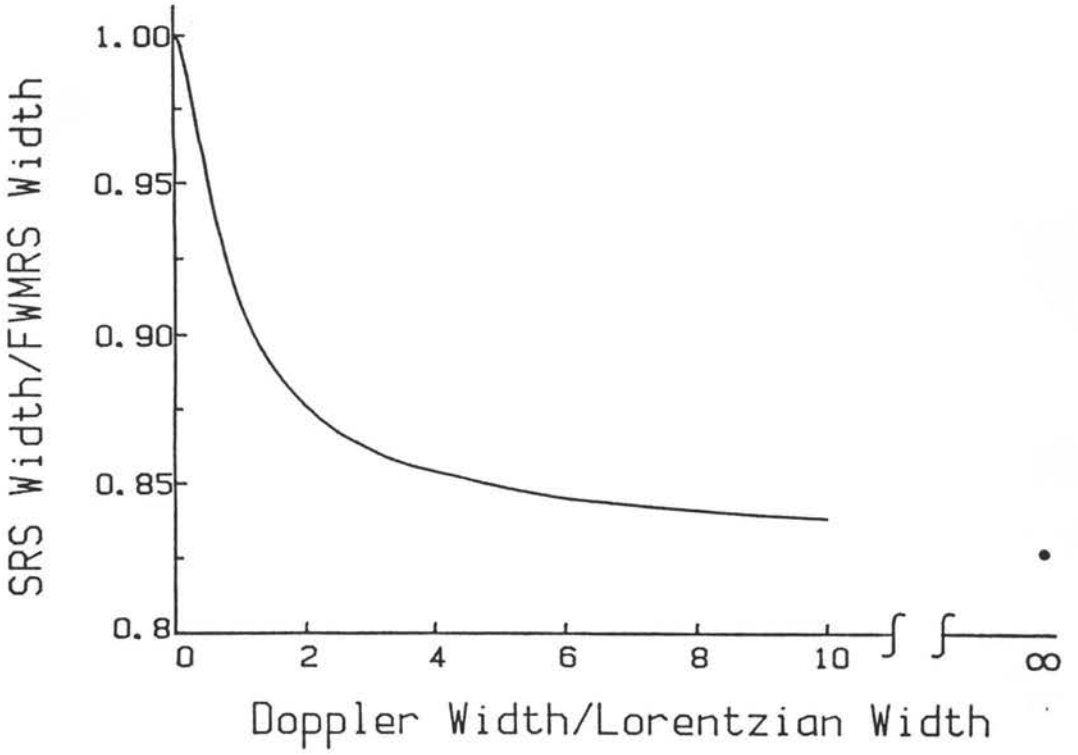

Fig. 2.7. Ratio of the HWHM of a SRS and a FWMRS line, as a function of the ratio of Doppler width and pressure broadened width

2.2.3 Influence of Neighboring Lines

In the case of nonisolated Raman lines, we must sum over the third order nonlinear susceptibilities of all contributing transitions. For the Q-branch molecular vibration of interest, we sum over all

rotational quantum numbers 1. The nonlinear susceptibility $\chi^{(3)}$ can now be written as

$$\chi^{(3)}(\Delta\omega) = \sum_1 \chi_1^{(3)}(\Delta\omega) = \sum_1 \chi_1'(\Delta\omega) + i \sum_1 \chi_1''(\Delta\omega). \qquad (2.117)$$

While the SRS signal is proportional to the straightforward sum of the imaginary components of $\chi^{(3)}$

$$\chi''(\Delta\omega) = \sum_1 \chi_1''(\Delta\omega), \qquad (2.118)$$

the FWMRS signal is proportional to the squared sums

$$|\chi^{(3)}(\Delta\omega)|^2 = \left[\sum_1 \chi_1'(\Delta\omega)\right]^2 + \left[\sum_1 \chi_1''(\Delta\omega)\right]^2, \qquad (2.119)$$

and we have to take the cross terms between the individual χ_1 into account. To gain more understanding for the influence of these terms on the FWMRS line shape, we consider a simplified example. Let us evaluate the shape of a line with a nonlinear susceptibility $\chi_1^{(3)}$, influenced by one neighboring line with susceptibility $\chi_{NR}^{(3)}$, whose center is shifted in frequency by an amount $D\omega$. Using Eq. (2.119) the resulting susceptibility $\chi^{(3)}$ can be written as

$$\chi^{(3)}(\Delta\omega) = \chi_1'(\Delta\omega) + \chi_{NR}'(\Delta\omega+D\omega) + i(\chi_1''(\Delta\omega) + \chi_{NR}''(\Delta\omega+D\omega)). \qquad (2.120)$$

For $D\omega \gg \Delta\omega$ we can approximate $\chi_{NR}^{(3)}$ to be a complex constant over the region of interest and write

$$\chi^{(3)}(\Delta\omega) = \chi_1'(\Delta\omega) + \chi_{NR}'(D\omega) + i(\chi_1''(\Delta\omega) + \chi_{NR}''(D\omega)). \qquad (2.121)$$

Assuming, furthermore, that $D\omega \gg \gamma$, we can neglect χ_{NR}'', which is second order in $D\omega$, while χ_{NR}' is in first order. Therefore we can write $\chi^{(3)}$ in the usual way [2.26]

$$\chi^{(3)} = (\chi_1'+\chi_{NR}') + i\chi_1''. \qquad (2.122)$$

Examining this equation, we see that the SRS spectrum is unchanged, while $|\chi^{(3)}|^2$ can be written as

$$|\chi^{(3)}|^2 = (\chi_1' + \chi_{NR}')^2 + (\chi_1'')^2, \tag{2.123a}$$

$$= \chi_1'^2 + \chi_1''^2 + \chi_{NR}'^2 + 2\chi_1'\chi_{NR}'. \tag{2.123b}$$

Besides the added constant $\chi_{NR}'^2$ we obtain the cross term $2\chi_1'\chi_{NR}'$, which is strongly frequency dependent and makes the FWMRS line shape asymmetric (Fig. (2.8)).

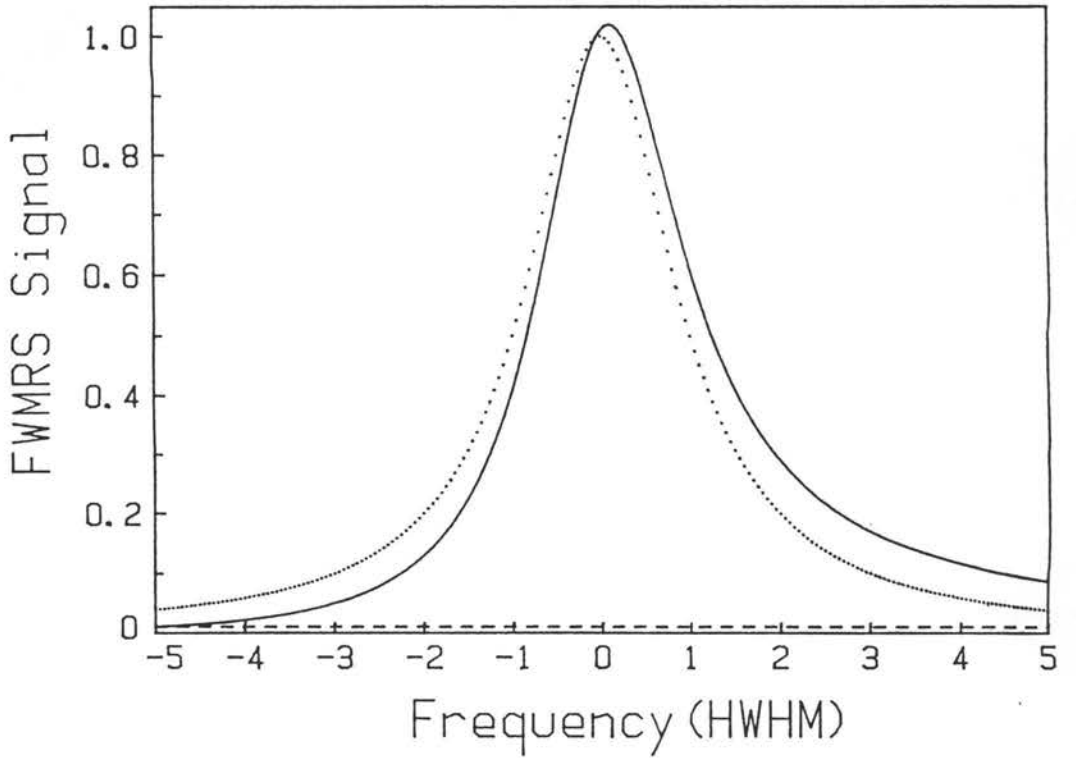

Fig. 2.8. The influence of a non-resonant backround ($\chi_{NR}^2 = 0.01$; dashed curve) on a Lorentzian FWMRS line ($\chi_1'^2+\chi_1''^2$; dotted curve) is shown to result in an asymmetric and shifted line shape ($\chi_1'^2+\chi_1''^2+\chi_{NR}^2+2\chi_1'\chi_{NR}$; solid curve)

This asymmetry leads to a peak shift away from the source (center) of the nonresonant susceptibility χ_{NR}'. The peak positions in FWMRS differ

therefore from those in SRS. As we will show in section 3.2.1, this peak shift is generally different for different lines and can even change its sign (direction) for different rotational lines of the same vibrational branch. To avoid systematic errors in high-resolution FWMRS, one must account for these shifts.

2.2.4 Stark Broadened Spectra

High intensity laser beams, which are associated with strong electrical fields, will shift the energy of each orientational sublevel by a certain amount, as discussed in section 2.1.7. The importance of this effect in coherent Raman spectroscopy has already been recognized by L.A. Rahn et al., who have mainly investigated Stark shifts in spatially homogeneous laser fields [2.27, 2.28]. Most laser spectroscopy is done with more or less Gaussian beams, focused in the medium of interest, which leads to a spatially inhomogeneous intensity distribution in the signal generating region. Additional complications may be due to the use of one or more pulsed laser beams, introducing a time evolution of the intensity.

2.2.4.1 Gaussian Beams

Gaussian beams are an approximate solution of the three dimensional electromagnetic wave equation in an uniform dielectric medium [2.29]. In what follows, we only discuss the cylindrically symmetric, lowest order solution, which corresponds to the TEM_{00} mode. The spatial distribution of the electrical field E(r,z) can be written

in cylindrical coordinates, with z and k being axis and wave vector of propagation, as [2.29]

$$E = E_0\left[1+\left(\frac{z}{z_0}\right)^2\right]^{-0.5} \cdot \exp\left[\frac{-\left(\frac{r}{w_0}\right)^2}{1+\left(\frac{z}{z_0}\right)^2}\right] \exp\left(i\left[\frac{\left(\frac{r}{w_0}\right)^2\left(\frac{z}{z_0}\right)}{1+\left(\frac{z}{z_0}\right)^2} - \tan^{-1}\left(\frac{z}{z_0}\right)\right]\right), \qquad (2.124)$$

where $z_0 = kw_0^2/2$ and w_0 are Rayleigh length and spot radius, respectively. The real terms in Eq. (2.124) describe the Gaussian amplitude variation in the radial direction and its change as the beam propagates (z direction) (Fig. 2.9)).

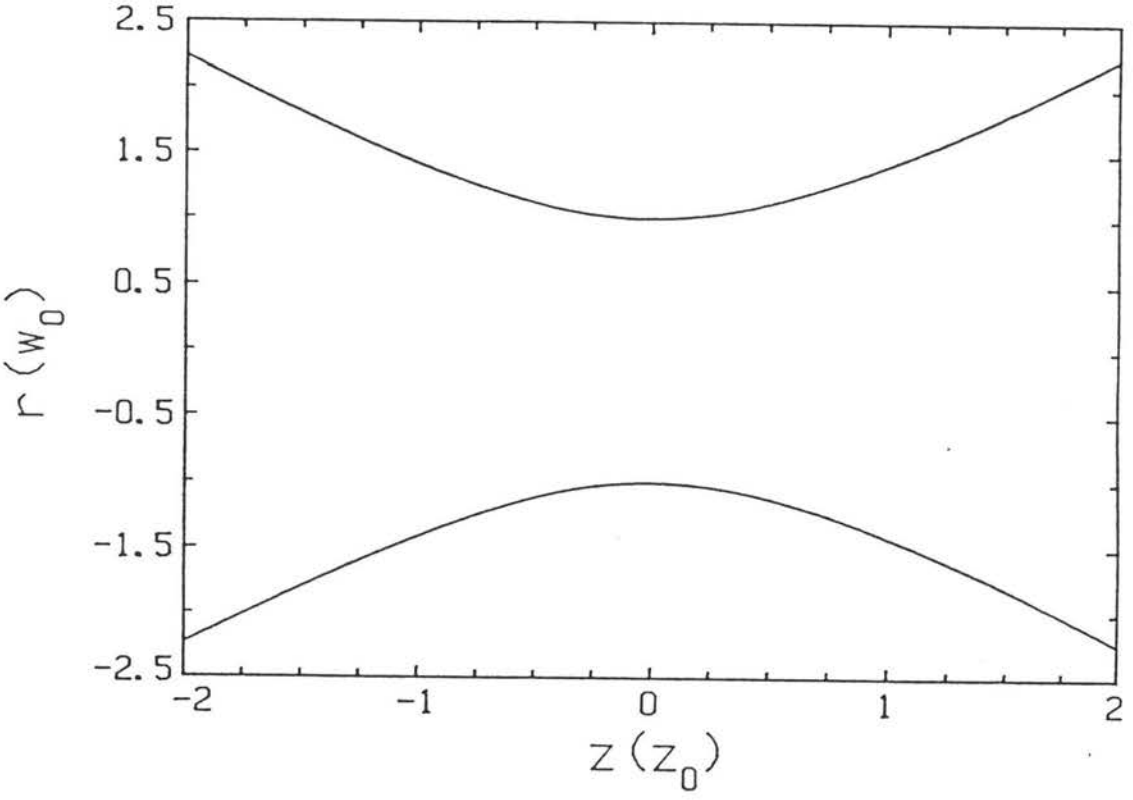

Fig. 2.9. Beam radius w as a function of z

Commonly one defines the beam radius w(z) as

$$w(z) = w_0\left[1 + (z/z_0)^2\right]^{0.5} \qquad (2.125)$$

We note that for any z, the amplitude of the electrical field at r = w has dropped to 1/e of its peak value at r = 0. The values of the beam radii (1/e points) for different z are shown in Fig. 2.9. The complex term in Eq. (2.124) expresses the phase difference between the electrical field of a Gaussian beam and that of a plane wave. A cut (along the z-axis) through surfaces of equal phase difference is shown in Fig. 2.10.

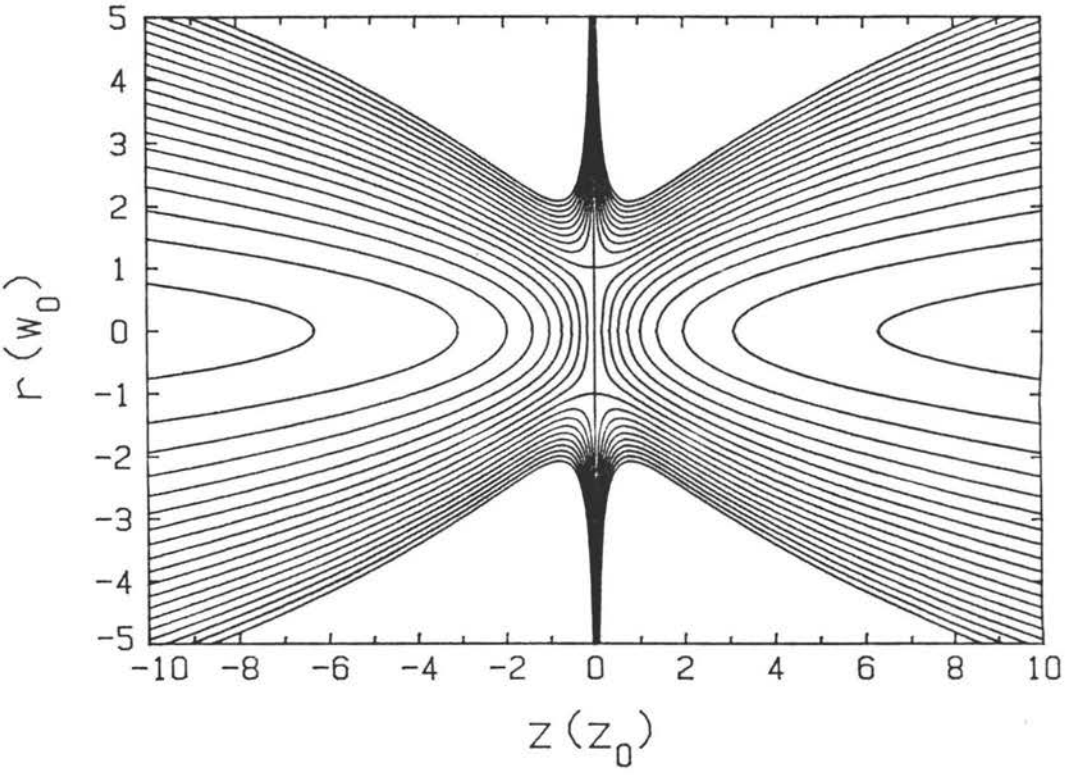

Fig. 2.10. Contours of equal phase difference between a focused Gaussian beam and a plane wave for $\phi = \frac{i}{10}\frac{\pi}{2}$, with i = -9,-8,...,9

We note that one surface of zero phase difference occurs at the obvious $z = 0$, while a second surface is designated by $r^2 = w_0^2 \frac{1 + (z/z_0)^2}{z/z_0} \tan^{-1}(z/z_0)$, with $\lim_{z\to 0} (r) = w_0$. On the axis of beam propagation ($r = 0$) we see the well known phase change of π from $z = -\infty$ to $z = +\infty$.

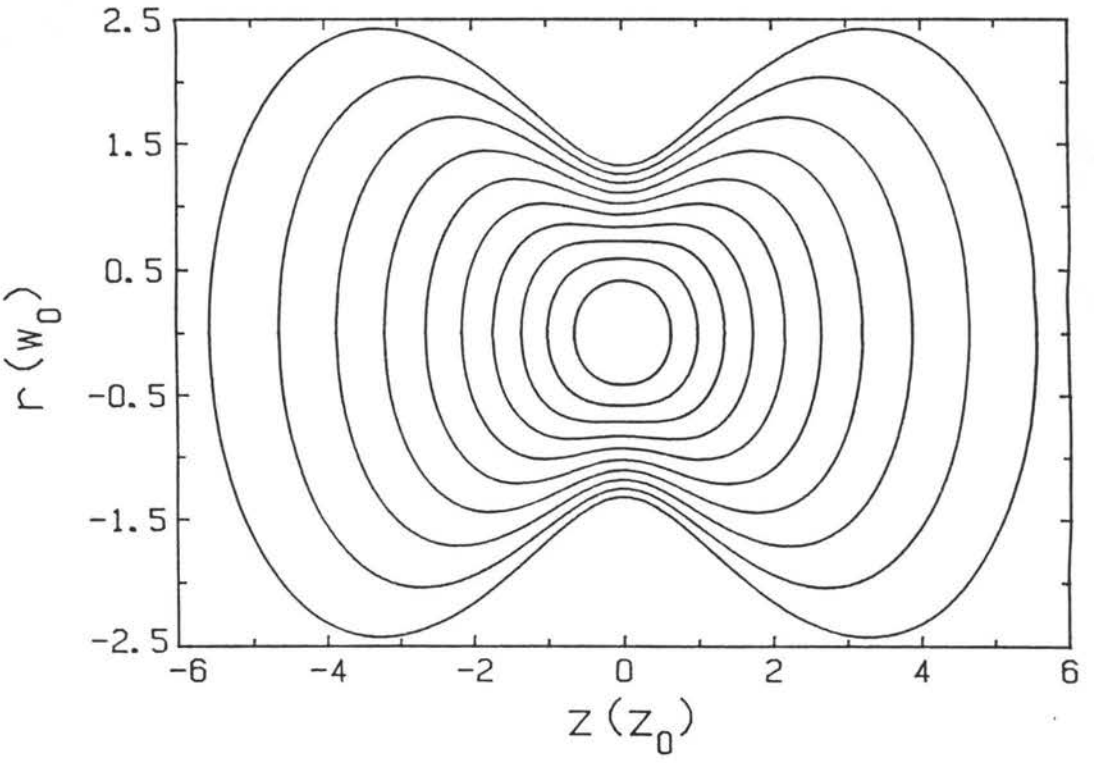

Fig. 2.11. Equal intensity contours for $I = e^{-i/2} I_{max}$ with $i = 1,\ldots,10$

The intensity distribution (Fig. (2.11) corresponding to the field distribution of Eq. (2.124) can be written in terms of the maximum intensity I_0 and the Gaussian intensity distribution $G_I(r,z)$ as

$$I = I_0 G_I(r,z) = I_0 \left[1+\left(\frac{z}{z_0}\right)^2\right]^{-1} \exp\left[\frac{-2\left(\frac{r}{w_0}\right)^2}{1+\left(\frac{z}{z_0}\right)^2}\right], \qquad (2.126a)$$

where the peak intensity I_0 is related to the total power P by

$$P = 2\pi \int_0^\infty dr\ r\ I(r) = \frac{\pi}{2} w_0^2\ I_0. \qquad (2.126b)$$

A cut (along the z-axis) through the equal intensity surfaces of this distribution is plotted in Fig. 2.11 together with the values of the beam radii. We note that the shape of the equal intensity surfaces changes from an "egg" shape to a "dog-bone" shape at $I/I_0 = 1/e$, which might suggest an alternate definition of spot size and beam radius.

2.2.4.2 Signal generation in focused Gaussian Beams

In section 2.2.1 we have treated the SRS and FWMRS signal generation for plane waves. In this section we expand the treatment to focused Gaussian beams. While we consider only parallel polarized laser beams (experimental situation), the calculations for other tensor elements can be done in the same manner as in section 2.2.1. The three dimensional wave equation may be written as

$$\nabla^2 E(t) - \frac{1}{c^2}\frac{\partial^2 E(t)}{\partial t^2} = \frac{1}{\epsilon_0 c^2}\frac{\partial^2 P^{(3)}(t)}{\partial t^2}, \qquad (2.127)$$

with $E(t) = E(\omega_n,r,z)\ e^{i(k_n z - \omega_n t)}$, and

$P^{(3)}(t) = P^{(3)}(\omega_n,r,z)\ e^{i(k_p z - \omega_n t)}$. In cylindrical coordinates the Laplacian operator ∇^2 is given by

$$\nabla^2 = \nabla_t^2 + \frac{\partial^2}{\partial z^2} = \frac{1}{r}\frac{\partial}{\partial r}\left(r\frac{\partial}{\partial r}\right) + \frac{1}{r^2}\frac{\partial^2}{\partial \phi^2} + \frac{\partial^2}{\partial z^2}, \qquad (2.128)$$

where ∇_t^2 stands for its transverse part. Substituting the expressions for E and $P^{(3)}$ into the wave equation, and using the slowly varying amplitude approximation (Eq. (2.92)) we obtain

$$\nabla_t^2 E(\omega_n,r,z) + 2ik_n \frac{\partial E(\omega_n,r,z)}{\partial z} = -\frac{1}{\epsilon_0} k_n^2 P^{(3)}(\omega_n,r,z)\, e^{i(k_p-k_n)z}. \quad (2.129)$$

First we deal with n = 1,2, corresponding to SRGS (stimulated Raman gain spectroscopy) and IRS (inverse Raman spectroscopy), respectively. The polarizations given by Eq.'s (2.84b), (2.84c) yield $k_p = k_n$ and we write for n = 1 (SRGS) in somewhat simpler notation

$$\nabla_t^2 E_1 + 2ik_1 \frac{\partial E_1}{\partial z} = -k_1^2 \chi^{(3)*} E_1 |E_2|^2. \quad (2.130a)$$

Multiplying this equation with E_1^* and its complex conjugate with E_1 yields

$$E_1^* \left(\nabla_t^2 + 2ik_1 \frac{\partial}{\partial z} \right) E_1 = - k_1^2 \chi^{(3)*} |E_1|^2 |E_2|^2. \quad (2.130b)$$

$$E_1 \left(\nabla_t^2 - 2ik_1 \frac{\partial}{\partial z} \right) E_1^* = -k_1^2 \chi^{(3)} |E_1|^2 |E_2|^2. \quad (2.130c)$$

We subtract Eq. (2.130c) from Eq. (2.130b), integrate the result over the transverse area, $\int_0^{2\pi} d\phi \int_0^{\infty} r dr$, and obtain

$$\int_0^{2\pi} d\phi \int_0^{\infty} dr\, r \frac{\partial}{\partial z} |E_1|^2 = k_1 \int_0^{2\pi} d\phi \int_0^{\infty} dr\, r\, \chi'' |E_1|^2 |E_2|^2, \quad (2.131a)$$

where we have made use of $\int_0^{2\pi} d\phi \int_0^{\infty} dr\, r \left(E_1^* \nabla_t^2 E_1 - E_1 \nabla_t^2 E_1^* \right) = 0$, which is a result of Green's theorem and the fact that, for Gaussian beams, $|E|^2$ vanishes for $r \to \infty$ much faster than 1/r. With the help of Eq. (2.32b) we can rewrite Eq. (2.131a) in terms of intensities as

$$\frac{1}{2}\, c\epsilon_0 \int_0^{2\pi} d\phi \int_0^{\infty} dr\; r \frac{\partial}{\partial z} I_1 = k_1 \int_0^{2\pi} d\phi \int_0^{\infty} dr\; r\; \chi'' I_1 I_2, \qquad (2.131b)$$

For Gaussian beams we take advantage of their cylindrical symmetry and, for small gain and no pump depletion, we can write the total power of the SRGS signal as

$$\Delta P_1 = 2\pi \int_0^{\infty} dr\; r I_1 = 4\pi \frac{k_1}{c\;\epsilon_0} \int_{z_1}^{z_2} dz \int_0^{\infty} dr\; r\; \chi'' I_1 I_2, \qquad (2.132a)$$

where z_1 and z_2 mark the beginning and the end of the interaction region (position of cell windows), and χ'' stands for the imaginary part of the third order nonlinear susceptibility $\chi^{(3)}$ (Eq. (2.104)). The equivalent equation for n = 2 (IRS) is

$$\Delta P_2 = 2\pi \int_0^{\infty} dr\; r I_2 = -4\pi \frac{k_2}{c\;\epsilon_0} \int_{z_1}^{z_2} dz \int_0^{\infty} dr\; r\; \chi'' I_1 I_2, \qquad (2.132b)$$

For a uniform medium and no Stark effect, χ'' is independent of the spatial coordinates r, z and we can solve Eq.'s (2.132). Using the expressions (2.126) for the intensities, we write the power of the generated signal as

$$\Delta P_1 = \frac{k_1 k\, \chi''}{c\;\epsilon_0 \pi} P_1\, P_2 \tan^{-1}(z/z_0)\Big|_{z_1}^{z_2} \qquad \text{(for SRGS)}, \qquad (2.133a)$$

$$\Delta P_2 = -\frac{k_2 k\, \chi''}{c\;\epsilon_0 \pi} P_1\, P_2 \tan^{-1}(z/z_0)\Big|_{z_1}^{z_2} \qquad \text{(for IRS)}, \qquad (2.133b)$$

where we have assumed identical Gaussian beam parameters for both beams. This is a good approximation for $k_1 \approx k_2$, i.e. small Raman shifts. The variable k corresponds to the common beam parameters ($k = 2z_0/w_0^2$) and may be chosen somewhere in between k_1 and k_2. For $z_1 \to -\infty$ and $z_2 \to \infty$, the total generated power becomes

$$\Delta P_1 = \frac{k_1 k \chi''}{c \epsilon_0} P_1 P_2 \qquad \text{(for SRGS)}, \tag{2.134a}$$

$$\Delta P_2 = -\frac{k_2 k \chi''}{c \epsilon_0} P_1 P_2 \qquad \text{(for IRS)}. \tag{2.134b}$$

If pulsed lasers are used, P_1 and/or P_2 become a function of time. In the case of non-time resolved detection, we integrate the whole expression over time to obtain the total signal energy. With the approximation $k = k_1 = k_2$, we define a gain coefficient G as

$$G = \frac{k^2 \chi''}{c \epsilon_0} P_{pump} \tag{2.134c}$$

and rewrite Eq.'s (2.134a,b) as

$$\Delta P_1 = G P_1 \qquad \text{(for SRGS)}, \tag{2.134d}$$

$$\Delta P_2 = -G P_2 \qquad \text{(for IRS)}. \tag{2.134e}$$

Under the conditions used to derive Eq.'s (2.134) (large cell, homogeneous medium, no Stark effect) the SRS signals are obviously independent of the focal parameters.

For high laser intensities we have to take the Stark effect into account; $\chi^{(3)}$ becomes a function of the pump laser intensity (which may be a function of time) and therefore a function of the spatial coordinates r and z. We rewrite Eq.'s (2.132) for these conditions as

$$\Delta P_1 = \frac{16}{\pi w_0^4} \frac{k_1}{c \epsilon_0} P_1 P_2 \int_{z_1}^{z_2} dz \int_0^\infty dr\, r\, \chi''(P_2,r,z)\, G_I^2, \tag{2.135a}$$

$$\Delta P_2 = -\frac{16}{\pi w_0^4} \frac{k_2}{c \epsilon_0} P_1 P_2 \int_{z_1}^{z_2} dz \int_0^\infty dr\, r\, \chi''(P_1,r,z)\, G_I^2, \tag{2.135b}$$

where we have assumed that the pump laser intensity is far higher than the probe laser intensity and is the sole cause of the Stark effect. The frequency dependency of the Lorentzian part of χ'' is given by

Eq.'s (2.104b), (2.66), (2.124) and (2.126b) for a single transition as

$$\chi_L'' = B \frac{\gamma}{(\Delta\omega + \beta I)^2 + \gamma^2}, \tag{2.136}$$

where $I = I_0 G_I = \frac{2P}{\pi w_0^2} G_I$. In the case of multiple transitions generating signal at the same frequency, one simply sums over the individual contributions. For additional broadening such as Doppler broadening or the influence of a finite laser linewidth, χ_L'' has to be convoluted with the respective lineshapes, as demonstrated in section 2.2.2. Due to the complicated functional dependence of χ'', we have to evaluate the integrals in Eq.'s (2.135) numerically. This will be done, for our experimental parameters, in section 3.2.2.

Now we proceed to the polarizations at the frequencies $\omega_3=2\omega_1-\omega_2$ and $\omega_4=2\omega_2-\omega_1$, which correspond to CSRS (coherent Stokes Raman spectroscopy) and CARS (coherent anti-Stokes Raman spectroscopy), respectively. For these polarizations we write Eq. (2.129) as

$$\left(\nabla_t^2 + 2ik_n \frac{\partial}{\partial z}\right) E_n(r,z) = f_n(r,z) \tag{2.137a}$$

where ∇_t^2 stands for the transverse Laplacian (Eq. (2.128)) and $f_n(r,z)$ is defined as

$$f_n(r,z) = -\frac{k_n^2}{\epsilon_0} P^{(3)}(\omega_n,r,z)\, e^{i(k_p-k_n)z}. \tag{2.137b}$$

A Fourier transform (Eq. (2.108)) of the transverse coordinates (x, y or $\vec{r}$) transforms Eq. (2.137a) into transverse wave vector, k_t-space as

$$\left(-k_t^2 + 2ik_n \frac{\partial}{\partial z}\right) E_n(k_t,z) = \frac{1}{\pi^2} \int d\vec{r}\, e^{-i\vec{k}_t\cdot\vec{r}} f_n(r,z). \tag{2.138}$$

Using the relationship

$$2ik_n \frac{\partial}{\partial z}\left[E \exp\left(i\frac{k_t^2 z}{2k_n}\right)\right] = -k_t^2 E \exp\left(i\frac{k_t^2 z}{2k_n}\right) + 2ik_n \frac{\partial E}{\partial z}\exp\left(i\frac{k_t^2 z}{2k_n}\right), \quad (2.139a)$$

we rewrite Eq. (2.138) as

$$2ik_n \frac{\partial}{\partial z}\left[E_n(k_t,z) \exp\left(i\frac{k_t^2 z}{2k_n}\right)\right] = \frac{1}{\pi^2}\exp\left(i\frac{k_t^2 z}{2k_n}\right) \int d\vec{r}\, e^{-i\vec{k}_t\cdot\vec{r}} f_n(r,z), \quad (2.139b)$$

which becomes after integration over z

$$E_n(k_t,z_{1,2}) = \frac{-i}{2\pi^2 k_n}\exp\left(-i\frac{k_t^2 z}{2k_n}\right) \int_{z_1}^{z_2} dz \exp\left(i\frac{k_t^2 z}{2k_n}\right)\int d\vec{r}\, e^{-i\vec{k}_t\cdot\vec{r}} f_n(r,z), \quad (2.139c)$$

where z_1 and z_2 correspond to the limits of the interaction region (position of cell windows). With the help of Parseval's theorem

$$\int_{-\infty}^{+\infty} d\vec{x}\,|E(\vec{x})|^2 = \frac{\pi}{2}\int_{-\infty}^{+\infty} d\vec{k}\,|E(\vec{k})|^2, \quad (2.140a)$$

and Eq. (2.32b) we can write the power generated at the frequency ω_n as

$$P_n = \frac{c\,\epsilon_0}{2}\int d\vec{r}\,|E(\vec{r},z_M)|^2 = \frac{c\,\epsilon_0 \pi^2}{8}\int d\vec{k}_t\,|E(k_t,z_M)|^2 \quad (2.140b)$$

and

$$P_n = \frac{c\,\epsilon_0}{32\pi^2 k_n^2}\int d\vec{k}_t \left| \int_{z_1}^{z_2} dz \exp\left(i\frac{k_t^2 z}{2k_n}\right)\int d\vec{r}\, e^{-i\vec{k}_t\cdot\vec{r}} f_n(r,z)\right|^2. \quad (2.140c)$$

For a cylindrical symmetric $f_n(r,z)$ we use the identities

$$\int d\vec{k}_t\, g(|k_t|,z) = 2\pi\int_0^\infty dk_t\; k_t\, g(|k_t|,z), \quad (2.141a)$$

$$\int d\vec{r}\, e^{-i\vec{k}_t\cdot\vec{r}} f_n(r,z) = 2\pi\int_0^\infty dr\; r\, f_n(r,z)\, J_0(k_t r), \quad (2.141b)$$

where $J_0(k_t r)$ stands for the Bessel function

$$J_0(k_t r) = \frac{1}{2\pi}\int_0^{2\pi} d\phi\ e^{-ik_t r\cos\phi}, \qquad (2.141c)$$

to rewrite the power of the generated signal as

$$P_n = \frac{c\,\pi\,k_n^2}{4\,\epsilon_0}\int_0^{\infty} dk_t\ k_t \left|\int_{z_1}^{z_2} dz\ \exp\left(i\frac{k_t^2 z}{2k_n}\right)\int_0^{\infty} dr\ r\ J_0(k_t r)\ P^{(3)}(\omega_n, r, z)\right|^2, \qquad (2.142)$$

where we have assumed phase matching, i.e. $k_n = k_p$. We use the explicit expressions for the third order nonlinear polarizations (Eq. (2.84d,e)) and the electrical field in a Gaussian beam (Eq. (2.124)) to write the final expressions for the CSRS (n=3) and CARS (n=4) signal as

$$P_3 = \frac{2k_3^2 k^2}{\pi^2 c^2 \epsilon_0^2} P_1^2 P_2 \int_0^{\infty} dx \left|\int_{z_1}^{z_2} dz\ e^{i\frac{xz}{4}}\ \frac{e^{-i\tan^{-1}z}}{(1+z^2)^{3/2}}\int_0^{\infty} dr\ r\chi^* J_0(x^{\frac{1}{2}} r) e^{r^2\left(\frac{iz-3}{1+z^2}\right)}\right|^2, \qquad (2.143a)$$

$$P_4 = \frac{2k_4^2 k^2}{\pi^2 c^2 \epsilon_0^2} P_1 P_2^2 \int_0^{\infty} dx \left|\int_{z_1}^{z_2} dz\ e^{i\frac{xz}{4}}\ \frac{e^{-i\tan^{-1}z}}{(1+z^2)^{3/2}}\int_0^{\infty} dr\ r\chi J_0(x^{\frac{1}{2}} r) e^{r^2\left(\frac{iz-3}{1+z^2}\right)}\right|^2, \qquad (2.143b)$$

where $x = \frac{2 z_0}{k_n} k_t^2$, and r, z are written in units of spot radius w_0 and Rayleigh length z_0, respectively. If pulsed lasers are used, P_1 and/or P_2 become a function of time. In the case of non-time resolved detection, we integrate the whole expression over time to obtain the total signal energy.

For a uniform medium and no Stark effect, χ is independent of the spatial coordinates r, z and we may solve Eq.'s (2.143) numerically. To simplify the computation we have solved the innermost integral analytically. For a z-integration over symmetric limits

$(z_M = z_2 = -z_1)$ and n = 3, 4 we obtain

$$P_n = \frac{2}{\pi^2} f(z_M)\, G^2 P_{probe} \tag{2.144a}$$

where $f(z_M)$ is defined as

$$f(z_M) = \int_0^{\infty} dx \left[\int_0^{z_M} dz \frac{\exp\frac{-3x(1+z^2)}{4(9+z^2)}}{(1+z^2)(9+z^2)} \left[(3+z^2)\cos\left(\frac{2xz}{9+z^2}\right) + 2z \sin\left(\frac{2xz}{9+z^2}\right) \right] \right]^2, \tag{2.144b}$$

with $f(z_M \to \infty) = 1.21$, (2.144c)

and G is defined as

$$G = \frac{k^2 |\chi|}{c\, \epsilon_0} P_{pump}, \tag{2.144d}$$

under the approximation of $k = k_1 = k_2$. This definition of the gain coefficient G agrees for the line center ($\chi' = 0$, $|\chi| = \chi''$) with the definition of G for SRGS (Eq. (2.134c)) and we can compare SRGS and FWMRS signal power directly. Figure 2.12 shows the power of SRS and FWMRS signals generated in a cell with windows at $-z_M$ and z_M, calculated with Eq. (2.133) and Eq. (2.144), respectively. The x-axis is in units of the Rayleigh length and the power $P(z_M)$ is normalized with respect to the power generated in a cell of infinite length, $P(\infty)$. We note that the SRS signal is generated within a shorter interaction length than the FWMRS signal. The strength of the FWMRS signal for Gaussian beams has been discussed by many authors and various approximate solutions have been given. We know of only one exact numerical solution, which was given by Bjorklund, who solves the problem in k-space [2.30]. His numerical result for the total signal agrees with ours, but he fails to take a possible spatial dependence

of $\chi^{(3)}$ into account, which makes the inclusion of the optical Stark effect unclear.

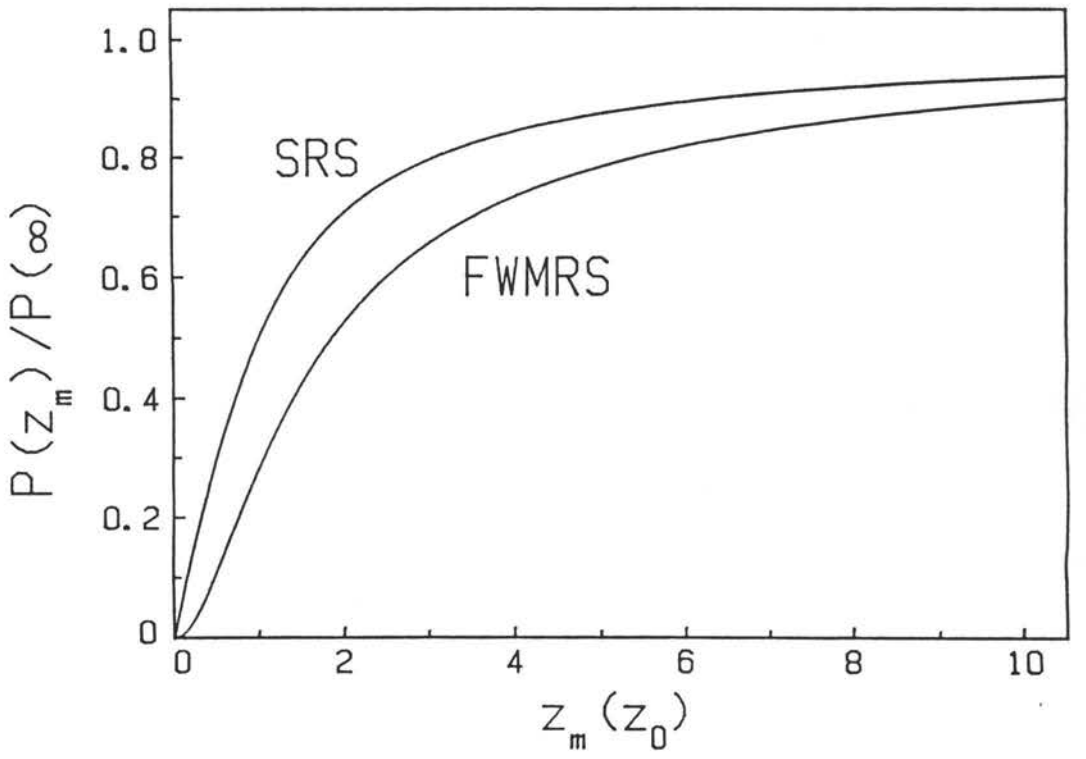

Fig. 2.12. Relative power generated between $z = -z_m$ and $z = z_m$

In the case of high laser intensities we proceed exactly the same way as for SRS. Due to the Stark effect we must write $\chi^{(3)}$ as a function of local intensity and therefore as a function of P_{pump} (which may be a function of time), r and z. For a single Lorentzian transition we have

$$\chi_L^{(3)} = \frac{B}{(\Delta\omega+\beta I)-i\gamma}, \qquad (2.145)$$

where $I = I_0 G_I = \frac{2P\ GI}{\pi\ w_0^2}$. Explicit FWMRS spectra will be calculated in section 3.2.2, by solving the three dimensional integrals in Eq. (2.143) for our experimental parameters.

References Chapter 2

2.1 G. Herzberg, Molecular Spectra and Molecular Structure I, Spectra of Diatomic Molecules (Van Nostrand, New York, 1950).

2.2 G. Placzek, "Rayleigh Streuung und Raman Effekt", in: E. Marx, Handbuch der Radiologie (Akademische Verlagsgesellschaft, Leipzig, 1934) Bd. VI, Teil II, S. 205.

2.3 L. Rahn, Sandia National Laboratory, Livermore, California (personal communication, 1984).

2.4 R.P. Feynman, The Feynman Lectures on Physics III, Quantum Mechanics (Addison-Wesley, Reading, Massachusetts, 1970), p. 4-1.

2.5 E. Merzbacher, Quantum Mechanics (Wiley, New York, 1970), p. 186.

2.6 G. Placzek and E. Teller, "Die Rotationsstruktur der Ramanbanden Mehratomiger Moleküle," Z. Physik **83**, 209 (1933).

2.7 J.D. Jackson, Classical Electrodynamics (Wiley, New York, 1975), p. 396.

2.8 M. Born, Optik (Springer Verlag, Berlin, 1933), S. 401.

2.9 G. Arfken, Mathematical Methods for Physicists (Academic, New York, 1970), p. 177.

2.10 E. Merzbacher, Quantum Mechanics (Wiley, New York, 1970), p. 64.

2.11 S.R. Langhoff, C.W. Bauschlicher, Jr. and D.P. Chong, "Theoretical Study of the Effects of Vibrational-Rotational Interactions on the Raman Spectrum of N_2," J. Chem. Phys. **78**, 5287 (1983).

2.12 W.M. Huo, NASA Ames Research Center, MS 230-3, Moffett Field, Ca 94035, "Optical Stark Effect in the Ro-Vibrational Raman Spectrum of a Diatomic Molecule in the $^1\Sigma^+$ State and Numerical Calculations on N_2," (unpublished, 1984).

2.13 E. Merzbacher, Quantum Mechanics (Wiley, New York, 1970), p. 396.

2.14 E.U. Condon and G.H. Shortley, The Theory of Atomic Spectra, (University Press, Cambridge, 1964), p. 77.

2.15 R. Gaufres and S.Sportouch, "The Placzek-Teller Coefficients $b_{J,K}$, for Negative ΔJ," J. Molec. Spect. **39**, 527 (1971).

2.16 G.C. Herring, "Coherent Raman Spectroscopy for Supersonic Flow Measurements," Ph.D. Dissertation (Colorado State University, Fort Collins, Colorado, 1987).

2.17 N. Bloembergen, Nonlinear Optics, (Benjamin, New York, 1965).

2.18 Y.R. Shen, The Principles of Nonlinear Optics, (Wiley, New York, 1984), p. 28.

2.19 R.W. Hellwarth, "Third-Order Optical Susceptibilities of Liquids and Solids," Prog. Quant. Electr. **5**, 1 (1977).

2.20 A. Owyoung, "Coherent Raman Gain Spectroscopy Using CW Laser Sources," IEEE J. Quantum Electron. **QE-14**, 192 (1978).

2.21 G.J. Rosasco, W.S. Hurst and W. Lempert, " Three-Beam Phase-Modulation Technique for Coherent Raman Spectroscopy," Opt. Lett. **9**, 19 (1984).

2.22 G.J. Rosasco and W.S. Hurst, "Measurement of Resonant and Nonresonant Third-order Nonlinear Susceptibilities by Coherent Raman Spectroscopy," Phys. Rev. A **32**, 281 (1985).
2.23 Y. Prior, "Three-Dimensional Phase Matching in Four-Wave Mixing," Appl. Opt. **19**, 1741 (1980).
2.24 National Bureau of Standards, Handbook of Mathematical Functions, edited by M. Abramowitz and I.A. Stegun, Applied Mathematics Series 55, (U.S. Government Printing Office, Washington, D.C., 1964), Eq. 7.4.7, p.302.
2.25 H.E. Salzer, "Formulas for Calculating the Error Function of a Complex Variable," Math. Tables Aid Com. **5**, 67 (1951).
2.26 W.M. Tolles, J.W. Nibler, J.R. McDonald, and A.B. Harvey, "A Review of the Theory and Application of Coherent Anti-Stokes Raman Spectroscopy (CARS)," Appl. Spectrosc. **31**, 253 (1977).
2.27 L.A. Rahn, R.L. Farrow, M.L. Koszykowski and P.L. Mattern, "Observation of an Optical Stark Effect on Vibrational and Rotational Transitions," Phys. Rev. Lett. **45**, 620 (1980).
2.28 R.L. Farrow and L.A. Rahn, "Optical Stark Splitting of Rotational Raman Transitions," Phys. Rev. Lett. **48**, 395 (1982).
2.29 J.T. Verdeyen, Laser Electronics, (Prentice-Hall, Englewood Cliffs, New Jersey, 1981), p. 56.
2.30 G.C. Bjorklund, "Effects of Focusing on Third-Order Nonlinear Processes in Isotropic Media," IEEE J. Quantum Electron. **QE-11**, 287 (1975).

Chapter 3

Experiments

3.1 Experimental Setup

We use an experimental setup (Fig. 3.1) which has evolved from a prior arrangement, designed by G.C. Herring for supersonic flow measurements with coherent Raman spectroscopy [3.1, 3.2, 3.3].

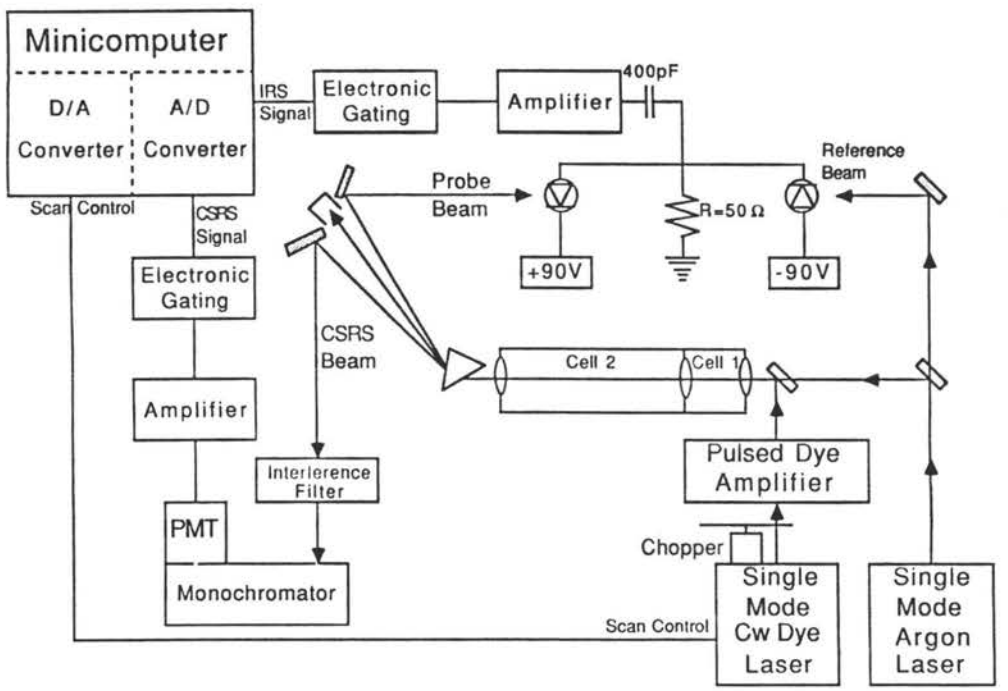

Fig. 3.1. Experimental setup

Major changes include a detection system for the simultaneous detection of IRS and CSRS signal, a nitrogen cell for convenient change between tight and mild focusing, a setup for measuring the beam profile and a computerized data aquisition and laser scan system.

3.1.1 Overview

To perform CRS we use two lasers. The pulsed laser beam is generated by passing the output of a 70-mW single-mode tunable cw dye laser through a pulsed amplifier. This way we obtain 5-nsec pulses with a nearly Fourier-transform-limited linewidth of 116MHz. The peak power is 2-4MW at roughly 584.5nm, and the repetition rate is 10 pulses/sec. For the second (probe) laser we use a 514.5-nm cw single-mode Ar^+-ion laser with roughly 200-mW output power and a line width of several megahertz. The fluorescence of a temperature-stabilized I_2 cell is used to lock the frequency of the Ar^+-ion laser to the side of an I_2 line.

While SRGS and IRS signals, for lasers with given power, are equally large in terms of photon numbers, the relative gain/loss depends on the power of the respective laser beams. With the pulsed dye laser being some 7 orders of magnitude more powerful than the cw argon laser, the relative gain in SRGS is roughly 7 orders of magnitude weaker than the relative loss in IRS. The situation for FWMRS is similarly asymmetric. While the CARS signal is proportional to $P_{dye}\ P^2_{argon}$, the CSRS signal is proportional to $P^2_{dye}\ P_{argon}$ and therefore some 7 orders of magnitude stronger. Thus we chose to detect the IRS and CSRS signals.

We overlap the dye laser beam and the argon laser beam with a dichroic mirror and focus them with 5-cm focal length into the first cell. This focus is imaged with 50-cm focal length into the second cell, resulting in a roughly ten times larger spot size, corresponding to a roughly 100 times lower intensity (Fig. (3.1)). During the experiment, one of these cells is filled with nitrogen at a pressure of 10kPa and a temperature of 292K, while the other cell is evacuated. By evacuating one cell and filling the other, we can switch within less than a minute from Raman signals generated in a tight focusing arrangement to signals generated in a mild focusing arrangement, without any realignment of optical components. After passing through the cells, the beams are separated by a prism and the dye laser beam is blocked by a beam dump. We detect the CSRS beam with a photomultiplier, while the argon laser beam is detected by a fast photodiode. Using the argon laser line at 514.5nm, we tune the dye laser near 584.5nm to be in resonance with the Q branch $v=0 \rightarrow v=1$ vibrational transition in molecular nitrogen (2330-cm^{-1} Raman shift). We scan the dye laser digitally over the Raman resonances, with eight dye laser pulses per frequency step. IRS and CSRS signals are electronically gated and then simultaneously recorded on a shot-to-shot basis by a minicomputer. To check for scan nonlinearities and absolute frequency of the dye laser, we split off a part of the cw dye beam before amplification and record, simultaneously with the Raman spectra, a saturated absorption spectrum of I_2 and a transmission spectrum of a Fabry-Perot interferometer with a free spectral range of about 75MHz.

3.1.2 Pump Laser System

We obtain high peak power, narrow band, tunable laser light by amplifying the output of a commercial cw dye laser with a home built three stage amplifier. The cw dye laser is a Coherent model 599-21, which is actively stabilized to an external reference cavity yielding a linewidth of 1MHz. It is pumped by 2.5W of multiline argon ion laser radiation. We use rhodamine 6G (rhodamine 590) as a dye to obtain between 50 and 120mW output power at a wavelength of about 584.5nm. While most of the output power is used as input for the pulsed amplifier, roughly 10% are split off for diagnostic purposes (Fig. (3.2)).

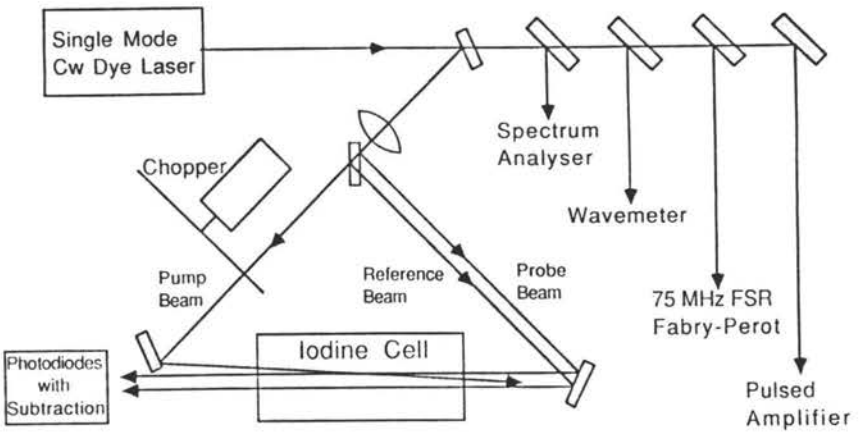

Fig. 3.2. Cw dye laser and diagnostic system

The diagnostic setup includes a Kowalski-type wavemeter [3.4], which measures the wavelength to one part in 10^6, a scanning confocal Fabry-Perot interferometer (spectrum analyser) with a free spectral range of 1.5GHz to verify single mode operation, a temperature stabilized

(±0.001K) confocal Fabry-Perot interferometer with a free spectral range of 74.295 ± 0.0003MHz [3.5] to check scan linearity and an I_2 saturated absorption setup as absolute frequency reference.

Saturated absorption spectroscopy (Fig. (3.2)) is a fairly simple technique used to eliminate first order Doppler broadening from the spectra of gaseous systems [3.6]. The dye laser beam is split into a strong pump beam and a weak probe beam. These beams are crossed in the sample in a nearly counter propagating geometry. Molecules which have a non zero velocity component parallel to the beam direction see both beams at different frequencies. Therefore only molecules with zero velocity component in beam direction can interact with both beams simultaneously. When the dye laser frequency corresponds to a molecular resonance frequency in the laboratory frame, the pump beam will bleach the absorption, resulting in a Doppler free absorption signal from the probe beam. To increase the signal to noise ratio the pump beam is chopped at a couple of kilohertz and we use phase sensitive detection for the probe beam. Additionally we employ a reference probe beam to reduce the influence of dye laser intensity fluctuations and Doppler broadened absorption signals. Using saturated absorption spectroscopy we obtain the Doppler free iodine hyperfine spectrum, which consists of a multitude of lines, with individual linewidths of several megahertz. These lines are used as frequency markers, which enable us to obtain a common frequency scale for repeated dye laser scans.

We amplify the narrow band, well characterized output of the cw dye laser with a three stage pulsed dye amplifier (Fig. (3.3)), which

is based on a design previously reported in the literature [3.7].

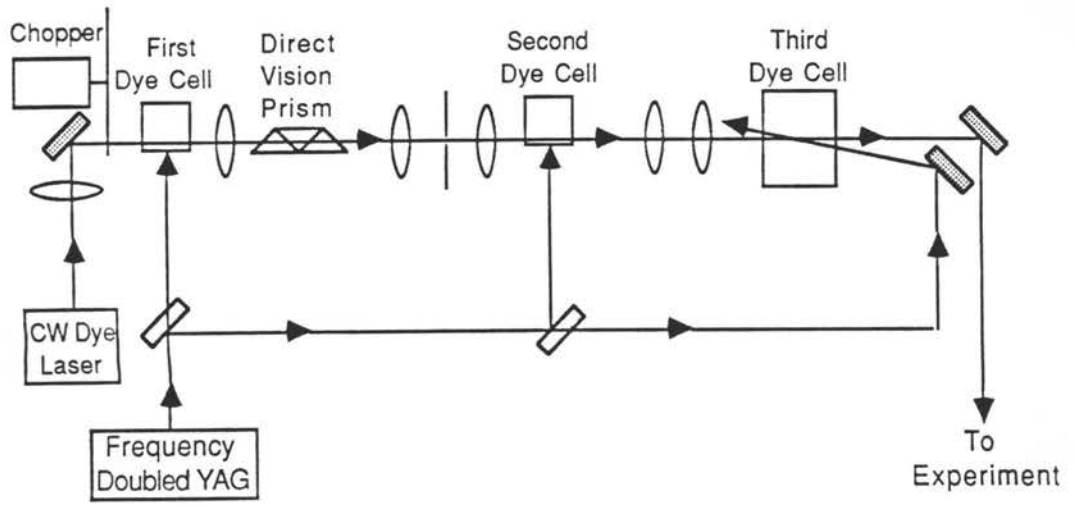

Fig. 3.3. Schematic of the dye laser amplifier

Recently a similar amplifier has become commercially available from Spectra Physics. For the amplification of 584.5nm radiation we use either rhodamine B (rhodamine 610) or sulfo-rhodamine 590 (kiton red 620) in methanol as a gain medium. The Nd-Yag laser (Quanta-Ray model DCR-1A) used to pump the amplifier is a frequency doubled oscillator-amplifier configuration, which emits 5-7nsec pulses at 532nm with 10Hz repetition rate. It is used at 50-70mJ pulse energy, well below its maximum power. Before the cw dye laser beam enters the first amplifier stage it is chopped into 1ms pulses with 10Hz repetition rate. This reduces unnecessary thermal heating of the dye between Nd-Yag laser pulses. The Nd-Yag laser is then triggered by the chopper and all of the detection electronics is triggered by the Q-switch synchronization output of the Nd-Yag laser. The dye laser beam is focused in both the

first and second amplifier stage, which are transversely pumped by about 5 and 15% of the total Nd-Yag output, respectively (Fig. (3.3)). To reduce amplification of spontaneous flourescence from the first stage, a direct vision prism together with a pinhole provides spectral and spatial filtering behind the first stage. An astronomical telescope is used to expand and collimate the output of the second stage to about 3mm diameter. The rest of the Nd-Yag laser output is used to longitudinally pump the third stage resulting in a dye laser pulse energy of 10-20mJ, corresponding to a power of about 2-4MW for 5nsec pulses. The spectral lineshape is shown in Fig. (3.4) [3.3].

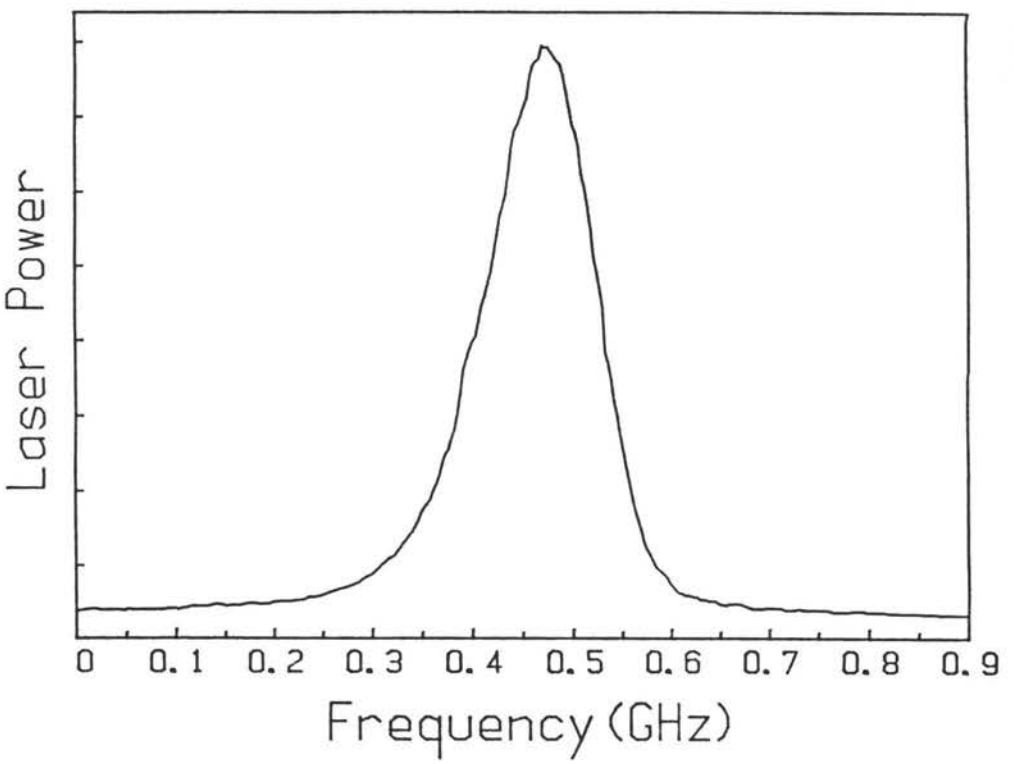

Fig. 3.4. Typical lineshape observed for the pulsed dye laser. The spectrum analyser has a bandwidth of 7 MHz

This figure demonstrates a nearly Fourier-transform-limited laser linewidth of 116MHz. For use in theoretical calculations the laser lineshape has been fitted with the following polynomial [3.8]

$$P(\nu) = \frac{C_1 C_2^3}{|(\nu/C_3)^3|+C_2^3} - C_4\nu \exp\left[\left(-\frac{\nu}{C_3 C_5}\right)^2\right] + C_6, \qquad (3.1)$$

where ν is in units of MHz and the constants are $C_1 = 123.2$, $C_2 = 4.318$, $C_3 = 13.426$, $C_4 = 2.194$, $C_5 = 8.618$ and $C_6 = 0.944$.

3.1.3 Probe Laser

The probe laser is a cw 3W Ar^+-ion laser (Coherent model CR-3). A prism in the laser cavity enables us to select the 514.5nm transition, which is used for our experiment. Furthermore we introduce a temperature stabilized etalon into the laser cavity to confine lasing to a single longitudinal mode. This arrangement results in roughly 200mw single mode output power and a linewidth of several megahertz, which is due to acoustical vibrations of the cavity. To reduce the temperature induced change of the cavity length which results in a slow frequency drift, we lock the argon laser frequency to the side of a Doppler broadened I_2 transition (Fig. (3.5)). We monitor both the total laser power with a photodiode and the iodine flourescence with a photomultiplier. The flourescence originates from a home made iodine cell, which is temperature stabilized to about ±0.1K. To lock the laser frequency to the half way point of the iodine flourescence we tune it with the internal etalon until we observe a flourescence level (photomultiplier voltage) of about half of the peak value.

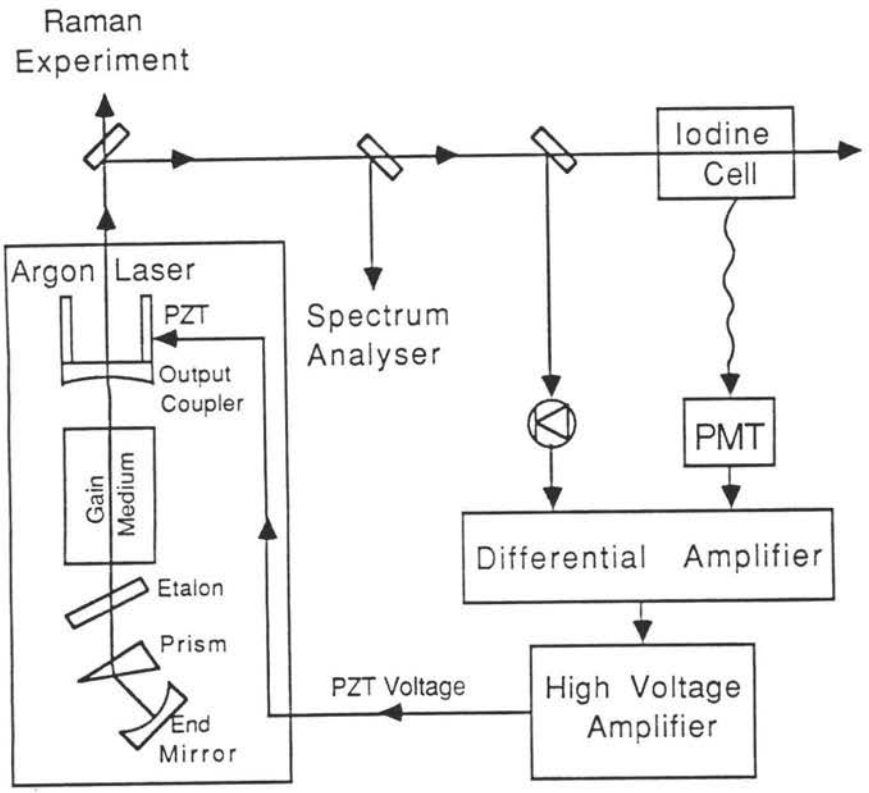

Fig. 3.5. Frequency stabilization of the argon ion laser

Then we regulate the amplification of either diode or photomultiplier until their output voltages are equal. The difference of their voltages is in first approximation independent of the laser power and proportional to the detuning of the laser frequency from the half way point. To lock the laser we obtain the difference voltage with a differential amplifier, amplify it, integrate it, add a bias voltage and apply the resulting voltage to a piezo-electric crystal (PZT). The bias voltage is chosen to be half of the maximum PZT voltage, starting the locking process with a PZT in mid position. By mounting the output

mirror on the PZT the applied voltage is proportional to a change in cavity length which in turn is proportional to a change in frequency, therefore closing the loop. The response time of the feedback loop is about 0.3s. Acoustical fluctuations of the cavity length are therefore not reduced while slow thermal drifts are eliminated. The probe laser output is also being monitored by a scanning confocal Fabry-Perot interferometer (spectrum analyser) to verify single mode operation.

3.1.4 Setup for Coherent Raman Spectroscopy

The argon laser beam is divided by a beam splitter into probe and reference beams. An astronomical telescope is used to match the probe laser beam size to to the beam size of the pump laser. With a standard telescope we would have to use a lens with different focal length to change the beam size. This procedure is fairly complicated, one needs a large supply of lenses and the optical readjustment is rather cumbersome. Therefore we replaced one of the lenses with a standard photographic zoom lens (28mm - 70mm), which enables us to change the beam size continuously by more than a factor of two, without having to replace lenses and without optical readjustment (Fig. (3.6)). The probe beam and the pump beam are overlapped with a dichroic mirror which transmits 60% of the probe laser beam at 514.5nm and reflects 99% of the pump laser beam at 584.5nm. Both beams enter the first nitrogen cell through a Brewster window and are focused by a 5-cm focal length air spaced achromatic lens. The focus of the beam is imaged into the second nitrogen cell by another achromatic 5-cm lens. We position this lens so that the second focus occurs 50cm behind this

lens. Therefore the second focus has ten times the spot size and 1% of the maximum intensity of the first focus. At the end of the second nitrogen cell we use a simple 50-cm lens to collimate both beams.

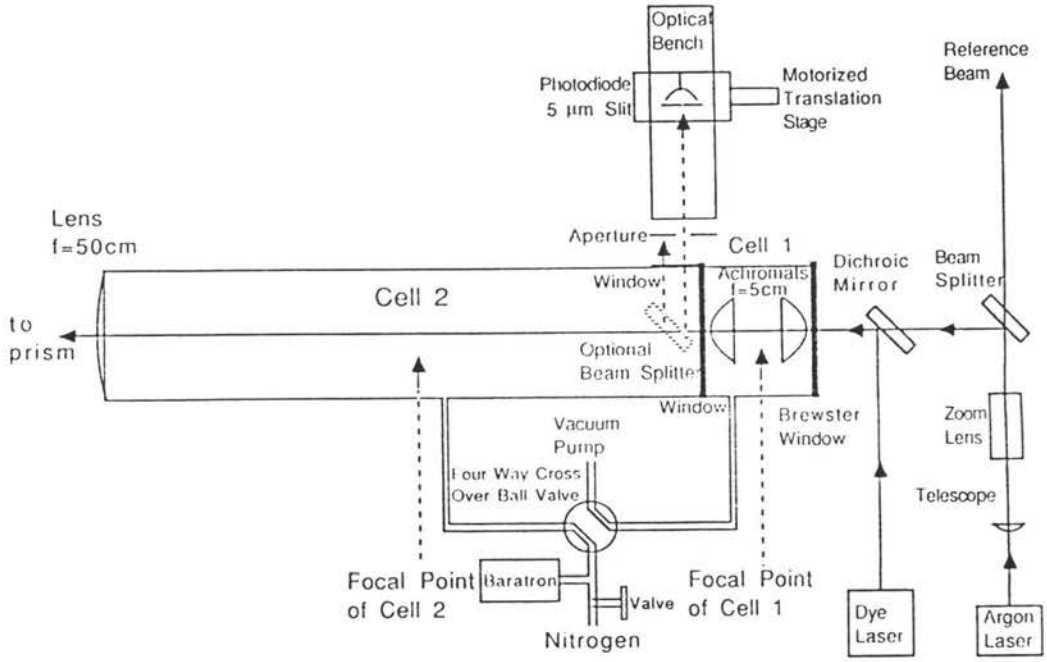

Fig. 3.6. Setup for coherent Raman spectroscopy with two gas cells

One of the cells is continuously evacuated by a mechanical pump, while the other cell is connected to a capacitive pressure meter (MKS Baratron) and can be filled from a nitrogen tank. All the Raman signal originates from the nitrogen filled cell while the evacuated cell does not contribute to the signal. Depending on the desired maximum intensity, one or the other cell is filled with nitrogen. We can reverse the filling of the cells by switching the connections with a

four-way crossover ball valve. This way it is possible to switch from mild focusing (cell 2 filled, spectra without Stark effect) to tight focusing (cell 1 filled, spectra with Stark effect) within less than a minute, without any optical realignment (Fig. (3.6)).

At the front end of the second gas cell we can insert a parallel glass plate to reflect part of the beam out of the cell. One of the two reflections is blocked upon exit out of the cell. The other beam can be profiled by the following arrangement (Fig. (3.6)). A photodiode, mounted directly behind a 5μm slit is scanned with a motorized translation stage (Oriel motor mike) across the beam. The synchronization pulses of the optical encoder of the translation stage are used to trigger the digital data aquisition, which records the beamprofile. In the case of a cw beam the photodiode output is just amplified and digitized, while for pulsed input, we use a gated integrator to sample the signal and store it between laser pulses for digitization. The translation stage is mounted on an optical bench parallel to the beam. This way it can be easily moved to acquire beam profiles at different distances from the focal point. This way focal point, Rayleigh length and spot size of both beams can be determined and matched. This procedure is rather time consuming, but once it has been completed, it does not have to be repeated until the basic setup is changed.

Behind the second gas cell we separate probe beam, pump beam and CSRS beam with a prism. About one meter behind the prism, we block the pump beam with a beam dump. The pump power is about twelve orders of

magnitude larger than the power of the CSRS beam. Therefore we have to take great care to suppress even minute traces of stray light from the pump beam. The CSRS beam is spectrally filtered by a series of colored glass and interference filters. Then it is focused into the entrance slit of a half meter monochromator, which is set on the CSRS wavelength (676.7nm for the Q-branch of N_2). The spectral filtering eliminates pump laser light (λ = 584.5nm) rather completely. Finally a photomultiplier, mounted behind the exit slit of the monochromator detects the CSRS signal. Probe and reference beams are spectrally filtered with spike filters for the argon 514.5nm line. Before the detection with fast photodiodes we use iris diaphragms to match the power of probe and reference beam.

3.1.5 Detection Electronics and Computerized Data Acquisition

To detect the IRS signal we use two high speed photodiodes, one for the probe and one for the reference beam. The photodiodes are EG&G, model FND 100 (rise time less than lnsec), which are operated in the reversly biased (photo conductive) mode. The source of the bias voltage must be fairly noise free, thus we use 90V batteries. To reduce laser noise and obtain the IRS signal, we connect the photodiodes in a subtraction scheme, as shown in Fig. (3.1). To subtract out the laser intensity, we have to take care that the path lengths of probe and reference beams are approximately equal. After subtraction the photodiodes are capacitively (C = 400pF) coupled to the 50Ω input of a 300MHz bandwidth preamplifier (Ortec model 9301 or

Phillips Scientific model 6950). The capacitor and the 50Ω input impedance act as a high-pass filter which transmits the 5nsec signal but blocks noise below 10MHz.

The CSRS signal is detected by a photomultiplier (ITT model FW-130) which is biased by a standard high voltage power supply. Its signal is amplified by another 300MHz preamplifier. After further amplification (Phillips Scientific model 770), both IRS and CSRS signals are gated (10nsec, 30nsec gate width, respectively) and stored between pulses by gated integrators (Stanford Research model SR250). We do not use the averaging capabilities of these instruments, but digitize and store the signals for every single shot. For this purpose we use a data aquisition system (Data Translation model DT 2781) with 8 differential A/D (analog to digital) and 2 D/A (digital to analog) channels. This system consists of a single width board for insertion in the backplane of our laboratory computer (Digital Equipment LSI 11/23). The data are finally stored on floppy disks. Besides IRS and CSRS signal, we record the saturated iodine and interferometer spectra simultaneously. At the beginning of each scan the laboratory computer also records the nitrogen pressure in the filled gas cell. At each discrete dye laser frequency the computer records the signal of the four input channels for each individual Nd-Yag laser pulse. After eight pulses it steps the dye laser to the next discrete frequency. One full scan consists of 1024 such steps and consequently out of 8192 data points for each of the four input channels. All of these data points are stored on floppy disks for further analysis.

3.2 Experimental Results and Comparison with the Theory

Using the setup discussed in section 3.1 , we have recorded spectra of several lines in the vibrational Q-branch ($v = 0 \rightarrow v \rightarrow 1$) of molecular nitrogen (N_2) under various experimental conditions. In this section, we first discuss our frequency linearization and frequency reference procedures, before we compare experimental spectra without and with the influence of optical Stark effect with respective theories.

Simultaneously recorded IRS, CSRS, iodine (I_2) and Fabry-Perot (F-P) spectra are shown in Fig.'s (3.7a-d) (9/Sept/1986, 17:30:36), respectively. Each spectrum consists of 2^{10} (i.e. 1024) data points, each averaged over 8 laser pulses at a constant dye laser frequency (Sec. 3.1.5). The peak height fluctuations of the Fabry-Perot transmission spectrum (Fig. (3.7d)) are largely due to the limited number of data points used, 2^{10} frequency steps are just enough to identify all Fabry-Perot peaks in a 7GHz scan. For scans longer than 7GHz a larger number of frequency steps would become necessary for the frequency linearization procedure. The common x-axis is a frequency scale derived from the analog voltage, which controls the dye laser scan, assuming a linear relationship between this voltage and the dye laser frequency. Due to the existence of unpredictable nonlinearities in the laser scan mechanism, the relationship between this voltage and the actual laser frequency is neither exact nor reproducible. The irreproducible nonlinearities of our system are in the order of several percent.

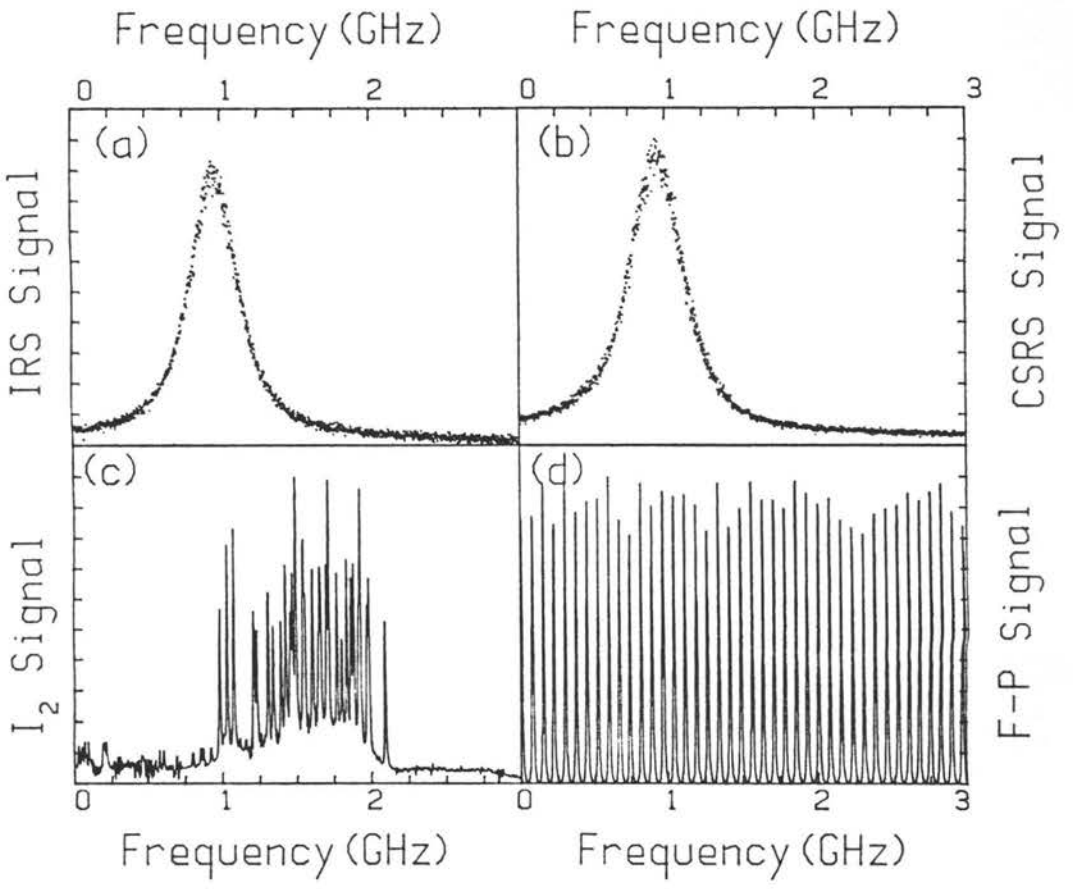

Fig. 3.7. Simultaneously recorded data (9/Sept/86, 17:36:30)

(a) IRS spectrum of the l=4 vibrational Q-branch transition (v=0 → v=1) in molecular nitrogen

(b) CSRS spectrum of the l=4 vibrational Q-branch transition (v=0 → v=1) in molecular nitrogen

(c) Doppler free spectrum of molecular iodine

(d) Transmission spectrum of the 75MHz Fabry-Perot interferometer

This nonlinearity is clearly seen in Fig. (3.8a), where we plot a portion of the Fabry-Perot transmission spectrum previously shown in Fig. (3.7d) against the frequency derived from the analog voltage, with a grid spacing corresponding to the free spectral range (FSR = 74.295MHz) of the Fabry-Perot (Sec. 3.1.2).

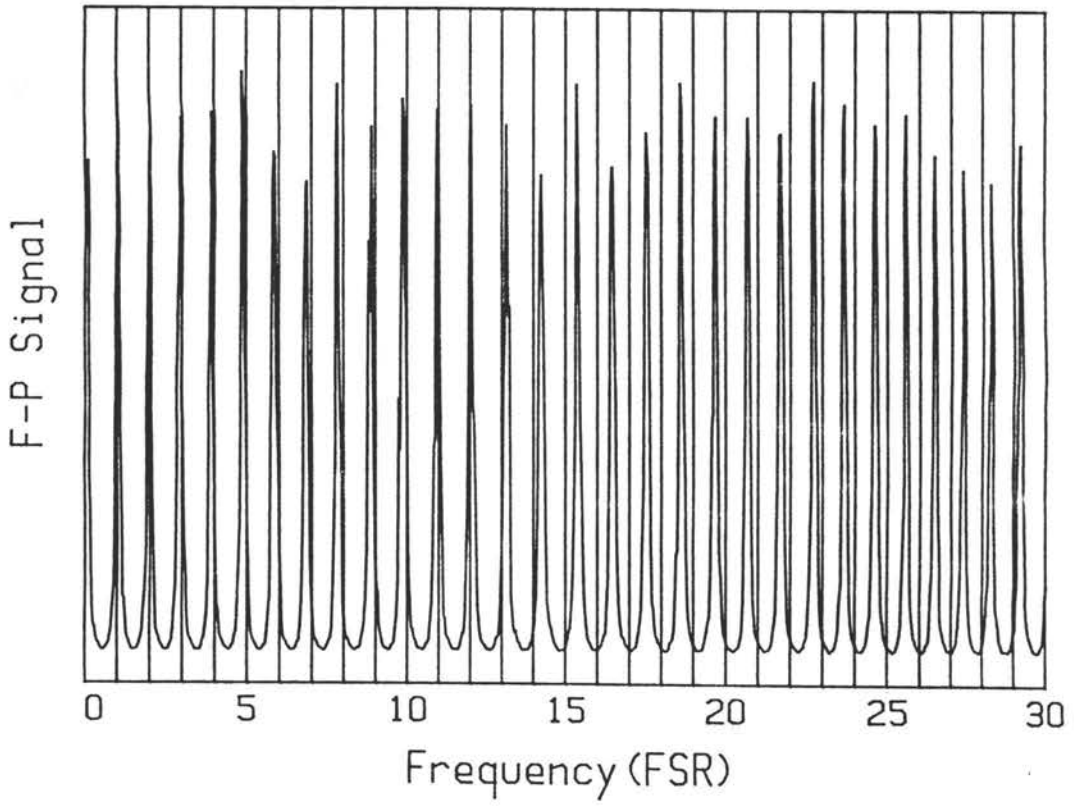

Fig. 3.8a. Part of the Fabry-Perot spectrum in Fig. (3.7d) with a frequency scale derived from the dye laser voltage

Obviously the spacing of the transmission peaks does not agree with the grid spacing. To construct an improved frequency scale, nearly linear in light frequency rather than proportional to the analog voltage, we use the Fabry-Perot peaks as equidistant frequency

markers. To determine their position as well as possible, we fit the transmission Airy formula, which is the theoretical description of the transmitted intensity [3.9], to each pair of neighboring peaks. This gives us the change in dye laser voltage corresponding to the free spectral range of the Fabry-Perot, for each pair of neighboring peaks. A new frequency scale is then constructed by linear interpolation between the peaks. Figure (3.8b) shows the spectrum of Fig. (3.8a) plotted against the new linearized frequency scale; the improvement is obvious.

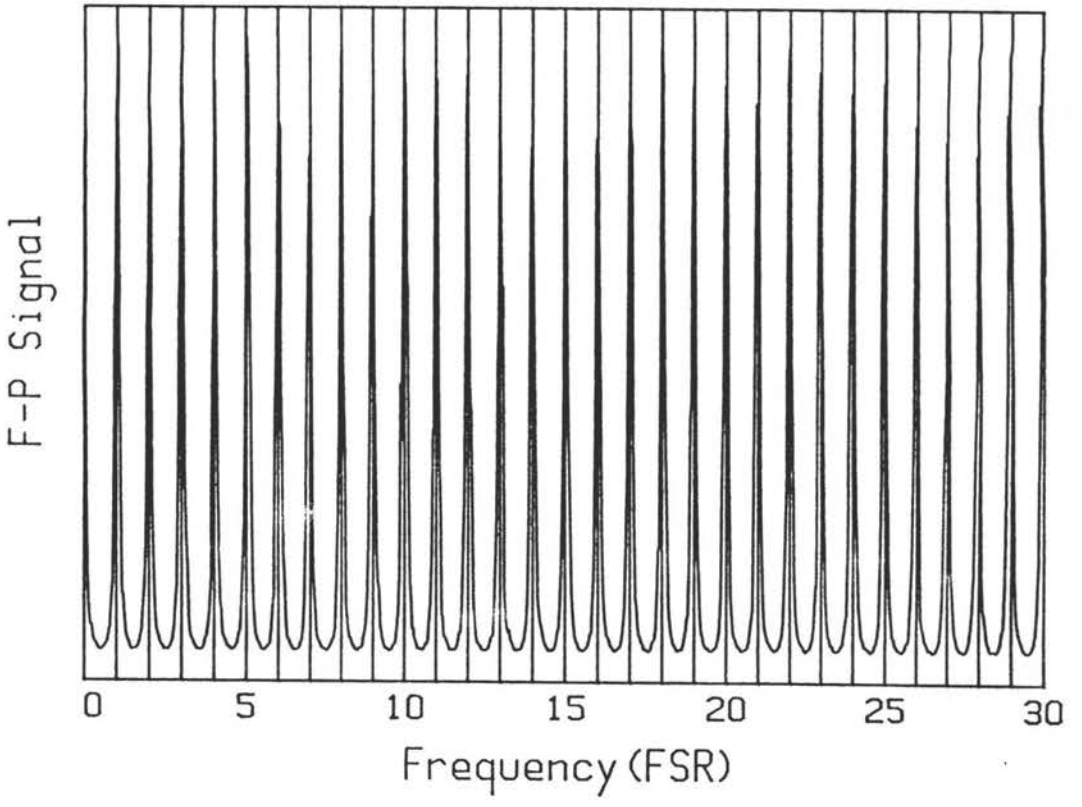

Fig. 3.8b. Part of the Fabry-Perot spectrum in Fig. (3.7d) with a linearized frequency scale derived from Fabry-Perot peaks

We have further checked this procedure by comparing the iodine spectra, as shown in Fig. (3.7c), of several different scans over the same frequency range. The linearization of the frequency scale leads to excellent agreement between the respective peak positions of different I_2 scans. The frequency scales of all experimental spectra shown in the following sections have been linearized by this procedure. Furthermore, we can establish a common frequency scale for different scans by overlapping their respective iodine spectra (Fig. (3.7c)). This procedure is legitimate only for spectra taken on the same day, because the lock point of the Ar^+ laser will differ from day to day. A common frequency scale for scans from different days may still be established by overlapping non-Stark broadened scans taken under identical conditions. Spectra for most experimental conditions have been recorded several (up to 20) times. The spectra actually shown are typical examples of the spectra with good signal to noise ratio.

3.2.1 Spectra without Stark Broadening

To record spectra without Stark broadening, we have evacuated cell one, while cell two is filled with N_2 at 10kPa. We first discuss the spectra of the Raman line with the rotational quantum number l=4. Simultaneously recorded IRS and CSRS spectra of l=4 are shown, respectively, in Fig. (3.9a) and Fig. (3.9b) (9/Sept/1986, 17:30:36). Each of the 2^{10} points corresponds to a Raman signal averaged over eight dye laser pulses.

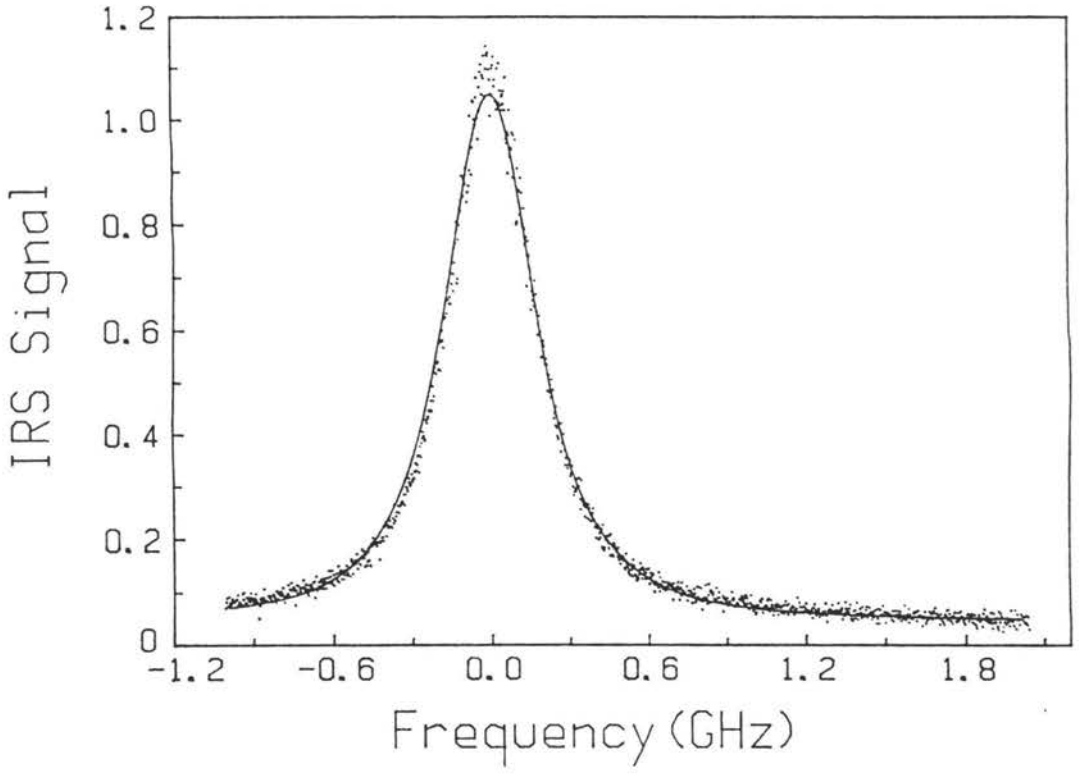

Fig. 3.9a. Comparison between theoretical (solid curve) and experimental (dots) IRS spectra of the l=4 vibrational Q-branch transition (v=0 → v=1) in molecular nitrogen (N_2), plotted as a function of $\Delta\omega$; i.e. with the dye laser scanned towards higher frequency (smaller Raman shift)

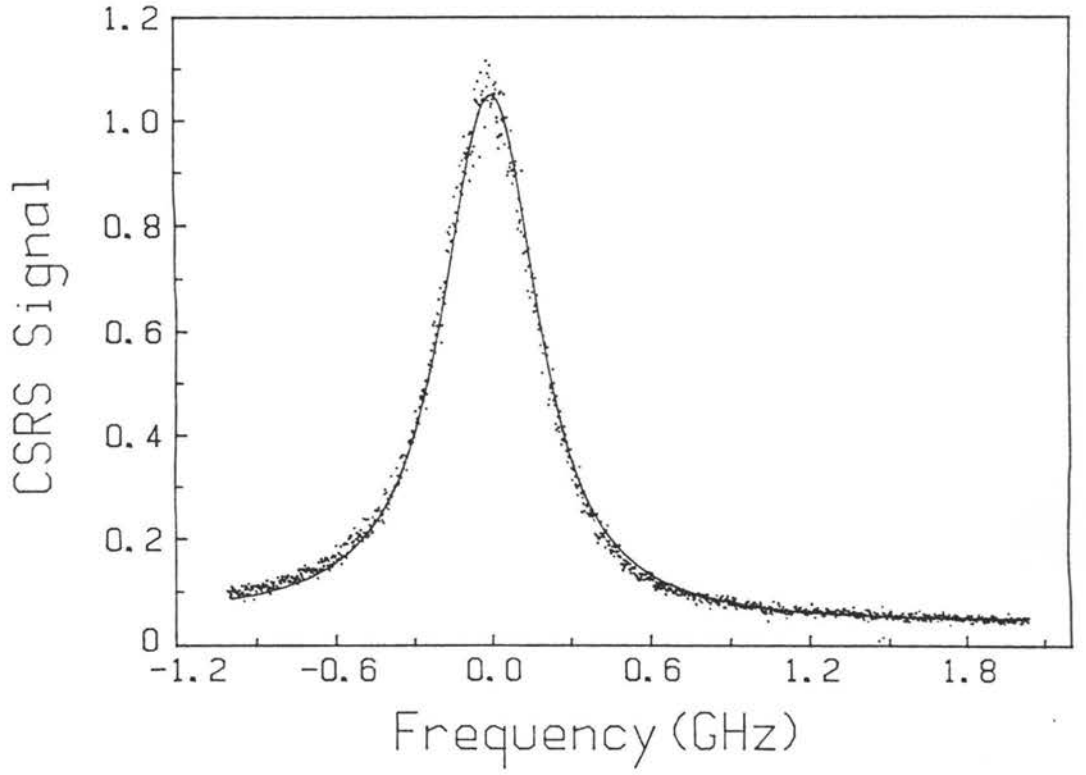

Fig. 3.9b. Comparison between theoretical (solid curve) and experimental (dots) CSRS spectra of the l=4 vibrational Q-branch transition (v=0 → v=1) in molecular nitrogen (N_2), plotted as a function of $\Delta\omega$; i.e. with the dye laser scanned towards higher frequency (smaller Raman shift)

To compare experimental IRS and CSRS spectra directly, we have applied a 25-point smoothing routine [3.10] to the data in Fig.'s (3.9a) and (3.9b). The resulting experimental spectra are both shown in Fig. (3.9c).

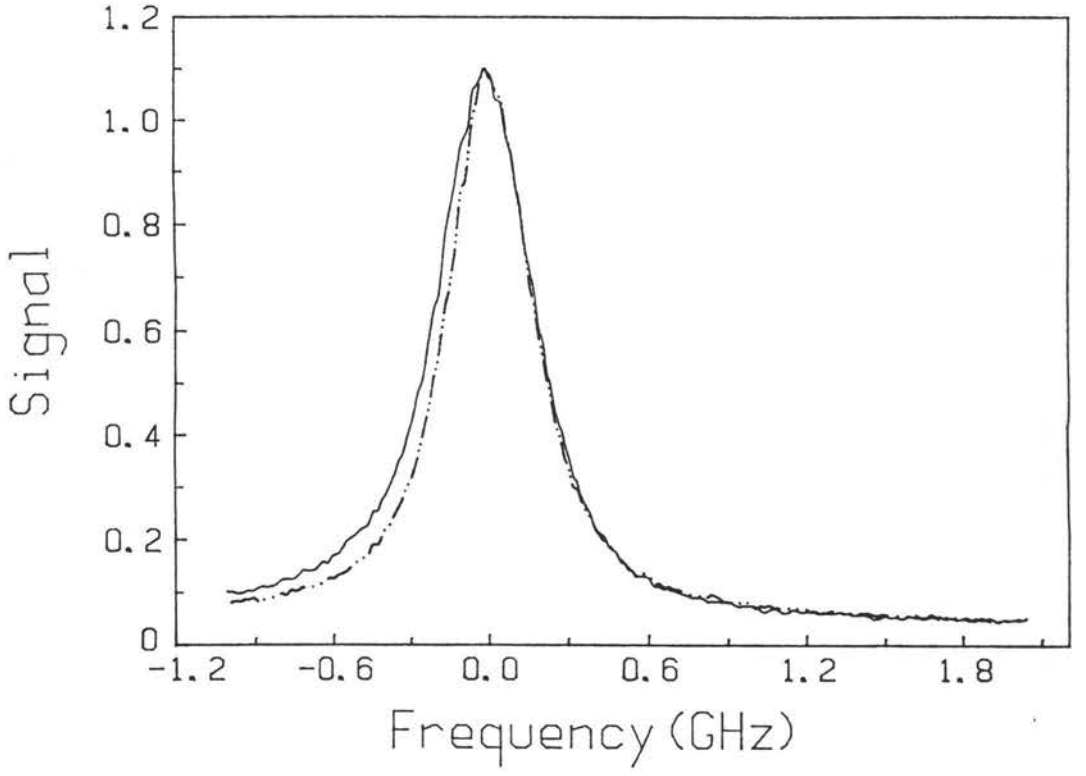

Fig. 3.9c. Comparison between experimental IRS (dotted curve) and CSRS (solid curve) spectra of the 1=4 vibrational Q-branch transition (v=0 → v=1) in N_2, plotted as a function of $\Delta\omega$

In this figure one recognizes two main differences between CSRS and IRS; the CSRS spectrum (solid curve) is wider and shifted to the left (larger Raman shift), as compared with the IRS spectrum (dotted curve). The difference in width can be accounted for quantitatively by

proper inclusion of the effect of Doppler broadening on Lorentzian lines. The IRS spectra have the usual Voigt shape, while the CSRS spectra show additional broadening that is due to interference between the contributions of different velocity subgroups to the real part of the third-order nonlinear susceptibility. Additionally, we must take the finite widths of the pulsed dye laser into account. This has been done exactly the same way as discussed in section 2.2.2 for the Doppler linewidth. The relative importance of the different broadening mechanisms depends on the experimental conditions. A gas temperature of 292K leads to a Doppler broadening of 161MHz (FWHM) for copropagating laser beams probing the 2330-cm^{-1} Raman transitions [3.2] in N_2. A pressure of 10kPA along with pressure-broadening coefficients given by Rosasco et al. [3.11] corresponds to a Lorentzian linewidth of roughly 270MHz (FWHM), depending on the specific line. While we can neglect the Ar^+-ion laser linewidth of several megahertz, we have to take the linewidth and line shape of the pulsed dye laser into account (section 3.1.2). Furthermore, we must calculate the influence of neighboring Raman lines. Using a Lorentzian approximation for the neighboring lines, we add up the contributions of all lines from l=0 to l=29 using Eq. (2.119). At 292K, these lines represent more than 99.9% of the Q-branch intensity. Figure (3.9d) shows the theoretical results for l=4, while Fig.'s (3.9a) and (3.9b) compare theory (solid curves) with experiment. From these figures it becomes clear that the theoretical calculations reproduce the experimental spectra well.

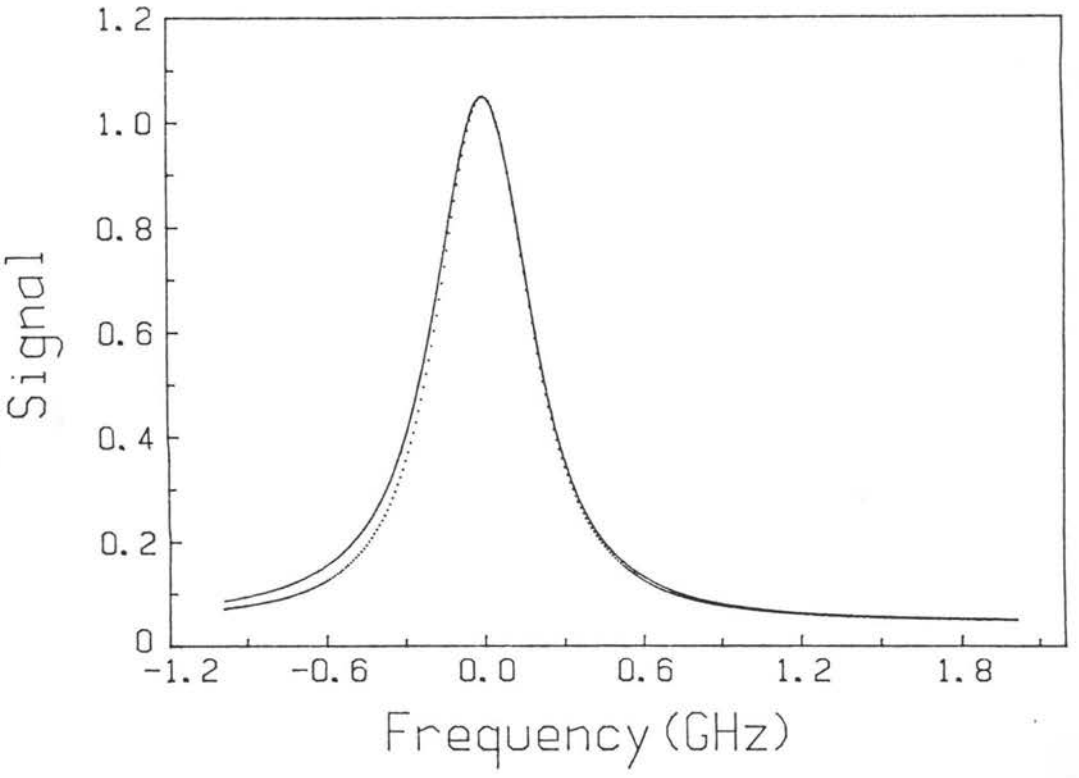

Fig. 3.9d. Comparison between theoretical IRS (dotted curve) and CSRS (solid curve) spectra of the l=4 vibrational Q-branch transition (v=0 → v=1) in N_2, plotted as a function of $\Delta\omega$

It should be pointed out that our theoretical curves are generated by using widths, calculated directly from our experimental conditions. We have fitted only signal strengths, zero offset of the signal and absolute frequency, which have not been determined experimentally. All other parameters, such as frequency shift between IRS and CSRS spectra, have not been adjusted in any way; in this manner, we are able to make a direct comparison between experiment and theory.

Figures (3.10a - 3.10d) show the same kind of plots for the l=12 line (7/Oct/1986, 19:29:58).

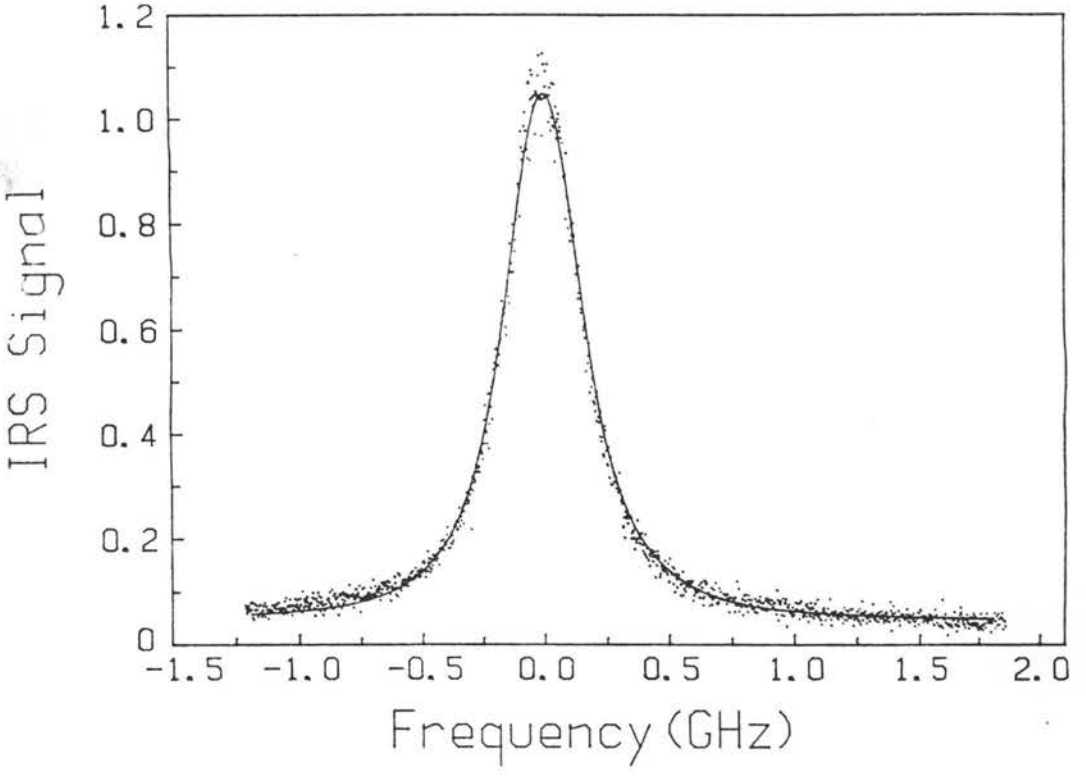

Fig. 3.10a. Comparison between theoretical (solid curve) and experimental (dots) IRS spectra of the l=12 vibrational Q-branch transition (v=0 → v=1) in molecular nitrogen (N_2), plotted as a function of $\Delta\omega$; i.e. with the dye laser scanned towards higher frequency (smaller Raman shift)

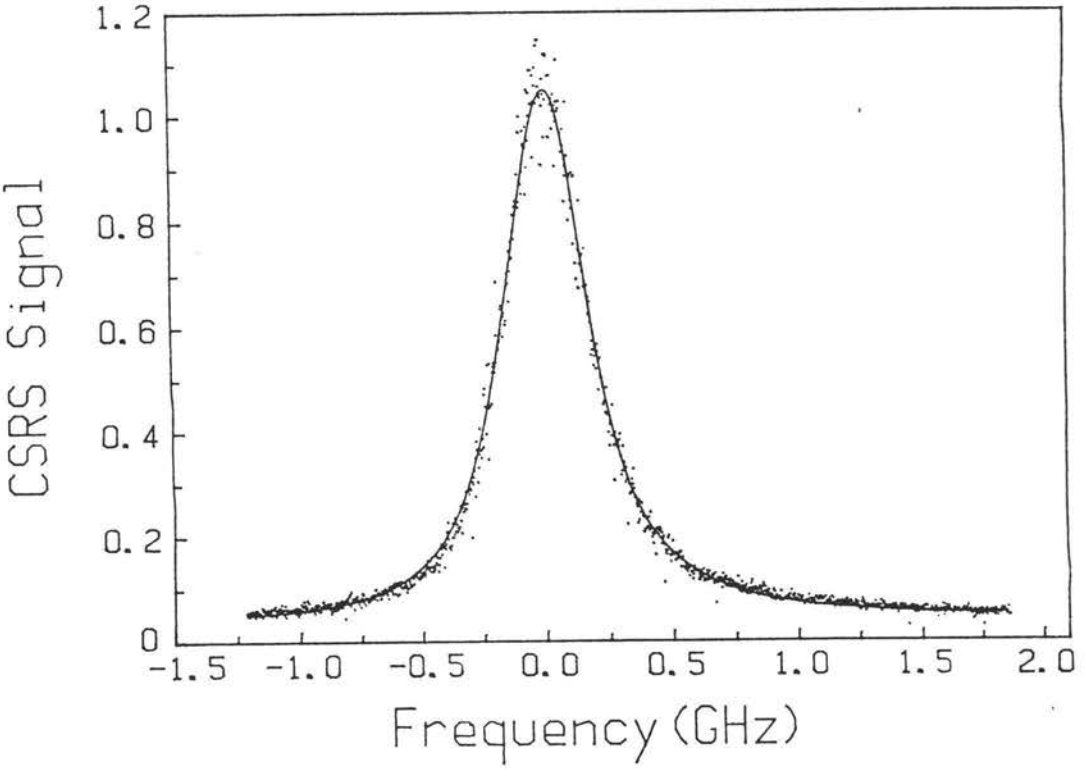

Fig. 3.10b. Comparison between theoretical (solid curve) and experimental (dots) CSRS spectra of the l=12 vibrational Q-branch transition (v=0 → v=1) in molecular nitrogen (N_2), plotted as a function of $\Delta\omega$; i.e. with the dye laser scanned towards higher frequency (smaller Raman shift)

Again we notice good agreement between theory and experiment. While linewidths and line shapes are comparable to those of l=4, we notice that the CSRS line is shifted to the right (smaller Raman shift), (Fig. 3.10c, Fig. 3.10d), instead of to the left as for the l=4 line.

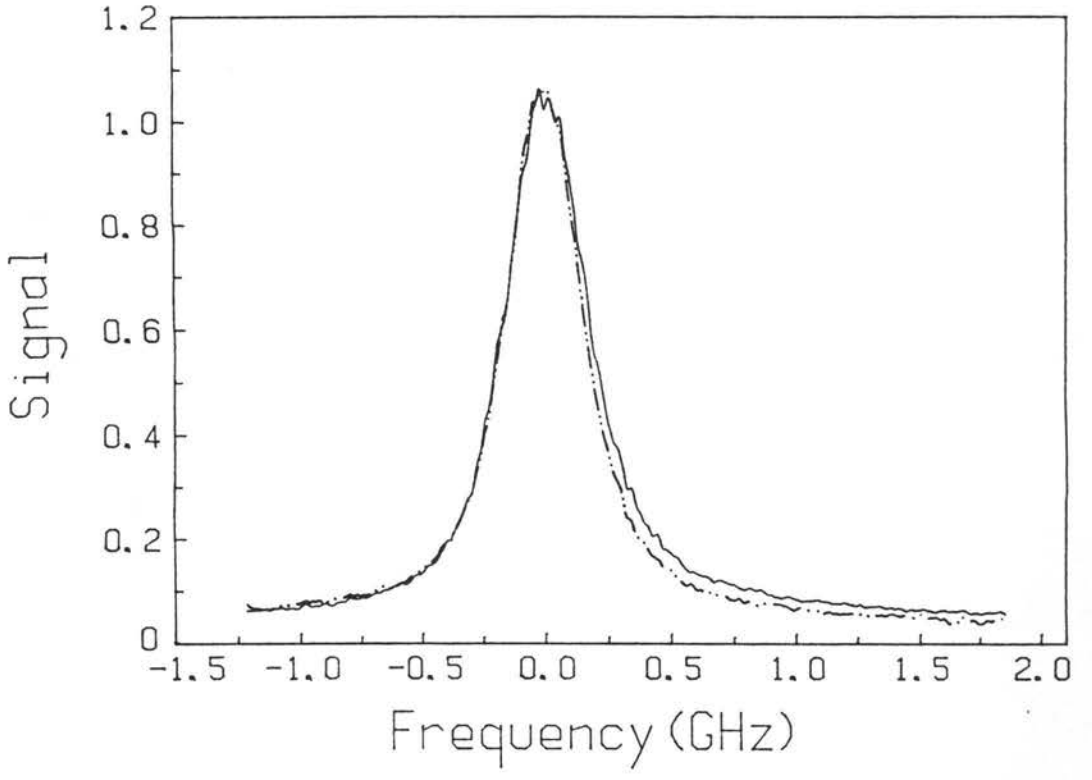

Fig. 3.10c. Comparison between experimental IRS (dotted curve) and CSRS (solid curve) spectra of the J=12 vibrational Q-branch transition (v=0 → v=1) in molecular nitrogen (N_2), plotted as a function of $\Delta\omega$; i.e. with the dye laser scanned towards higher frequency (smaller Raman shift)

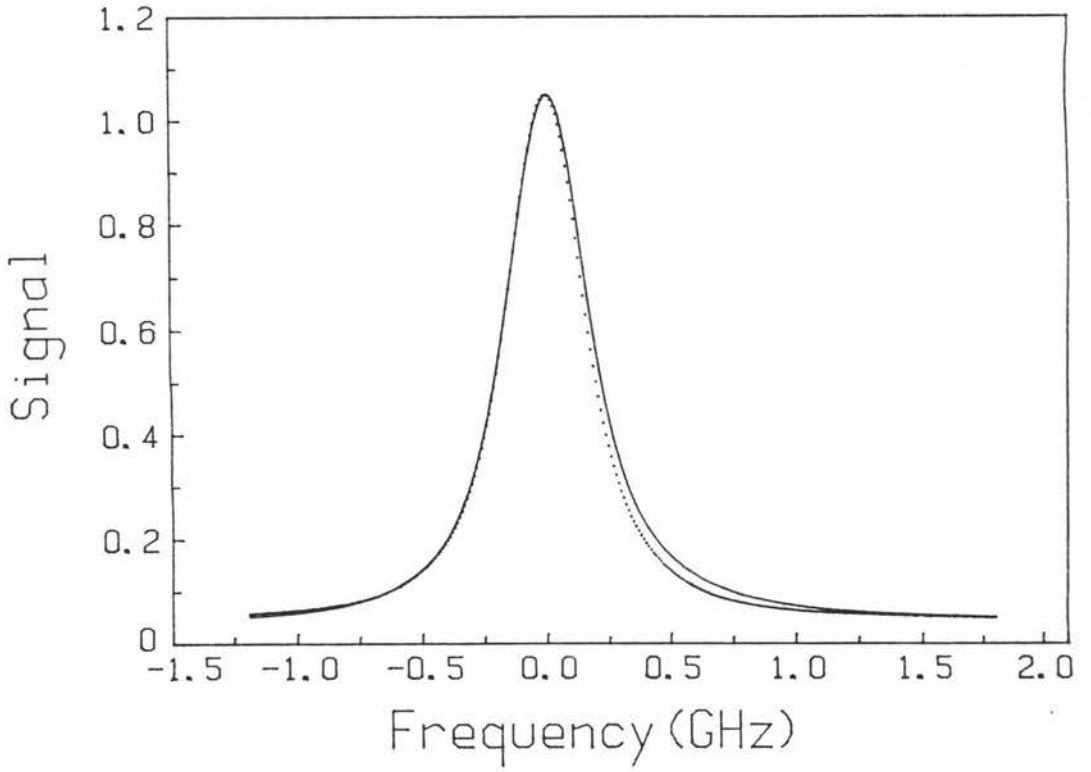

Fig. 3.10d. Comparison between theoretical IRS (dotted curve) and CSRS (solid curve) spectra of the l=12 vibrational Q-branch transition (v=0 → v=1) in N_2, plotted as a function of $\Delta\omega$

To understand this result of experiment and theory, we must take a closer look at all rotational lines in the Q-branch of N_2. Table 3.1 gives relative Raman shifts F(l) and intensities $\phi(l)$ for various lines of the Q-branch [3.12]. One can see that the strongest lines, and thus the main source of the nonresonant susceptibility χ'_{NR} are located between l=4 and l=12. As discussed in section 2.2.3, CSRS lines are shifted away from the source of χ'_{NR}, i.e., l=4 to the left and l=12 to the right, explaining our experimental and theoretical

results. To see this in a more quantitative way, we have listed in table 3.1 the ratio of the nonresonant susceptibility due to all neighboring lines $[\chi'_{NR}(F(l)) = \sum_{I=0}^{\infty} \chi'_I(F(l))]$ to the resonant susceptibility $\chi''_J(F(l))$ at the center of each line l.

Table 3.1. Spectroscopic data for some lines in the Q-branch of N_2 at 292K and 10kPa

l	F(l)(GHz)	Φ(l)	$\sum_{I=0}^{\infty} \chi'(F(I))/\chi''(F(l))$
0	0.00	0.0130	2.0941
1	-1.04	0.0191	0.9265
2	-3.13	0.0614	0.1723
3	-6.25	0.0405	0.1664
4	-10.42	0.0963	0.0362
5	-15.64	0.0534	0.0239
6	-21.89	0.1121	-0.0027
7	-29.19	0.0564	-0.0290
8	-37.53	0.1093	-0.0213
9	-46.91	0.0512	-0.0588
10	-57.33	0.0930	-0.0332
11	-68.80	0.0411	-0.0805
12	-81.31	0.0706	-0.0436
13	-94.86	0.0296	-0.1022
14	-109.45	0.0483	-0.0541
15	-125.09	0.0192	-0.1262
16	-141.77	0.0299	-0.0681
17	-159.49	0.0114	-0.1560
18	-178.25	0.0169	-0.0866
19	-198.06	0.0061	-0.2092
20	-218.90	0.0087	-0.1293

Here we notice that the relative magnitude of x'_{NR} is nearly identical for l=4 and l=12 but with a different sign because of the nature of dispersion, leading to opposite shifts. These nonresonant susceptibilities are temperature and pressure dependent. Therefore not

only do SRS and FWMRS spectra have different peak positions but also the peak positions in FWMRS spectra shift as a function of pressure and temperature. This effect, for example, led to problems with systematic errors in previous CSRS velocity measurements in supersonic flows, while IRS measurements are unaffected [3.13].

Finally let us take a look at spectra of the l=0,1, and 2 lines, as shown in Fig.'s (3.11a - 3.11d) (7/Oct/1986, 20:48:01).

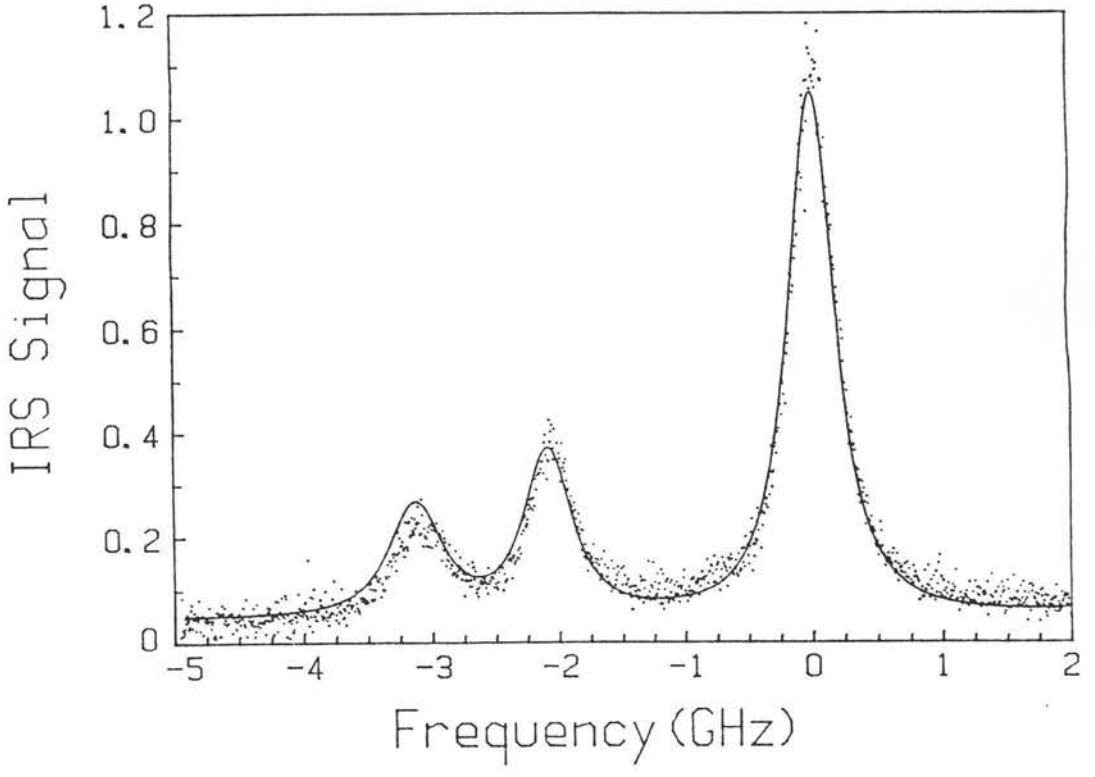

Fig. 3.11a. Comparison between theoretical (solid curve) and experimental (dots) IRS spectra of the l=0, 1, and 2 vibrational Q-branch transitions (v=0 → v=1) in molecular nitrogen, plotted as a function of $\Delta\omega$

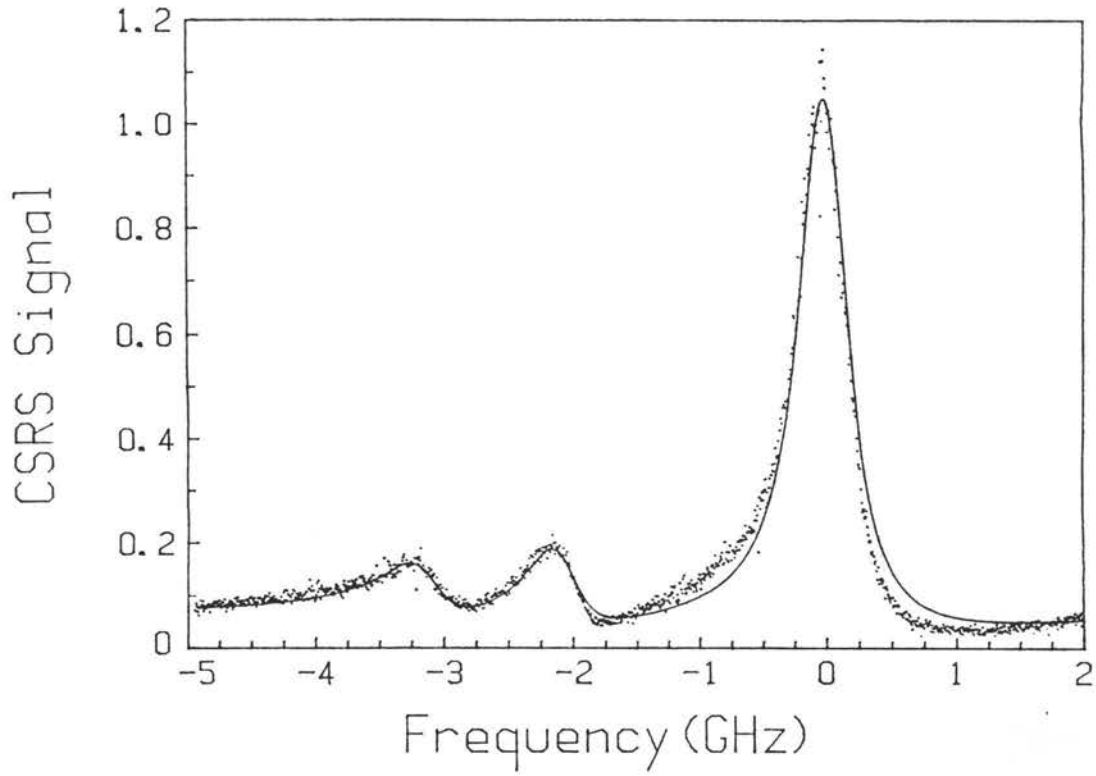

Fig. 3.11b. Comparison between theoretical (solid curve) and experimental (dots) CSRS spectra of the l=0, 1 and 2 vibrational Q-branch transitions (v=0 → v=1) in molecular nitrogen (N_2), plotted as a function of $\Delta\omega$

Here we notice larger differences between CSRS and IRS spectra, than in the case of the l=4 and l=12 lines. CSRS spectra have large asymmetries and peak shifts, and even IRS spectra start to show some asymmetry and line overlap. These larger effects are due to the close line spacing near the head of the Q branch (l=0), and the higher intensity of the neighboring higher-l lines.

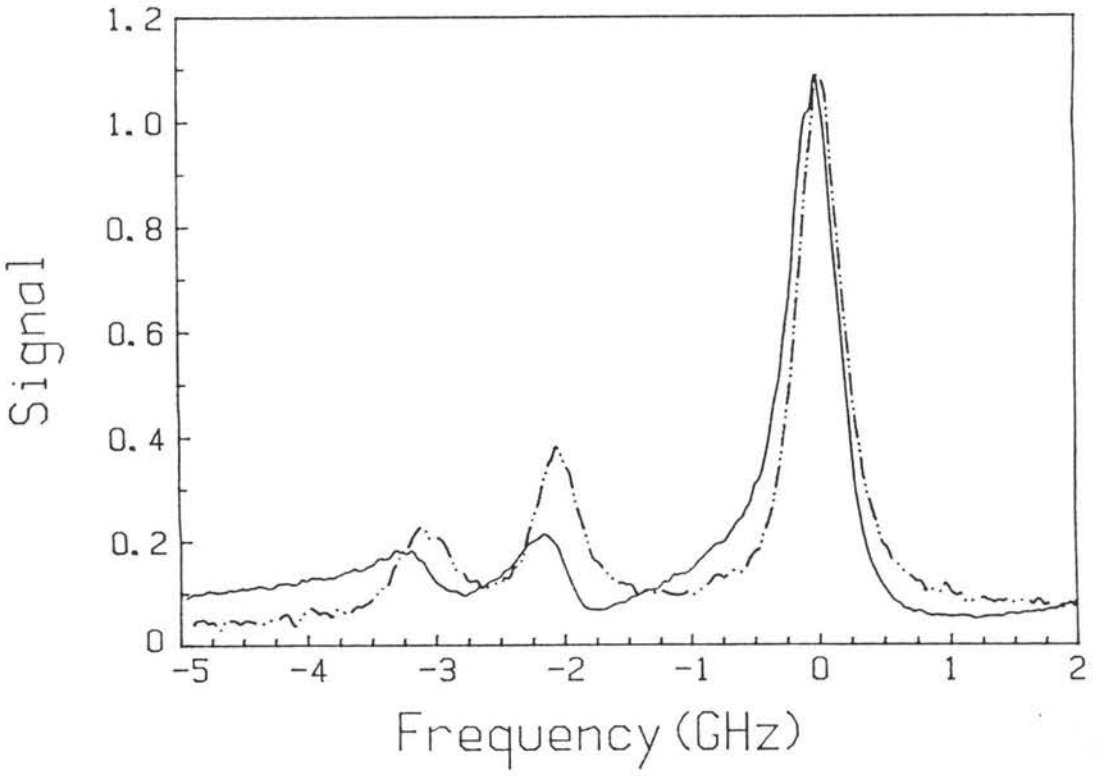

Fig. 3.11c. Comparison between experimental IRS (dotted curve) and CSRS (solid curve) spectra of the l=0, 1 and 2 vibrational Q-branch transitions (v=0 → v=1) in N_2 as a function of $\Delta\omega$

To account for these obvious differences, we again use Eq.'s (2.118) and (2.119). For simplicity, we used correctly convoluted line shapes (pressure, Doppler, laser line shapes) only for contributing lines up to l=4, while for higher-l lines we simply use the approximation of a Lorentzian shape with a width corresponding to the pressure broadening. We obtain good agreement between theory and experiment, but, on a closer look, one recognizes some minor discrepancies between experimental and theoretical line shapes (Figs. (3.11a,b).

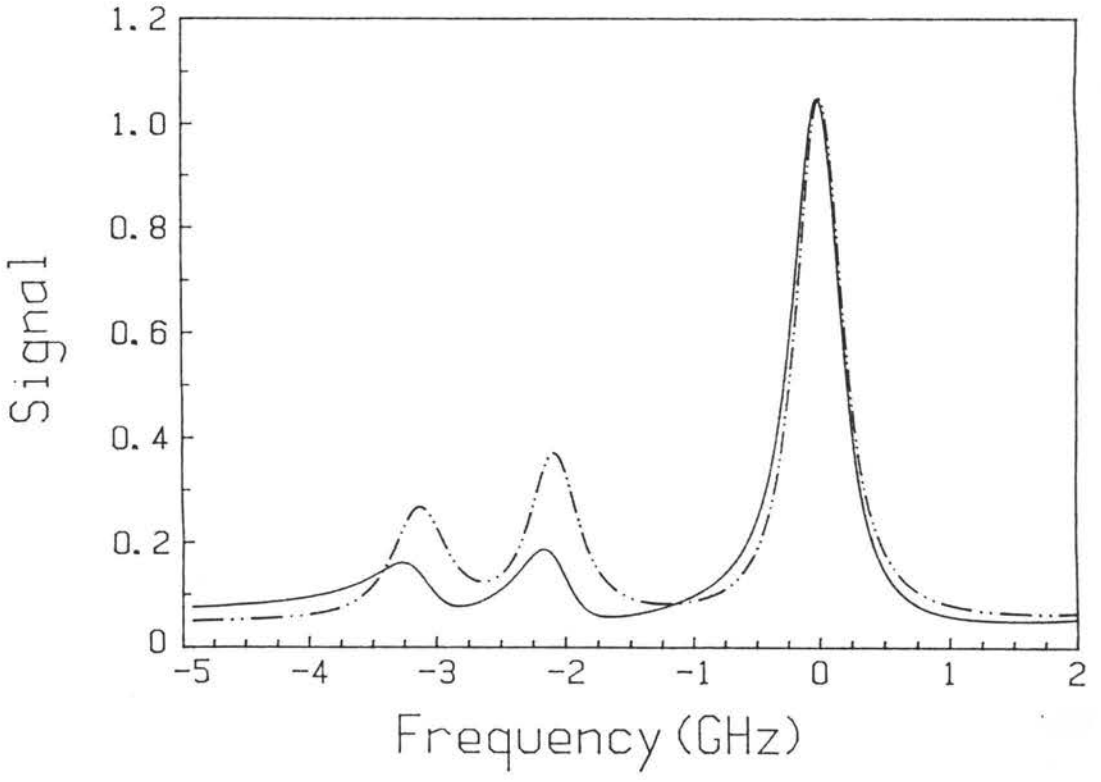

Fig. 3.11d. Comparison between theoretical IRS (dotted curve) and CSRS (solid curve) spectra of the 1=0, 1 and 2 vibrational Q-branch transitions (v=0 → v=1) in N_2, plotted as a function of $\Delta\omega$

The source of these minor discrepancies is unclear. While it would become necessary to include coherent line mixing [3.11] into calculations for experiments at higher pressures, this effect does not account for the discrepancies under our experimental conditions. We have also investigated the electronic contribution to the nonresonant susceptibility; it again is negligible for our conditions.

3.2.2 Stark Broadened Spectra

Alternating with the non-Stark broadened spectra analysed in section 3.2.1, we have used cell one (f = 5cm) to record spectra which show appreciable Stark broadening. In order to estimate the peak intensity in this cell, we measure the beam profiles of both pulsed and cw laser beams. The analysis for determining beam parameters is given in section 3.2.2.1. In the following sections we proceed to compare the simultaneously recorded IRS and CSRS spectra with calculations, following the theoretical results of section 2.2.4.2.

3.2.2.1 Beam Profiles

Using the arrangement described in section 3.1.4 we have obtained profiles of the laser beams in cell two. Profiles taken on 9/Sept/86 will be used to estimate the peak energy density and intensity in cell one. To obtain transverse beam profiles we scan a 5μm slit across the respective laser beam which has been reflected out of cell two with the help of an optional beam splitter, as shown in Fig. (3.6). Such profiles are shown, as solid lines, for the cw Ar^+ and the pulsed dye laser beam in Fig. (3.12a) and Fig. (3.12b), respectively. To determine the beam radius ($1/e^2$ points of the intensity), we have fitted Gaussians (dotted lines) to both curves. We note that, despite a slight asymmetry, the experimental results agree rather well with the Gaussian fit. Nine to ten transverse beam profiles were acquired for each beam, varying the distance from the focusing lens by roughly 5cm (2") between the individual profiles. The resulting beam radii (squares) together with a theoretical fit (solid line, Eq. (2.125)),

which describes the beam sizes along the propagation axis, are shown in Fig.'s (3.12c) and (3.12d).

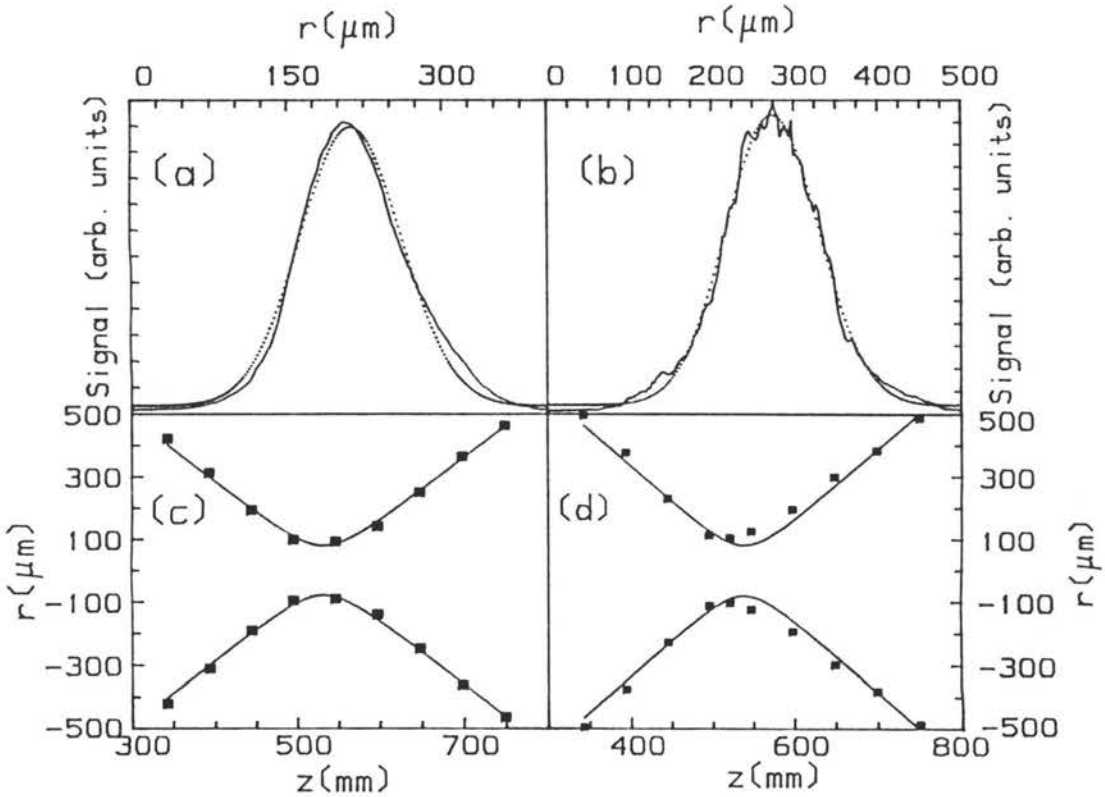

Fig. 3.12. Results of beam profiling

(a) Beam profile of the cw Ar^+ laser (solid line) together with a Gaussian fit (dotted line)

(b) Beam profile of the pulsed dye laser (solid line) together with a Gaussian fit (dotted line)

(c) Measured beam radii of the cw Ar^+ laser (squares) together with a theoretical fit (solid curves)

(d) Measured beam radii of the pulsed dye laser (squares) together with a theoretical fit (solid curves)

The theoretical fit assumes that the Rayleigh length z_0 and the spot radius w_0 are related by $z_0 = \pi w_0^2/\lambda$, where λ is the laser wavelength (section 2.2.4.1). We note that while we do not have perfect Gaussian beams, the Gaussian approximation with identical parameters for both beams appears to be reasonable. According to Fig. (3.12d), the focus of the pulsed beam occurs in a distance of $z_2 = 540\text{mm} \pm 5\%$ from the imaging lens with a spot radius of $w_{02} = 80\mu\text{m} \pm 20\%$. The error limits are not the result of a statistical analysis of the fit, but an educated guess. We use geometrical optics to calculate the spot radius in cell one as

$$w_{01} = w_{02} \frac{f}{z_2 - f} = 8.2\mu\text{m} \pm 21\%. \qquad (3.2)$$

This result would change by less than one part in 10^4, if we would have used the correct formula for Gaussian beams [3.14]. The measured average power of the pulsed dye laser is 55mW ± 20% at a repetition rate of 10Hz, corresponding to an energy of 5.5mJ ± 20% per pulse. We use Eq. (2.126b) to calculate the peak energy density at the focal point (z = 0, r = 0) as

$$ED_0 = \frac{2}{\pi} \frac{E}{w_0^2} = 5.2\ 10^7 \frac{J}{m^2} \pm 45\%. \qquad (3.3)$$

To estimate the peak intensity of the dye laser pulse, we have measured its time evolution with a fast photodiode (Opto-Electronics model PD10, rise time < 100psec) and a 500MHz storage oscilloscope. A few examples of the time evolution are shown in Fig. (3.13). The irregular spiking, which changes from pulse to pulse is due to the beating of longitudinal modes in the Nd-Yag laser cavity.

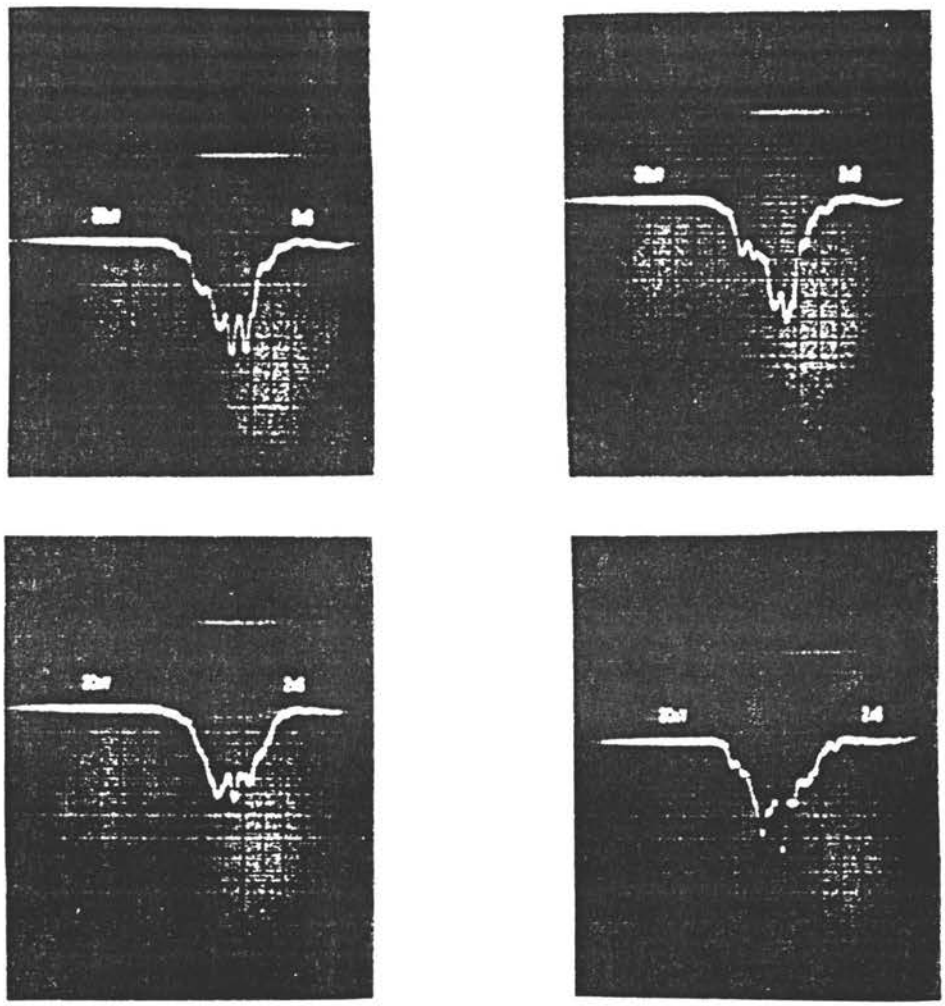

Fig. 3.13. Time evolution of several individual dye laser pulses

In spite of these spikes, we have chosen to model the time evolution with a Gaussian function

$$I(t) = I_0 \exp\left[-\frac{\ln(2)}{\delta t^2} t^2\right], \tag{3.4}$$

where δt stands for the measured HWHM of δt = 3nsec ± 30%. Integrating over this time evolution we relate the peak intensity in space and time I_0 to the maximum spatial energy density ED_0

$$I_0 = \left[\frac{\ln(2)}{\pi}\right]^{0.5} \frac{ED_0}{\delta t} = 8\ 10^{15}\ W/m^2 \pm 55\%, \tag{3.5a}$$

or directly to the measured parameters

$$I_0 = \frac{2}{\pi}\left(\frac{\ln(2)}{\pi}\right)^{0.5}\frac{E}{\delta t}\left[\frac{z_2-f}{w_{02}f}\right]^2 = 8\text{GW/mm}^2 \pm 55\%. \qquad (3.5b)$$

Due to the large accumulative error of this measurement, we will use the value for the peak intensity only as an order of magnitude estimate.

3.2.2.2 SRS Spectra

To calculate Stark broadened SRS spectra we have to adapt Eq. (2.135) to our experimental situation. The peak power of the pulsed dye laser is some seven orders of magnitude larger than the power of the Ar^+ laser. Its electrical field is therefore the only source of the optical Stark effect. Our detection system integrates the signal over the duration of each pulse, yielding the SRS energy per pulse; therefore we have to include an integration over the time evolution of the pulsed laser into our theoretical results. The length of the interaction region in cell one ($l \approx 10$cm) is about 200 times larger than the Rayleigh length ($z_0 \approx 0.36$mm); the limits of integration z_1, z_2 can therefore be approximated by $-\infty$ and $+\infty$, respectively. Taking all of the above into account and neglecting proportionality constants, which do not influence the lineshape we may rewrite Eq. (2.135) as

$$\Delta E \sim \int_{-\infty}^{\infty} dt\, e^{-at^2} \int_{-\infty}^{\infty} dz \int_{0}^{\infty} dr\, \chi''\, G_I^2, \qquad (3.6)$$

where ΔE is the energy of the SRS signal generated by one laser pulse, e^{-at^2} is the Gaussian approximation of the time evolution of the dye

laser intensity, with $a = \ln(2)/\delta t^2$ and δt = 3nsec being the HWHM; χ'' is the imaginary part of the third order nonlinear susceptibility and G_I the spatial intensity distribution in a Gaussian beam (Eq. (2.126a)). Due to the Stark effect χ'' becomes a function of the Stark coefficient β and the local intensity, which is a function of the coordinates t, z, r. Furthermore we have to sum over the contributions of the individual rotational levels (quantum number l) and their orientational sublevels (quantum number m), which have individual Stark coefficients $\beta^{v,\,l,\,m}_{v',l',m'}$. These coefficients together with the corresponding transition strengths $Fs^{0,1,m}_{1,1,m}$ are listed for some Q-branch lines of N_2 in table 2.3. We write the Lorentzian part of χ'' for the Q-branch as (Eq. (2.136))

$$\chi''_L(\Delta\omega) = B \sum_{l=0,\infty} \sum_{m=0,1} Fs^{0,1,m}_{1,1,m} \frac{\gamma}{(\Delta\omega + \beta^{0,1,m}_{1,1,m} I(t,z,r))^2 + \gamma^2}, \qquad (3.7a)$$

where B is a constant (Eq. (2.98b)), $\Delta\omega$ has been defined as $\Delta\omega = \Delta - \omega = \Delta - (\omega_2 - \omega_1)$ (Eq. (2.103)), and the pump intensity I, which induces the Stark shift βI, may be written as

$$I(t,z,r) = I_0\, e^{-at^2}\, G_I(z,r). \qquad (3.7b)$$

To obtain χ'' including Doppler broadening and laser linewidth, we convolute χ''_L with the respective Doppler and laser lineshapes G (Eq. (2.105)) and P (Eq. (3.1)), as described in section 2.2.2

$$\chi'' = \chi''_L * G * P. \qquad (3.8)$$

We have used Eq.'s (3.6) through (3.8) to calculate Stark broadened SRS line shapes for the l = 4 vibrational transition in the Q-branch of N_2 for various peak intensities I_0. The summation over l has proven to be unnecessary in these calculations, since compared to the Stark

broadening the influence of neighboring lines turned out to be negligible. Results ,with the maximum signal normalized to one, are shown in Fig. (3.14) for peak intensities between 0 and 16GW/mm^2.

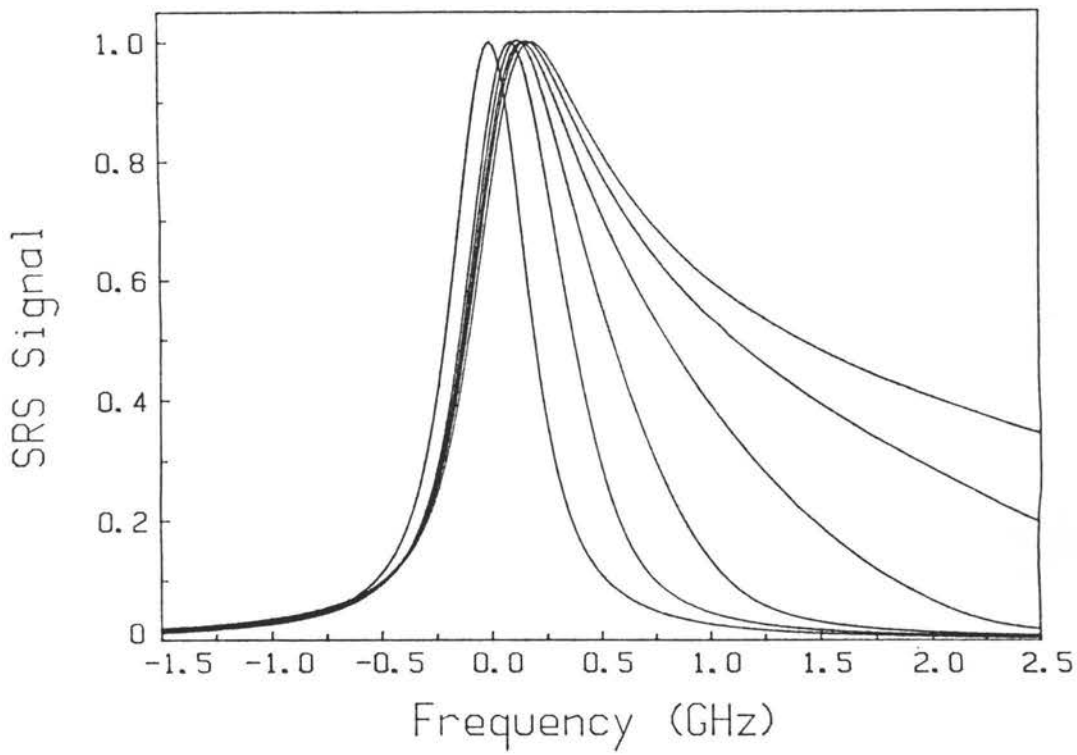

Fig. 3.14. Theoretical SRS spectra of the 1 = 4 vibrational Q-branch transition (v=0 → v=1) in molecular nitrogen for peak intensities of I_0 = 0, 1, 2, 4, 8, and 16 GW/mm^2, plotted as a function of $\Delta\omega$

We note that at a fairly low peak intensity (I_0 = 1GW/mm^2) the spectral peak is shifted and the line somewhat broadened towards higher frequency (smaller Raman shift). At higher intensities the peak shift increases only minimally, while the asymmetric broadening

significantly changes the line shape and linewidth. A qualitative explanation of this result may be found in the fact that at high intensities, the signal generated close to the origin (t,z,r = 0) is spread in frequency due to the large range of Stark shifts. The spectral peak is therefore still due to the nearly unshifted signal, generated away from the origin in time and space (r,z,t = 0) at fairly small intensities. This leads to small peak shifts together with a strong asymmetric broadening of the wings.

An experimental IRS spectrum of the 1 = 4 vibrational Q-branch transition in nitrogen (9/Sept/86, 17:01:39), which shows substantial Stark broadening, together with a theoretical calculation is shown in Fig. (3.15a). To overlay theoretical and experimental curves, we have fitted only peak intensity, signal strength and zero offset of the signal. This fitting procedure has led to a peak intensity of $4.8GW/mm^2$, well within the limits given by section 3.2.2.1 ($8GW/mm^2 \pm 55\%$). The common frequency scale for theory and experiment has not been adjusted; it is simply that of the non-Stark broadened spectrum from a subsequent measurement (9/Sept/86, 17:30:36). We have chosen the peak of the theoretical fit to this non-Stark broadened spectrum as the zero of our frequency scales for 1 = 4 (Fig. (3.9a)). As described in section 3.2, we use the respective Fabry-Perot spectra to define relative linear frequency scales for both spectra. Then we overlay the multitude of iodine hyperfine lines (Fig. (3.7c)) of one scan with those of the other scan. This way we transfer the zero of the frequency scale from the non-Stark broadened to the Stark broadened spectrum.

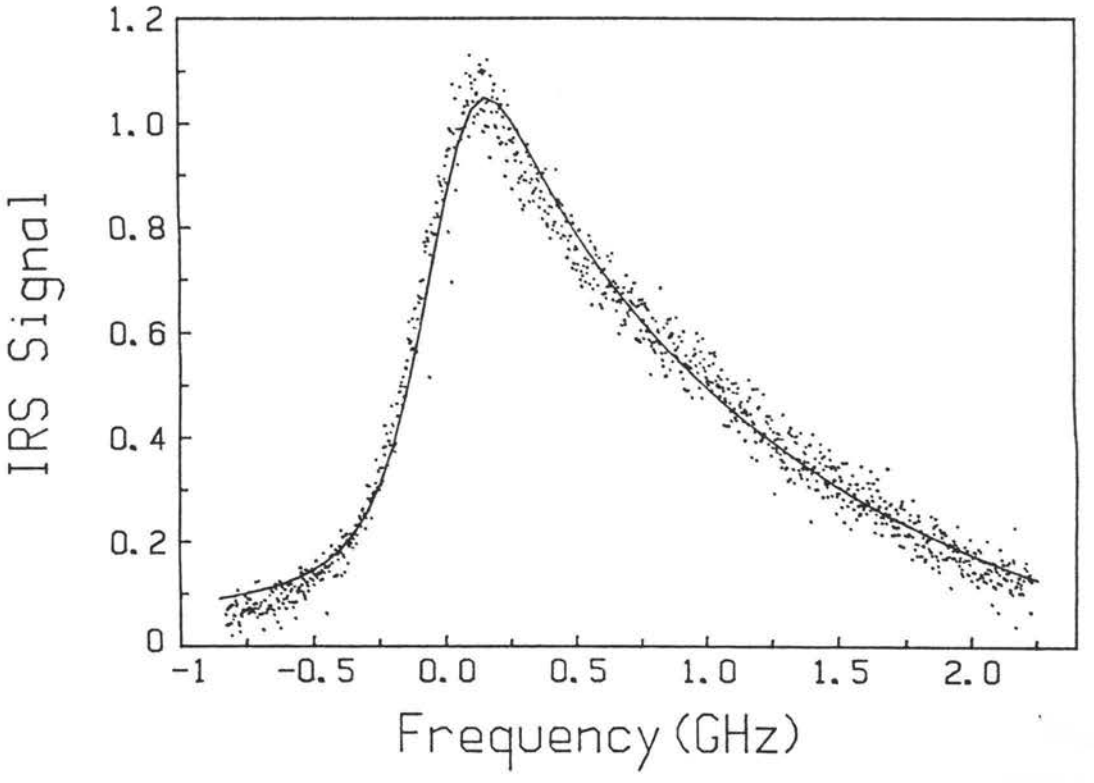

Fig. 3.15a. Comparison between theoretical (solid curve, I_0 = 4.8GW/mm^2) and experimental (dots) Stark broadened IRS spectra of the l=4 vibrational Q-branch transition (v=0 → v=1) in molecular nitrogen (N_2), plotted as a function of $\Delta\omega$; i.e. with the dye laser scanned towards higher frequency (smaller Raman shift)

A comparison with the theory therefore evaluates not only the prediction of the line shape for the Stark broadened spectra, but also the prediction of the shift between non-Stark broadened and Stark broadened SRS spectra. Figure (3.15a) shows good agreement between theory and experiment. Minor disagreements in the line shape are probably due to the imperfect assumption of identical Gaussian profiles for pump and probe laser and the rather crude approximation of a Gaussian time evolution of the pump laser intensity. In particular one could imagine to calculate the theory with a lower peak intensity, which would shift the peak and the positive slope of the calculation to the left and yield better agreement in this part of the spectrum. This change would also lower the theoretical signal in the right part of the spectrum, leading to a severe disagreement with the experiment. This problem could possibly be resolved by including the the high intensity spikes (in time) of the pulsed laser into the calculation. These spikes would increase the signal for large Stark shifts, while leaving the left part of the spectrum unchanged. So much for a possible qualitative explanation of the small discrepancies. Due to insufficient knowledge about the random nature of the time evolution of the dye laser pulses, we have not attempted a quantitative calculation of this effect. Figure (3.15b) shows the experimental result together with calculated spectra corresponding to peak intensities of 4.0, 4.8 and 5.5 GW/mm^2. We note that a change of about 15% in peak intensity corresponds to a noticeable change in line shape.

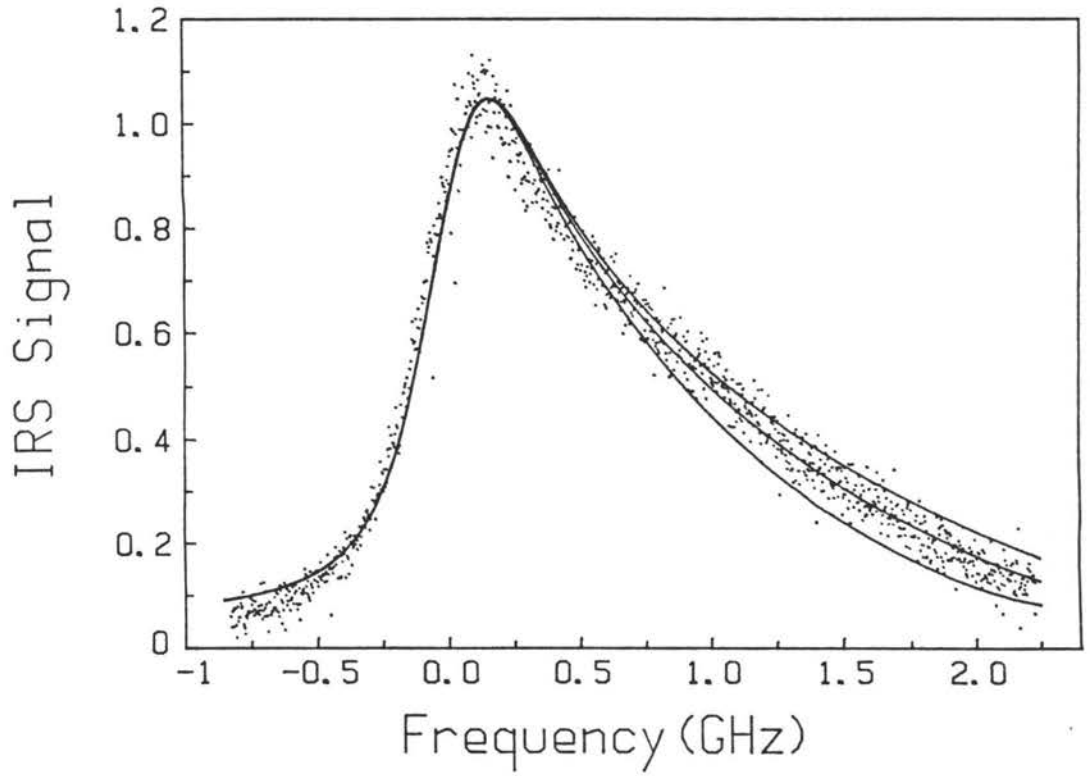

Fig. 3.15b. Comparison between theoretical (solid curves, I_0 = 4.0, 4.8, and 5.5GW/mm^2) and experimental (dots) Stark broadened IRS spectra of the l=4 vibrational Q-branch transition (v=0 → v=1) in molecular nitrogen (N_2), plotted as a function of $\Delta\omega$; i.e. with the dye laser scanned towards higher frequency (smaller Raman shift)

To directly compare non-Stark broadened and Stark broadened IRS spectra of l = 4 we have applied a 25-point smoothing routine [3.10] to the data in Fig. (3.9a) (9/Sept/86, 17:30:36) and in Fig. (3.15a) (9/Sept/86, 17:01:39). The resulting experimental IRS spectra are both shown in Fig. (3.15c).

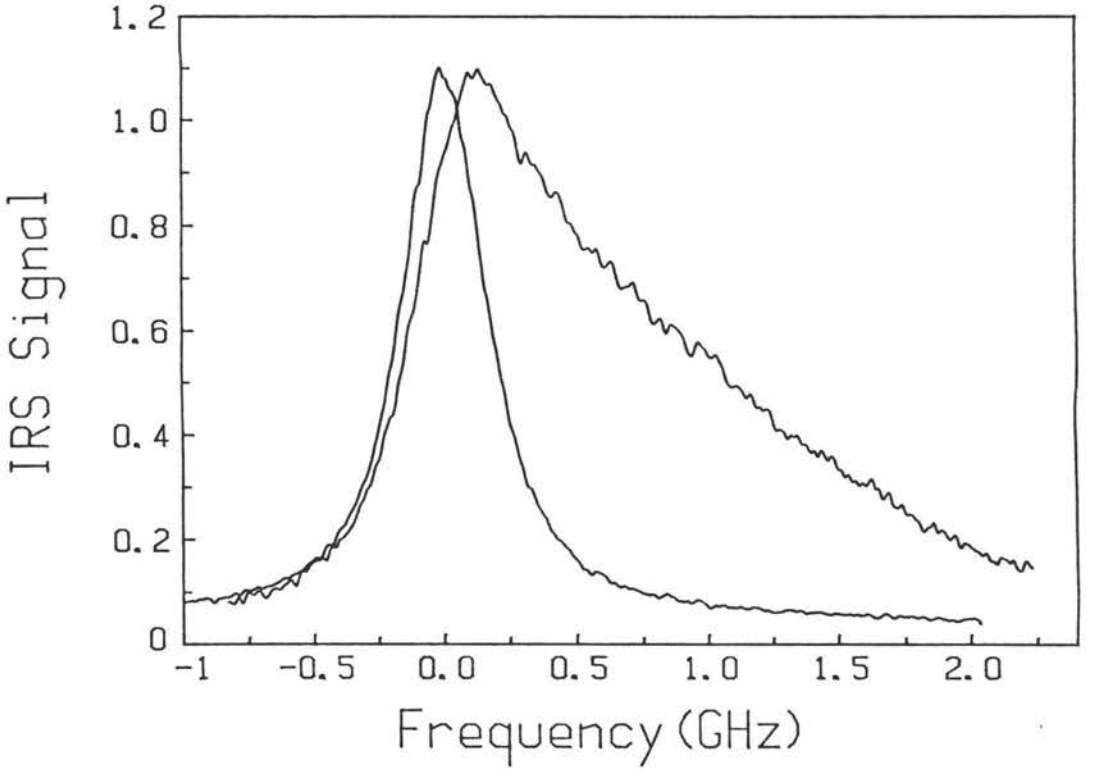

Fig. 3.15c. Comparison between non-Stark broadened and Stark broadened experimental IRS spectra of the l=4 vibrational Q-branch transition (v=0 → v=1) in N_2, plotted as a function of $\Delta\omega$

One recognizes directly the major influence of the Stark effect on line shape and peak position. The Stark broadened IRS spectrum was taken with cell one filled with 10kPa of nitrogen and cell two

evacuated, while we have reversed this situation to record the non-Stark broadened IRS spectrum. Due to the fact that we have left all other experimental parameter unchanged, Fig. (3.15c) represents a rather direct comparison between Stark broadened and non-Stark broadened IRS spectra. Figure (3.15d) shows the same comparison for the theoretically calculated SRS spectra.

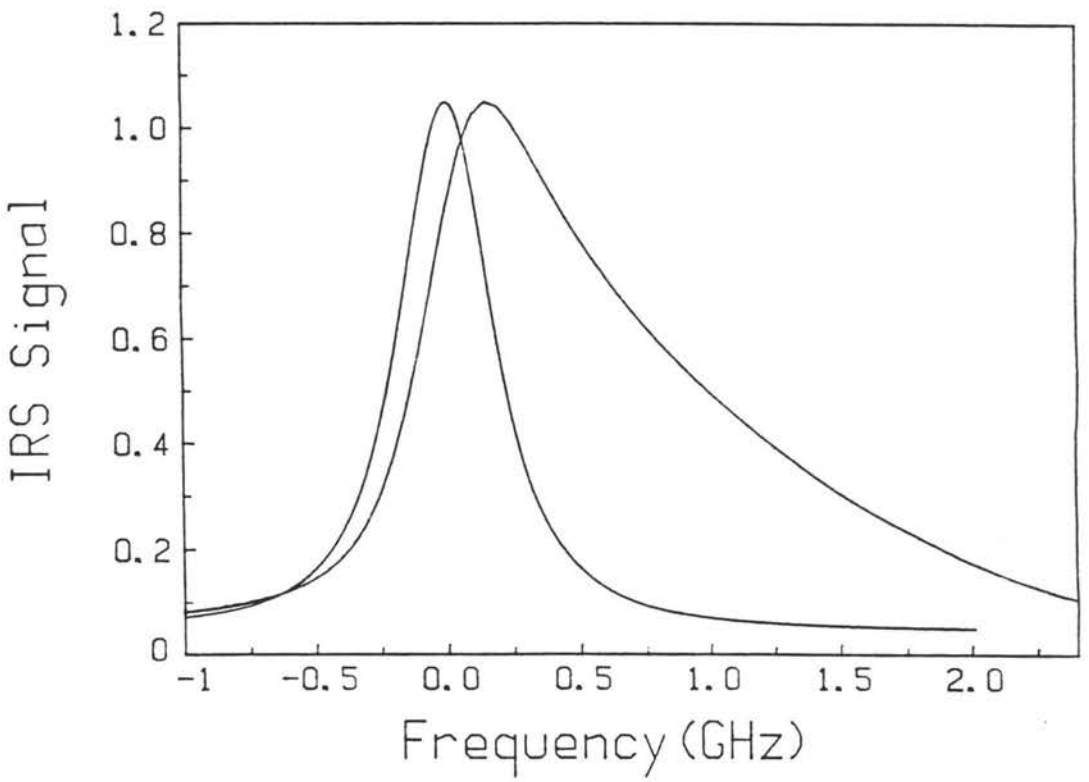

Fig. 3.15d. Comparison between non-Stark broadened and Stark broadened (I_0 = 4.8GW/mm^2) theoretical IRS spectra of the l=4 vibrational Q-branch transition (v=0 → v=1) in N_2, plotted as a function of $\Delta\omega$

The same analysis was performed for a scan of the l = 12 vibrational Q-branch transition in molecular nitrogen (7/Oct/86, 20:01:43). In this case the calculations become a little more tedious, because we sum over 13 non-degenerate m-sublevels instead of only 5 as in the previous calculation for l = 4. Figure (3.16a) shows the comparison between experiment and theory, with a theoretical peak intensity of $I_0 = 6.8 GW/mm^2$.

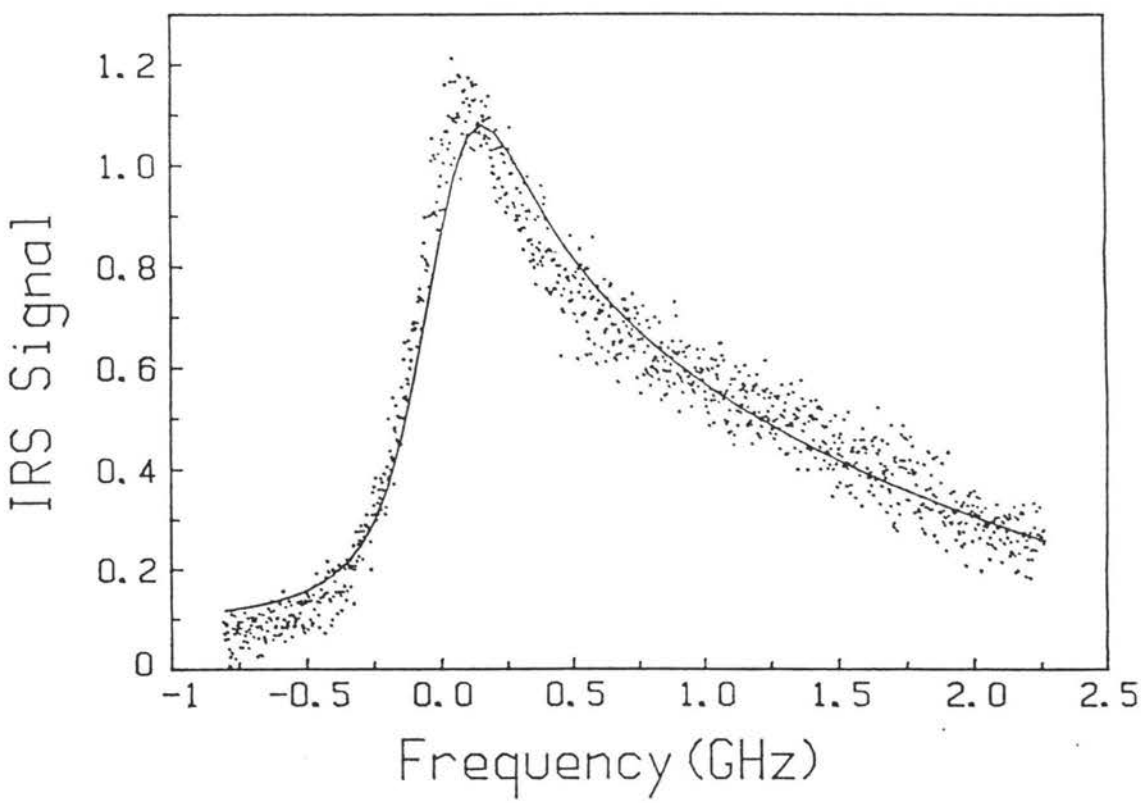

Fig. 3.16a. Comparison between theoretical (solid curve, $_0I$ = $6.8 GW/mm^2$) and experimental (dots) Stark broadened IRS spectra of the l=12 vibrational Q-branch transition (v=0 → v=1) in N_2, plotted as a function of $\Delta\omega$

We note good agreement between experiment and theory. The minor discrepancies are very similar to those of l = 4. Figure (3.16b) gives a comparison between non-Stark broadened (7/Oct/86, 19:29:58) and Stark broadened (7/Oct/86, 20:01:43) experimental spectra after use of a 25-point smoothing routine [3.10].

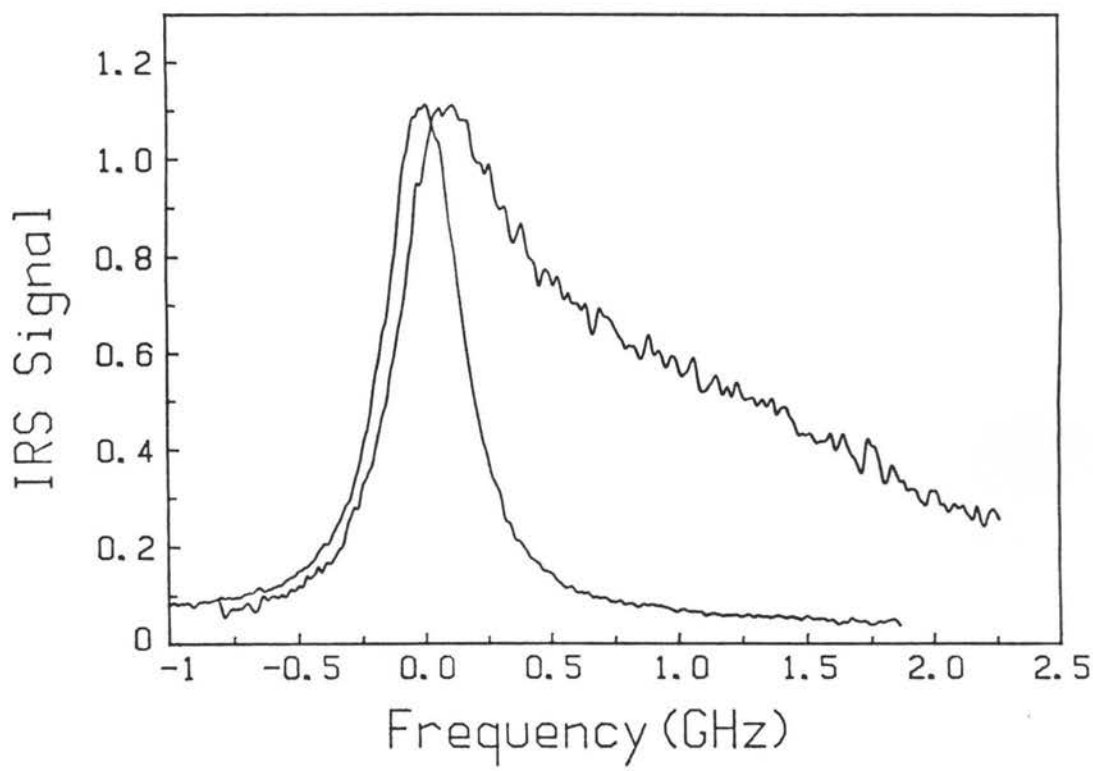

Fig. 3.16b. Comparison between non-Stark broadened and Stark broadened experimental IRS spectra of the l=12 vibrational Q-branch transition (v=0 → v=1) in N_2, plotted as a function of $\Delta\omega$

Figure (3.16c) shows the same comparison for the theoretical calculations for l = 12.

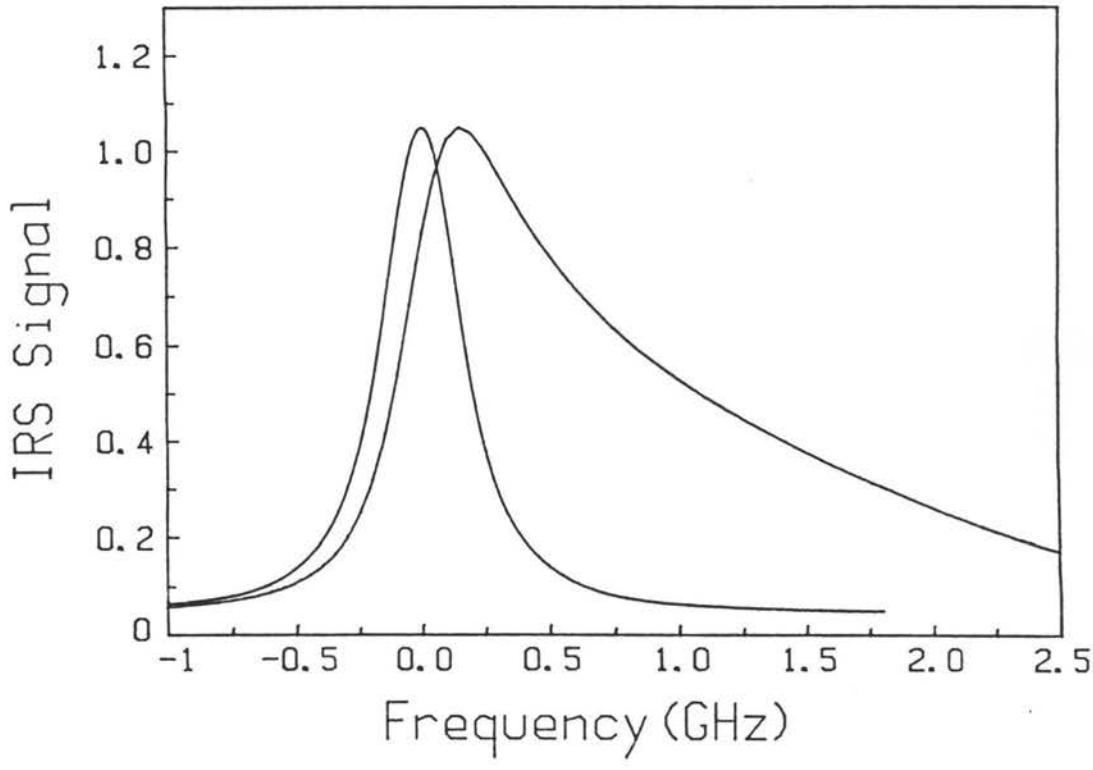

Fig. 3.16c. Comparison between non-Stark broadened and Stark broadened (I_0 = 6.8GW/mm^2) theoretical IRS spectra of the l=12 vibrational Q-branch transition (v=0 → v=1) in N_2, plotted as a function of $\Delta\omega$

3.2.2.3 FWMRS Spectra

To calculate Stark broadened FWMRS spectra we follow similar procedures as for SRS (Sect. 3.2.2.2). Equation (2.143) is adapted to the experimental situation by making the pump laser intensity a Gaussian function of time, corresponding to a pulsed pump laser. Furthermore we integrate the whole expression over time, which corresponds to a detection scheme which is non-time resolved for any single laser pulse, detecting the total emitted energy per pulse. Neglecting all constants which do not influence the line shape we rewrite Eq. (2.143) as

$$E \sim \int_{-\infty}^{+\infty} dt\, e^{-2at^2} \int_0^{\infty} dx \left| \int_{-\infty}^{+\infty} dz\, e^{i\frac{xz}{4}} \frac{e^{-i\tan^{-1}z}}{(1+z^2)^{3/2}} \int_0^{\infty} dr\, r\chi J_0(x^{\frac{1}{2}}r) e^{r^2\left[\frac{iz-3}{1+z^2}\right]} \right|^2 , \quad (3.9a)$$

where e^{-at^2} is the Gaussian approximation of the time evolution of the dye laser intensity, with $a = \ln(2)/\delta t^2$ and δt = 3nsec being the HWHM. Taking advantage of symmetries in z and t, we rewrite Eq. (3.9a) as

$$E(\Delta\omega) \sim \int_0^{\infty} dt\, e^{-2at^2} \int_0^{\infty} dx \cdot \left| \int_0^{\infty} \frac{dz}{(1+z^2)^2} \int_0^{\infty} dr \frac{\chi(\Delta\omega, I) r J_0(x^{\frac{1}{2}}r)}{\exp\left[\frac{3r^2}{1+z^2}\right]} \left[\cos\left[\frac{xz}{4} + \frac{zr^2}{1+z^2}\right] + z\sin\left[\frac{xz}{4} + \frac{zr^2}{1+z^2}\right] \right] \right|^2 , \quad (3.9b)$$

where everything but the third order nonlinear susceptibility $\chi(\Delta\omega, I)$ is real.

The numerical evaluation of this formula is fairly involved and its basic principles will be described in the following. We note that

the integrand in Eq. (3.9b) may be split up into two factors. A real function of r, z and x which can be written as

$$f(r,z,x) = \exp\left(\frac{-3r^2}{1+z^2}\right) \frac{rJ_0(x^{\frac{1}{2}}r)}{(1+z^2)^2} \left[\cos\left(\frac{xz}{4}+\frac{zr^2}{1+z^2}\right) + z\sin\left(\frac{xz}{4}+\frac{zr^2}{1+z^2}\right)\right], \quad (3.10a)$$

and the complex third order nonlinear susceptibility $\chi(\Delta\omega,I)$, a function of detuning $\Delta\omega$ and local intensity $I(r,z,t)$, which can be calculated from Eq.'s (3.7, 3.8) by replacing the imaginary part of the Lorentzian with the complete complex Lorentzian. Equation (3.9b) may now be rewritten as

$$E(\Delta\omega) \sim \int_0^\infty dt\ e^{-2at^2}\ P(\Delta\omega,I_t) \quad (3.10b)$$

with $I_t = I_0 e^{-at^2}$. We change the variable of integration from t to I_t and obtain

$$E(\Delta\omega,I_0) \sim \int_0^{I_0} dI_t \frac{I_t}{(-a\ln(I_t/I_0))^{0.5}}\ P(\Delta\omega,I_t), \quad (3.10c)$$

$$\text{with}\quad P(\Delta\omega,I_t) = \int_0^X dx \left| \int_0^Z dz \int_0^R dr\ f(r,z,x)\ \chi(I_t,\Delta\omega) \right|^2, \quad (3.10d)$$

where X, R, Z are the upper limits for the numerical integration. A priori it is unclear how to choose these limits and the number of evaluation points in each dimension. We have solved this problem rather pragmatically by increasing the limits and the number of evaluation points until the calculated spectra converge to their final form. This has lead to X = 20, Z = 20, R = 10, and 50 evaluation points in each dimension. For these values we estimate the remaining error for any $\Delta\omega$ to be less than 1% of the maximum signal. First we

evaluate the generated power $P(\Delta\omega,I_t)$ on an equidistant two dimensional grid for different detunings $\Delta\omega$ (72 points, 50MHz spacing) and maximum spatial intensities I_t (51 points, 0.1 GW/mm^2 spacing). The rather complicated function f(r,z,x) is independent of $\Delta\omega$ and I_t and does not have to be re-evaluated for different positions on the grid. One part of f(r,z,x) is a Bessel function J_0, which is calculated by an approximation with rational functions or polynomials, depending on the size of its argument [3.15]. The third order nonlinear susceptibility $\chi(\Delta\omega,I=0)$, including the appropriate pressure, Doppler and laser broadening (Eq. (3.8)), is first stored in a one dimensional look up table. Then we use the complex form of Eq. (3.7a) to calculate a two dimensional array of χ for 3672 different combinations of $\Delta\omega$ and I, values between these points will be evaluated by linear interpolation. The summation over the rotational quantum number l (Eq. (3.7a)) is terminated at l = 8 for the calculation of the spectrum for l = 4, including all neighboring resonances within ±30GHz. Finally we use a closed Newton-Cotes formula, the extended trapezoidal rule [3.15], for the three dimensional integration, calculating 3672 values of $P(\Delta\omega,I_t)$ for the different combinations of $\Delta\omega$ and I_t. Using Microsoft Fortran V4.01 on an 16 MHz Intel 80386 based personal computer with a 80387 numerical coprocessor, this calculation takes roughly 10 hours of computer time, i.e. about 10 seconds per three dimensional integration. Now we may calculate the final spectra rather easily via Eq. (3.10c). To avoid the weak singularity at $I_t = 0$ we use the extended midpoint rule,

which is based on the second Euler-Mclaurin summation formula [3.15], for the final integration.

Results ,with the maximum FWMRS signal normalized to one, are shown in Fig. (3.17) for peak intensities between 0 and 4GW/mm^2.

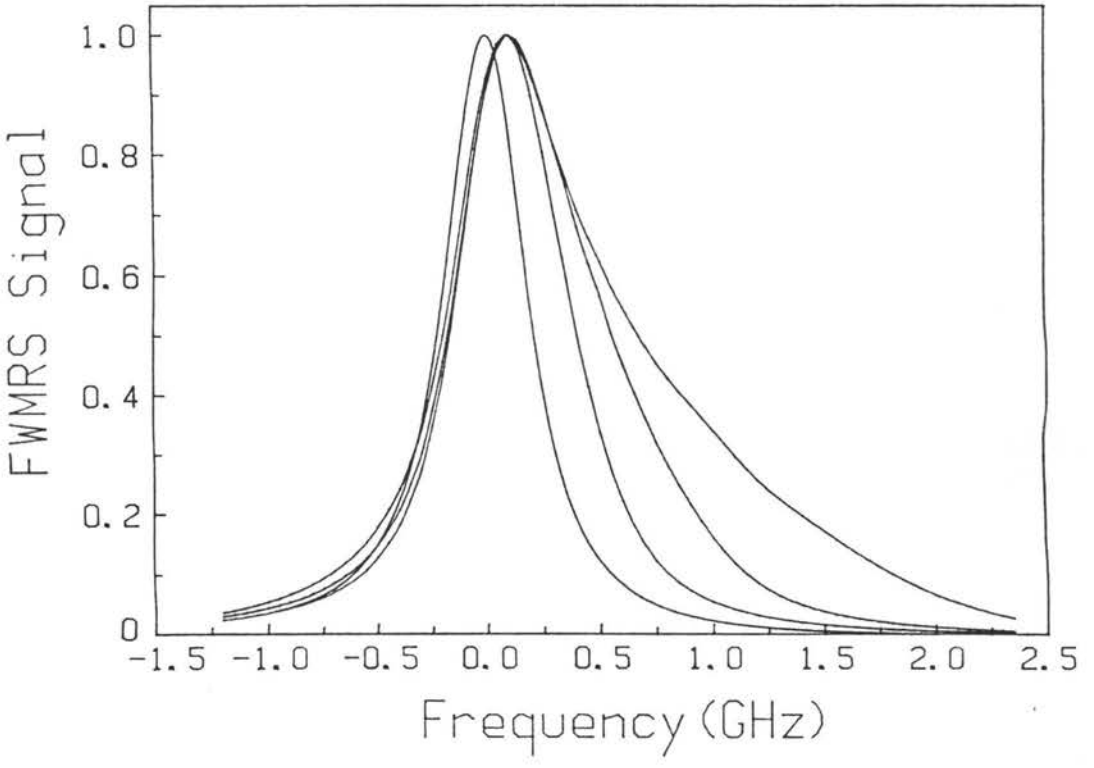

Fig. 3.17. Theoretical FWMRS spectra of the l = 4 vibrational Q-branch transition (v=0 → v=1) in molecular nitrogen for peak intensities of I_0 = 0, 1, 2, 4 GW/mm^2, plotted as a function of $\Delta\omega$

We note that the main peak shift takes place at a relatively low peak intensity (I_0 < 1GW/mm^2). For higher peak intensities I_0 the line shape becomes more asymmetric, but no further shift of the spectral

peak is observed. Figure (3.18a) shows a comparison between simultaneously recorded Stark broadened CSRS and IRS spectra of the 1 = 4 vibrational Q-branch transition in nitrogen (9/Sept/86, 17:01:39, 25-point smoothing). We note that the peak of the CSRS spectrum is narrower and shows less Stark shift than the peak of the IRS spectrum.

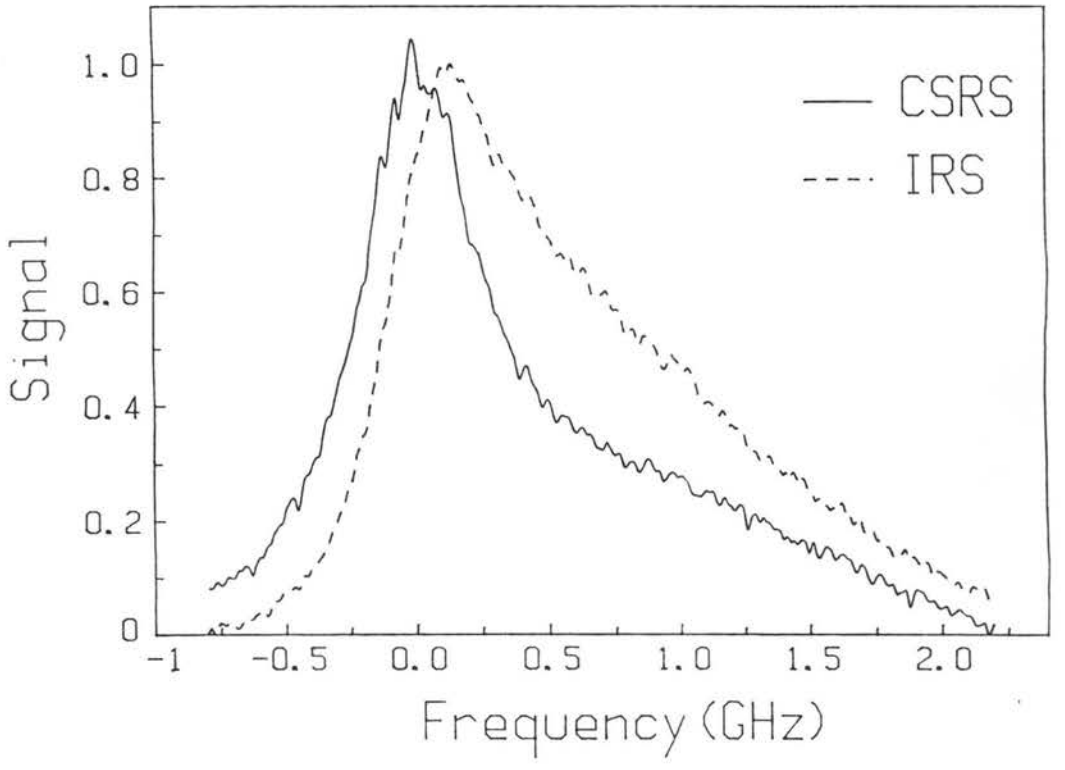

Fig. 3.18a. Comparison between experimental Stark broadened CSRS (solid curve) and SRS (dashed curve) spectra of the 1=4 vibrational Q-branch transition (v=0 → v=1) in molecular nitrogen, plotted as a function of $\Delta\omega$; i.e. with the dye laser scanned towards higher frequency (smaller Raman shift)

Furthermore the line shape of the CSRS spectrum shows a characteristic kink around $\Delta\omega$ = 0.3GHz. These characteristic features have been repetitively observed in many (≈20) individual spectra taken on several different days. The IRS spectrum has previously been successfully fitted with a theoretical spectrum corresponding to a peak intensity of $I_0 = 4.8 GW/mm^2$ (Sec. 3.2.2.2). We compare this theoretical calculation with a calculation of the CSRS spectrum for the same peak intensity (Fig. (3.18b)).

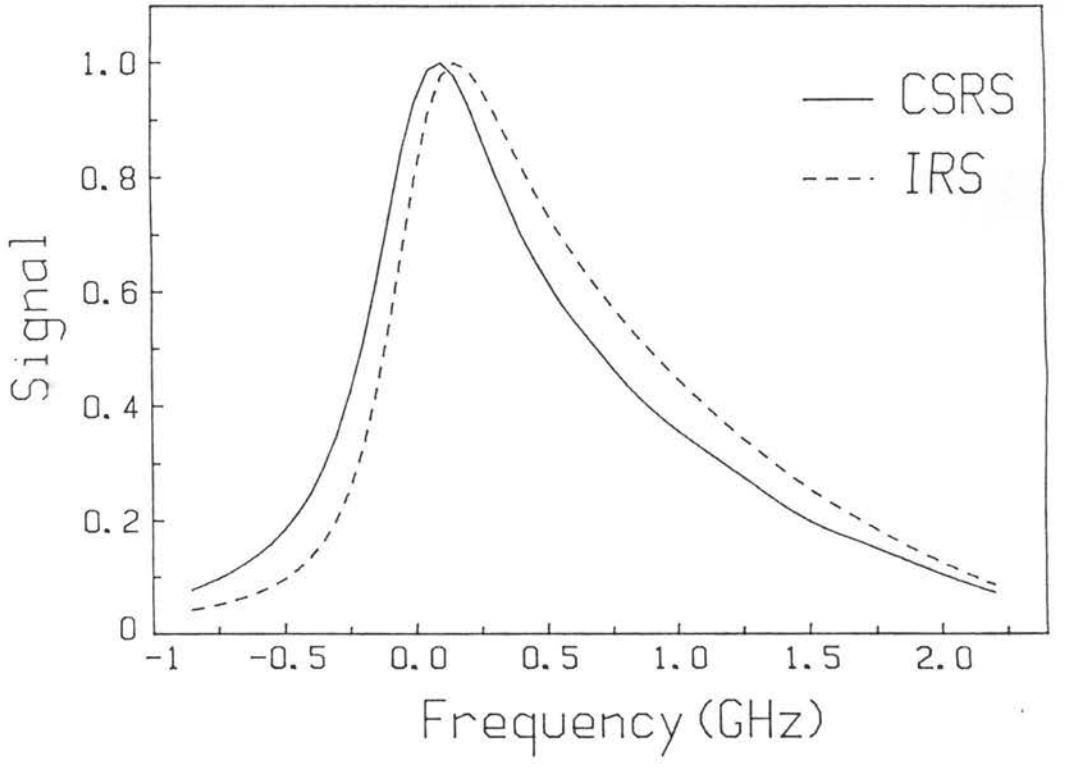

Fig. 3.18b. Comparison between theoretical Stark broadened CSRS (solid curve) and SRS (dashed curve) spectra of the 1=4 vibrational Q-branch transition (v=0 → v=1) in molecular nitrogen, plotted as a function of $\Delta\omega$

The CSRS theory reproduces some of the experimental features, it shows less Stark shift and is somewhat narrower than the theoretical IRS spectrum. However, it does not reproduce the characteristic CSRS line shape as seen in Fig. (3.18a). A direct comparison between the experimental (dots) and the theoretical (solid line) CSRS spectrum is shown in Fig. (3.18c). As for IRS (Sec. 3.2.2.2), peak hight and zero offset are adjusted, while the common frequency scale has been experimentally determined.

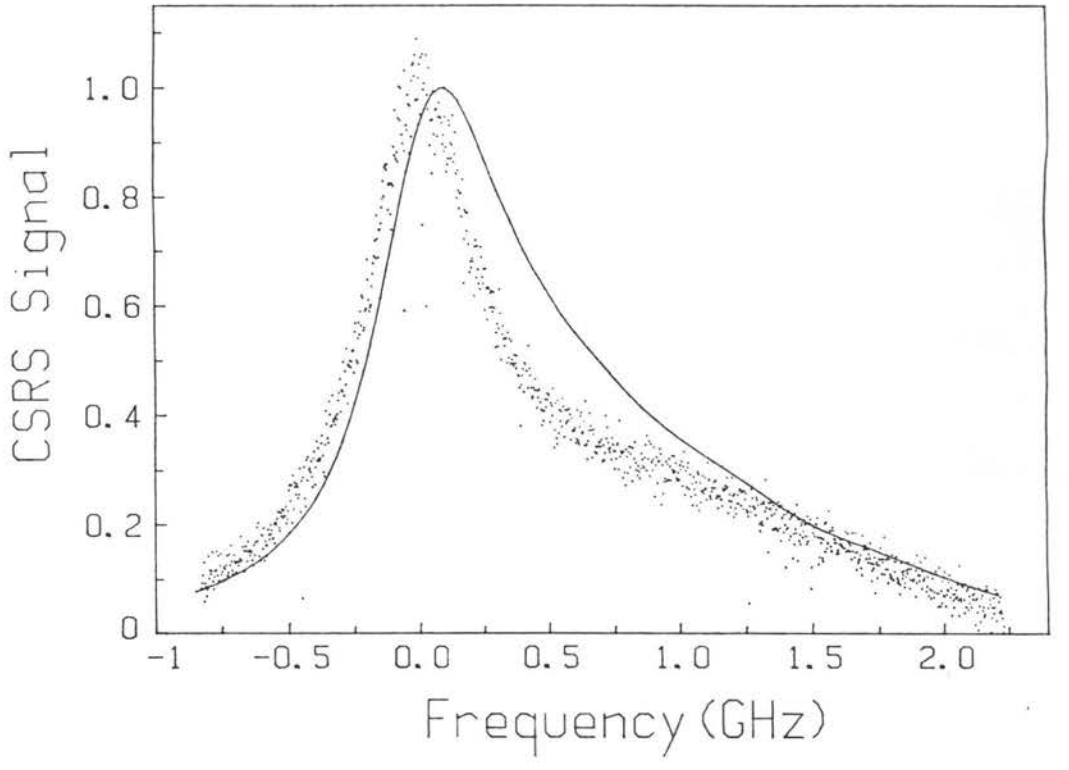

Fig. 3.18c. Comparison between theoretical (solid curve, I_0 = 4.8GW/mm^2) and experimental (dots) CSRS spectra of the l=4 vibrational Q-branch transition (v=0 → v=1) in molecular nitrogen, plotted as a function of $\Delta\omega$

The experimental peak is narrower and and shows less Stark shift than the theoretical peak. Furthermore the theory does not reproduce the characteristic kink mentioned earlier. Figure (3.18d) compares a Stark broadened (17:01:39, 9-Sept-86) with a non-Stark broadened CSRS spectrum (17:30:36, 9-Sept-86). We see, in comparison with the same figure for SRS (Fig. (3.15c)), rather little peak shift, a small broadening of the main peak and the characteristic asymmetric wing with a definite kink on the high frequency side.

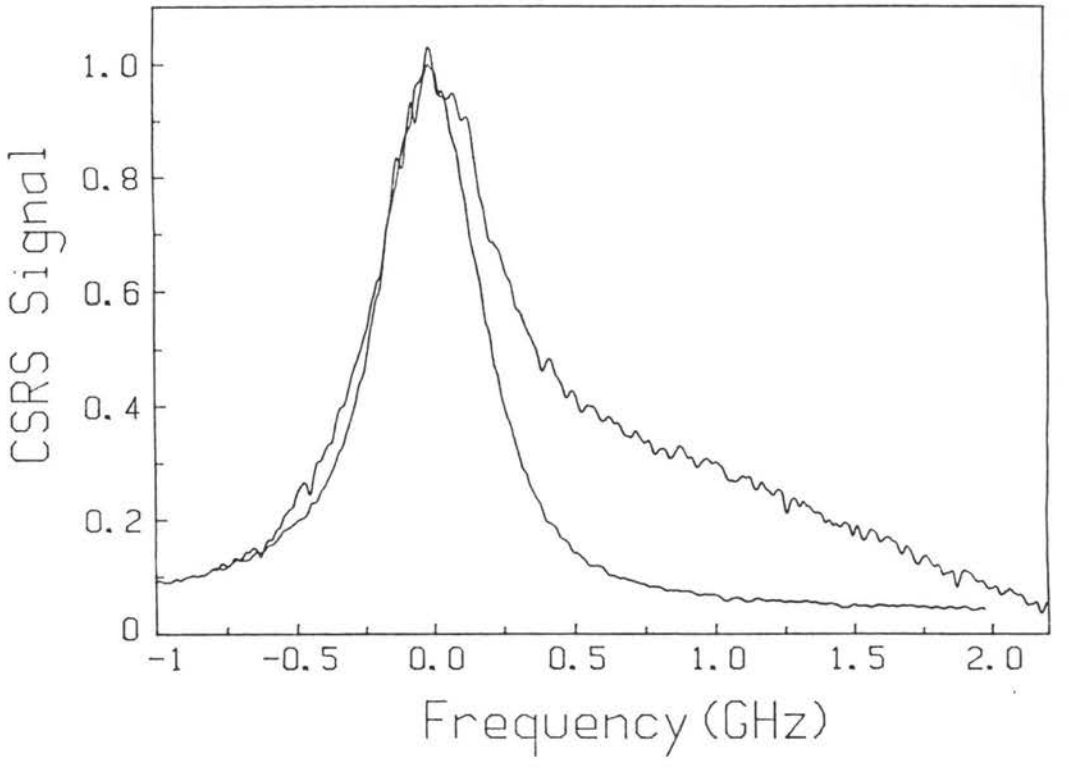

Fig. 3.18d. Comparison between non-Stark broadened and Stark broadened experimental CSRS spectra of the 1=4 vibrational Q-branch transition (v=0 → v=1) in molecular nitrogen, plotted as a function of $\Delta\omega$

The theoretical comparison (Fig. (3.18e), $I_0 = 4.8GW/mm^2$) clearly does not reproduce these experimental findings.

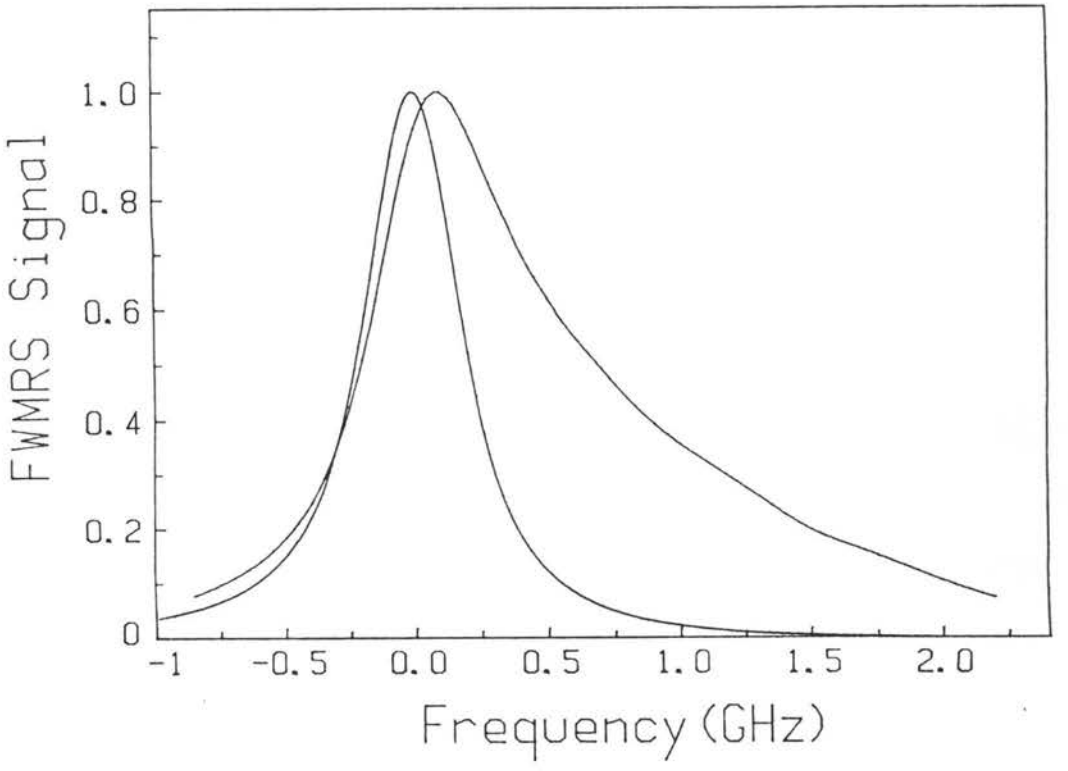

Fig. 3.18e. Comparison between non-Stark broadened and Stark broadened ($I_0 = 4.8GW/mm^2$) theoretical CSRS spectra of the l=4 vibrational Q-branch transition (v=0 → v=1) in molecular nitrogen, plotted as a function of $\Delta\omega$

While the reasons for the discrepancies between theoretical and experimental FWMRS spectra are not entirely clear, we will discuss two likely possibilities. The theoretical analysis assumes Gaussian laser beams, with an additional Gaussian time evolution for the pump laser intensity. Especially the pulsed pump laser beam deviated from this

ideal situation, as discussed in section 3.2.2.1. Whereas the SRS signal varies linearly with the pump laser intensities (Eq. (2.100)), the FWMRS signal is proportional to the square of the pump laser intensity (Eq. (2.102)); FWMRS spectra are therefore influenced more strongly by deviations from the ideal Gaussian beam and the spiking in time evolution than SRS spectra. The qualitative discussion of the minor discrepancies for SRS (Sec. 3.2.2.2) therefore also applies to FWMRS, resulting in larger discrepancies.

Furthermore we have to examine possible contributions of higher order processes, based on the fifth order nonlinear susceptibility $\chi^{(5)}$ to the FWMRS signal. Section 4.2 gives a theoretical account for a likely fifth order process; its inclusion leads to the following expression for the nonlinear susceptibility

$$\chi(\Delta\omega,I) = I(r,z,t)\ \chi^{(3)}\left[1 + A\ \frac{I(r,z,t)}{\Delta\omega - i\gamma}\right], \qquad (3.11)$$

with $\chi^{(5)} = A\ \frac{\chi^{(3)}}{\Delta\omega - i\gamma}$. Section 4.2 will give an order of magnitude estimate along with the relative sign for the constant A. In this section however, we will treat A as an adjustable parameter to fit our FWMRS as well as possible. Inserting the new expression for $\chi(\Delta\omega,I)$ (Eq. (3.11)) into Eq. (3.9) enables us to calculate theoretical FWMRS spectra for different values of A. Figure (3.19) shows FWMRS spectra for $l = 4$, a peak intensity I_0 of $4.8GW/mm^2$ and fifth order coefficients A of 0.0, 0.2 and $0.5mm^2/J$. Increasing the coefficient A shifts the spectral peak to a lower frequency $\Delta\omega$ and raises the high frequency wing.

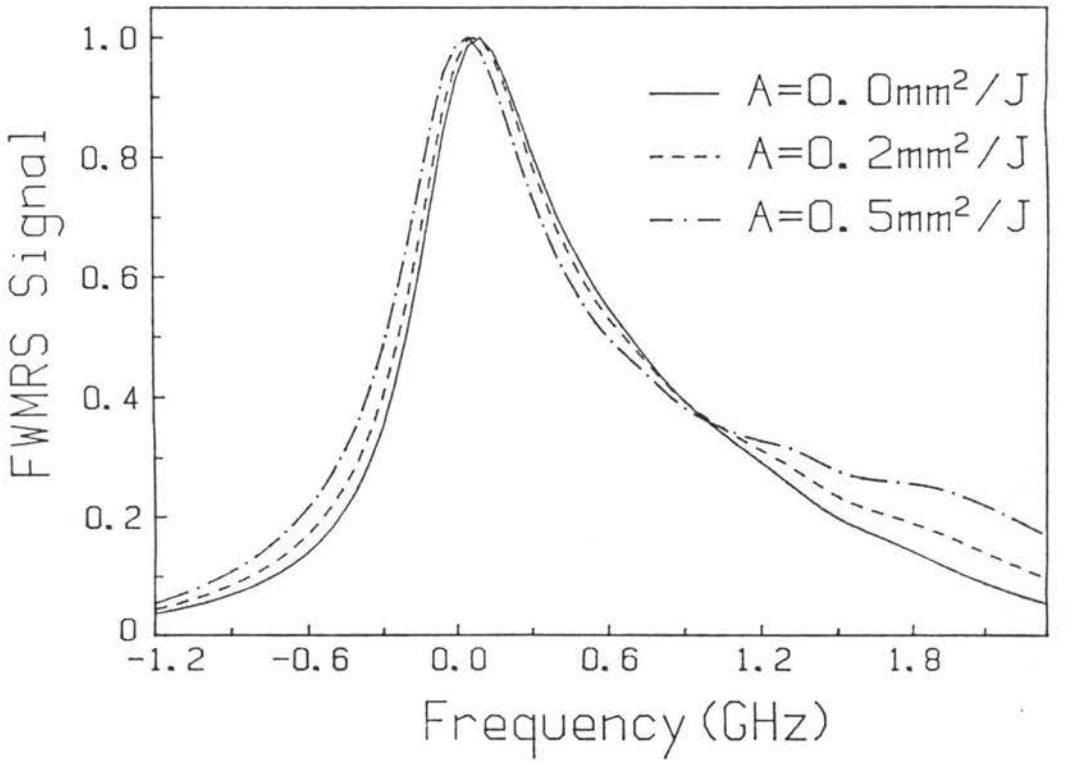

Fig. 3.19. Theoretical FWMRS spectra of the 1 = 4 vibrational Q-branch transition (v=0 → v=1) in molecular nitrogen for fifth order coefficients of A = 0.0, 0.2, 0.5 mm^2/J and a peak intensity of $4.8GW/mm^2$, plotted as a function of $\Delta\omega$

Adjusting the parameter A to achieve a good fit with the experimental spectrum plotted in Fig. (3.18c) (1 = 4, $I_0 = 4.8GW/mm^2$) leads to A = $0.3mm^2/J$ and to significantly improved agreement between experiment and theory (Fig. (3.20)), due to the additional $\chi^{(5)}$ term. While our experiment has not been designed to test the possible influence of higher order effects, its results never the less suggest that the fifth-order process leading to a fifth-order nonlinear susceptibility

$\chi^{(5)}$ (Sec. 4.2) may be important and should perhaps be included in the line shape theory for tightly focused high power laser beams. It will be necessary however, to investigate this possibility with a specifically designed experiment.

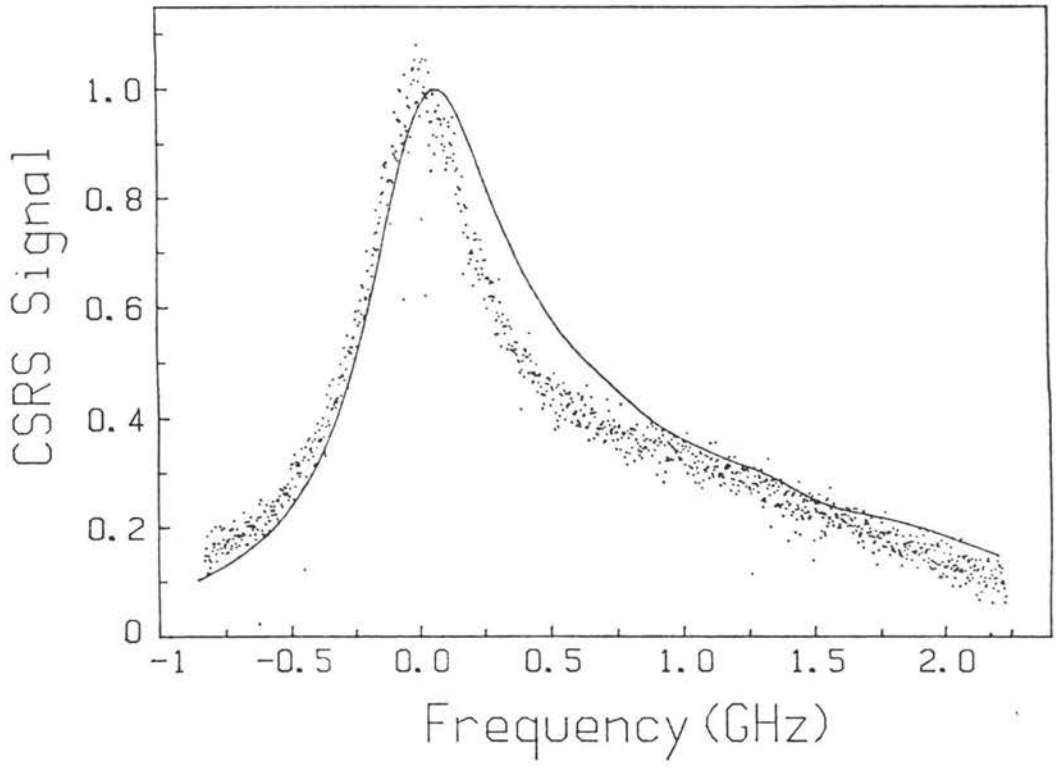

Fig. 3.20. Comparison between experimental (dots) and theoretical (solid curve, $I_0 = 4.8 GW/mm^2$, fifth order coeff. A = $0.3 mm^2/J$) CSRS spectra of the 1 = 4 vibrational Q-branch in molecular nitrogen, plotted as a function of $\Delta\omega$

References Chapter 3

3.1 G.C. Herring, S.A. Lee and C.Y. She, "Measurements of a Supersonic Velocity in a Nitrogen Flow Using Inverse Raman Spectroscopy," Opt. Lett. **8**, 214 (1984).

3.2 H. Moosmüller, G.C. Herring, and C.Y. She, "Two-Component Velocity Measurements in a Supersonic Nitrogen Jet with Spatially Resolved Inverse Raman Spectroscopy," Opt. Lett. **9**, 536 (1984).

3.3 G.C. Herring, "Coherent Raman Spectroscopy for Supersonic Flow Measurements," Ph.D. dissertation (Colorado State University, Fort Collins, Colorado, 1987).

3.4 F.V. Kovalski, R.T. Hawkins and A.L. Schawlow, "Digital Wavemeter for CW Lasers," J. Opt. Soc. Am. **66**, 965 (1976).

3.5 L. Hlousek, S.A. Lee, and W.M. Fairbank, Jr., "Precision Wavelength Measurements and New Experimental Lamb Shifts in Helium," Phys. Rev. Lett. **50**, 328 (1983).

3.6 T.W. Hänsch, M.D. Levenson and A.L. Schawlow, "Complete Hyperfine Structure of a Molecular Iodine Line," Phys. Rev. Lett. **26**, 946 (1971).

3.7 P. Drell and S. Chu, "A Megawatt Dye Laser Oscillator-Amplifier System for High Resolution Spectroscopy," Opt. Commun. **28**, 343 (1979).

3.8 G.C. Herring, NASA Langley Research Center, Hampton, Virginia (personal communication, 1984).

3.9 W. Demtröder, Laser Spectroscopy (Springer, Heidelberg, 1981), p.154.

3.10 P.R. Bevington, Data Reduction and Error Analysis for the Physical Sciences (McGraw-Hill, New York, 1969), p.255.

3.11 G.J. Rosasco, W. Lempert, W.S. Hurst, and A. Fein, "Pressure Dependent Line Width and Line Shift Measurements in the Vibrational Q-Branch of N_2 from 4 to 200kPa," in Proceedings of the Sixth International Conference on Spectral Line Shapes (Walter de Gruyter, Berlin, 1982).

3.12 K.P. Huber and G. Herzberg, Molecular Spectra and Molecular Structure IV, Constants of the Diatomic Molecules (Van Nostrand, New York, 1979), p.412.

3.13 C.Y. She, H. Moosmüller and G.C. Herring, "Coherent Light Scattering Spectroscopy for Supersonic Flow Measurements," Appl. Phys. **B45** (to be published).

3.14 W. Demtröder, Laser Spectroscopy (Springer, Heidelberg, 1981), p.268.

3.15 W.H. Press, B.P. Flannery, S.A. Teukolsky and W.T. Vetterling, Numerical Recipes: The Art of Scientific Computing (Cambridge University Press, Cambridge, 1986).

Chapter 4

Other Nonlinear Effects

4.1 Phase Modulation Induced by Rapid Stark Tuning of the Molecular Transition Frequency

In section 2.2.4 we have treated the Stark broadening in a quasi continuous manner, i.e. we have neglected effects due to the rapid Stark tuning of the molecular frequency by the pulsed laser. As it turns out the resulting effect averages out under our experimental conditions, which justifies our simplification. None-the-less we will discuss these effects, and specify the experimental conditions under which they should be observable.

We reduce the number of equations by assuming an experimental setup with one low power cw laser and one high power pulsed laser, which has a uniform intensity distribution and is the sole source of the molecular Stark effect; equations for different experimental situations may be derived easily. However, for an experimental setup using two pulsed lasers saturation effects and Rabi-flopping may become important. These effects have been discussed in a recent publication [4.1]. We start with the molecular equation of motion (Eq. (2.74)), which has been modified, by adding a Stark shift $\beta I(t)$ to the molecular resonance frequency Δ.

$$\frac{\partial^2 q}{\partial t^2} + 2\gamma \frac{\partial q}{\partial t} + [\Delta + \beta I(t)]^2 q = F(t) \qquad (4.1)$$

where I(t) is the time dependent intensity of the pulsed laser. The driving force given by Eq. (2.73) is modified by including a time dependent envelope for the electrical field to account for the pulsed laser.

$$F(t) = \frac{1}{4}\,\epsilon_0\alpha'\left[f(t)E_1^* E_2 e^{-i(\omega_2-\omega_1)t} + c.c.\right], \tag{4.2}$$

where E_n is the peak electrical field at the frequency ω_n and f(t) is the time evolution of the field amplitude of the pulsed laser, i.e. $f(t) = \left[\frac{I(t)}{I_{max}}\right]^{0.5}$. We substitute the Ansatz

$$q(t) = \frac{1}{2}\left[Q(t)\; e^{-\gamma t}\; e^{-i(\Delta^2-\gamma^2)^{0.5}t} + c.c.\right], \tag{4.3}$$

into Eq. (4.1) and obtain

$$\frac{\partial^2 Q}{\partial t^2} - 2i(\Delta^2-\gamma^2)^{\frac{1}{2}}\frac{\partial Q}{\partial t} + [2\Delta\beta I(t) + \beta^2 I^2(t)]\,Q = \tag{4.4a}$$

$$= \frac{1}{2}\epsilon_0\alpha' f(t)E_1^* E_2\; e^{\gamma t}\; e^{i(\Delta^2-\gamma^2)^{\frac{1}{2}}t}\; e^{-i\omega t}$$

with $\omega = \omega_2-\omega_1$. For most experimental conditions the Raman shift Δ is far larger than the Stark shift $\beta I(t)$ and the damping constant γ ($\gamma \ll \Delta$ and $\beta I \ll \Delta$). Furthermore we use the slowly varying amplitude approximation and neglect $\frac{\partial^2 Q}{\partial t^2}$. This simplifies Eq. (4.4a) to

$$\frac{\partial Q}{\partial t} + i\beta I(t)Q = \frac{i}{4\Delta}\epsilon_0\alpha' f(t)E_1^* E_2 e^{\gamma t} e^{i(\Delta-\omega)t}. \tag{4.4b}$$

Using the identity

$$\frac{\partial}{\partial t}\left[Q\,\exp\left(i\beta\int_{-\infty}^{t} I(t')dt'\right)\right] = \exp\left(i\beta\int_{-\infty}^{t} I(t')dt'\right)\left(\frac{\partial Q}{\partial t} + i\beta I(t)Q\right), \tag{4.5}$$

we solve Eq. (4.4b) and obtain

$$Q(t) = \tag{4.6a}$$

$$= \frac{i}{4\Delta}\epsilon_0\alpha' E_1^* E_2 \exp\left(-i\beta\int_{-\infty}^{t} I(t')dt'\right)\int_{-\infty}^{t} dt'' f(t'')e^{\gamma t''}e^{i(\Delta-\omega)t''}\exp\left(i\beta\int_{-\infty}^{t''} I(t')dt'\right),$$

where $Q(t)$ relates to the q_0 of Eq. (2.75) by

$$q_0(t) = e^{-\gamma t}e^{-i(\Delta-\omega)t}Q(t). \tag{4.6b}$$

If we set $\beta I(t) = 0$ and remove the time dependency ($f(t) = 1$, $I(t) = I$), Eq. (4.6) becomes identical with the previous solution (Eq. (2.76)). Based on Eq. (4.6) we define a time dependent third order nonlinear susceptibility as

$$\chi^{(3)}(t) = \frac{i\epsilon_0}{8\Delta}\left(\frac{1}{V}\sum_{m=1,n}\alpha_m'^2\right) f(t)\ e^{-\gamma t}\ e^{-i(\Delta-\omega)t}\cdot$$

$$\exp\left(-i\beta\int_{-\infty}^{t} I(t')dt'\right)\int_{-\infty}^{t} dt'' f(t'')e^{\gamma t''}e^{i(\Delta-\omega)t''}\exp\left(i\beta\int_{-\infty}^{t''} I(t')dt'\right), \tag{4.7a}$$

corresponding to the time-independent $\chi^{(3)}$ defined in Eq. (2.83a). Defining τ as $\tau = t - t''$, we may rewrite Eq. (4.7a) as

$$\chi^{(3)}(t) = iA\ f(t)\int_0^t d\tau\ f(t-\tau)e^{-\gamma\tau}e^{-i\Delta\omega\tau}\exp\left(-i\beta\int_{t-\tau}^{t} I(t')dt'\right), \tag{4.7b}$$

with $A = \frac{\epsilon_0}{8\Delta}\left(\frac{1}{V}\sum_{m=1,n}\alpha_m'^2\right)$ and $\Delta\omega = \Delta - \omega$.

For a sufficiently large damping constant γ, only small times τ contribute to $\chi^{(3)}$ and we may replace the integration $\int_{t-\tau}^{t} I(t')dt'$ by the simple multiplication $\tau I(t)$. Furthermore we use the slowly varying wave approximation to take $f(t-\tau)$ out of the integral, thus excluding Fourier transform broadening due to the finite width of the laser pulse. The analytical solution of the remaining integral yields

$$\chi^{(3)}(t) = \frac{A\ I(t)}{(\Delta\omega + \beta I(t)) - i\gamma} \tag{4.7c}$$

This approximation is identical to the treatment of the time dependence of the dye laser power in section 3.2.2.

First we use the exact solution for $\chi^{(3)}(t)$ (Eq. (4.7b)) to calculate undamped spectra ($\gamma = 0$) for different maximum Stark shifts βI_0. Then we examine spectra for different damping constants γ, and demonstrate that for an increasing damping constant γ, line shapes obtained with the exact expression for $\chi^{(3)}(t)$ (Eq. (4.7b)), converge towards those obtained with the approximate expression (Eq. (4.7c)). To calculate SRS and FWMRS spectra, we conveniently use the results of section 2.1, by replacing $\chi^{(3)}$ with $\chi^{(3)}(t)$. Considering the case of a high power pulsed pump laser, a cw probe laser and non-time resolved detection of signal pulses, we can derive the energy of the SRS signal directly from Eq. (2.100) by integration over the time evolution of χ'' during one laser pulse. We write the energy of the SRS signal as a function of detuning $\Delta\omega$ ($\Delta\omega = \Delta - \omega$) as

$$S_{SRS}(\Delta\omega) = B \int_{-\infty}^{\infty} dt\, \chi''(t) = \frac{B}{2i} \int_{-\infty}^{\infty} dt \left[\chi^{(3)}(t) - \chi^{(3)*}(t) \right], \qquad (4.8a)$$

which becomes, after inserting the general solution for $\chi^{(3)}(t)$ (Eq. (4.7b))

$$S_{SRS}(\Delta\omega) = \frac{AB}{2} \left[\int_{-\infty}^{\infty} dt f(t) \int_{0}^{t} d\tau f(t-\tau) e^{-\gamma\tau} e^{-i\Delta\omega\tau} \exp\left(-i\beta \int_{t-\tau}^{t} I(t')dt' \right) + c.c. \right] \qquad (4.8b)$$

where A and B are real constants and I(t) the pump laser intensity. With the help of some substitutions and an implicit Fourier transform, Eq. (4.8b) may be simplified to

$$S_{SRS}(\Delta\omega) = AB \frac{\gamma}{\Delta\omega^2 + \gamma^2} * \left| \int_{-\infty}^{\infty} dt\, f(t) e^{i\Delta\omega t} \exp\left(i\beta \int_{-\infty}^{t} I(t')dt' \right) \right|^2, \qquad (4.8c)$$

where * denotes convolution. For strong damping we use the approximate $\chi^{(3)}$ of Eq. (4.7c) and obtain

$$S_{SRS}(\Delta\omega) = AB\int_{-\infty}^{\infty} dt\ I(t)\frac{\gamma}{(\Delta\omega + \beta I(t))^2 + \gamma^2} \tag{4.8d}$$

Similarly we derive the energy of the FWMRS signal from Eq. (2.102) under the assumption of phase matching as

$$S_{FWMRS}(\Delta\omega) = C\int_{-\infty}^{\infty} dt\ \left|\chi^{(3)}(t)\right|^2, \tag{4.9a}$$

which becomes, after inserting the general solution for $\chi^{(3)}(t)$ (Eq. (4.7b))

$$S_{FWMRS}(\Delta\omega) = A^2C\int_{-\infty}^{\infty} dt\ I(t)\left|\int_0^t d\tau\ f(t-\tau)e^{-\gamma\tau}e^{-i\Delta\omega\tau}\exp\left[-i\beta\int_{t-\tau}^{t} I(t')dt'\right]\right|^2. \tag{4.9b}$$

For strong damping we insert the approximate $\chi^{(3)}$ of Eq. (4.7c) and obtain

$$S_{FWMRS}(\Delta\omega) = A^2C\int_{-\infty}^{\infty} dt\ \frac{I(t)^2}{(\Delta\omega + \beta I(t))^2 + \gamma^2}. \tag{4.9c}$$

Choosing $I(t) = I_0e^{-at^2}$, with $a = \ln 2/\delta t^2$, where δt = 3ns is the HWHM of the intensity evolution in time, in agreement with previous calculations, we may examine spectral line shapes for specific parameters γ (damping or pressure broadening) and βI_0(maximum Stark shift). We assume a uniform spatial intensity distribution for the pulsed laser and a non-degenerate molecular transition (1 = 0). Figure 4.1 (a-d) shows SRS and FWMRS spectra for γ = 0 and βI_0 = 0.1, 0.5, 1, 2 GHz, respectively.

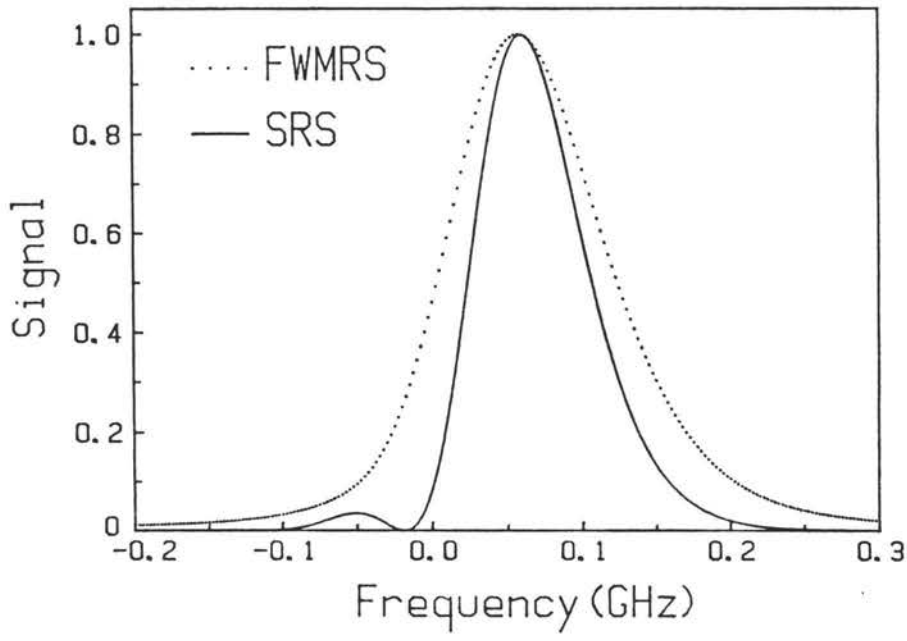

Fig. 4.1a. Phase modulated CRS spectra for an undamped oscillator ($\gamma = 0$) with a maximum Stark shift of $\beta I_0 = 0.1$GHz

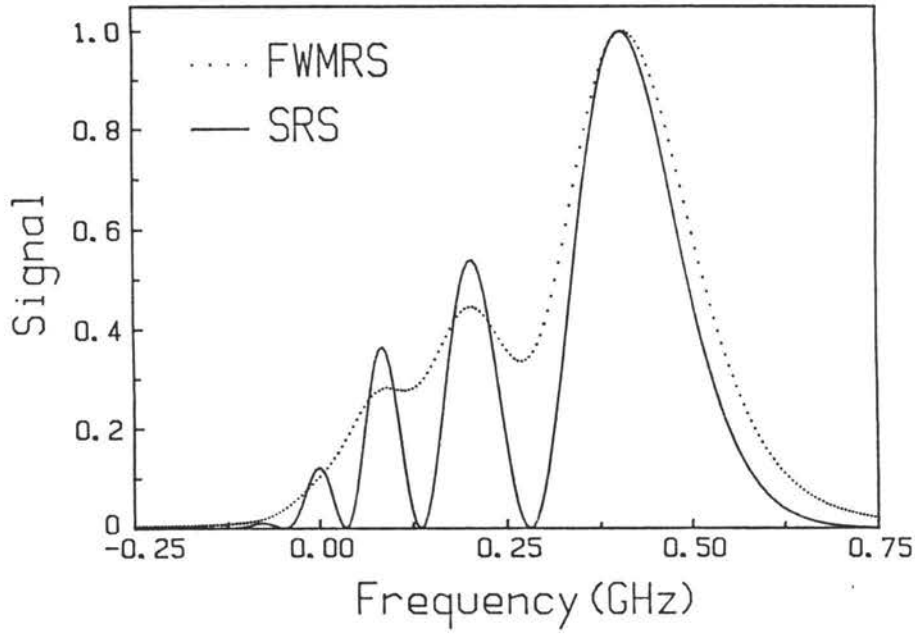

Fig. 4.1b. Phase modulated CRS spectra for an undamped oscillator ($\gamma = 0$) with a maximum Stark shift of $\beta I_0 = 0.5$GHz

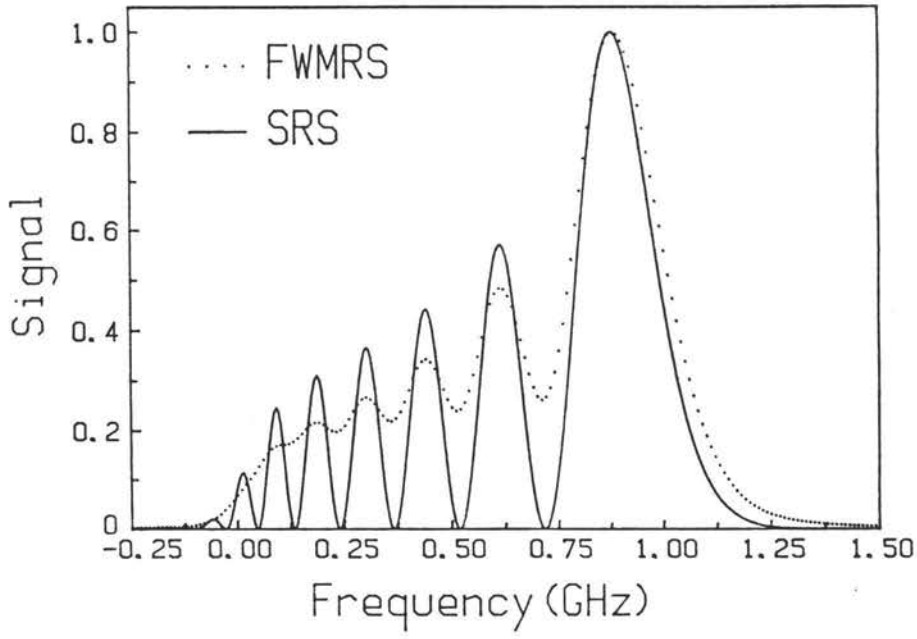

Fig. 4.1c. Phase modulated CRS spectra for an undamped oscillator ($\gamma = 0$) with a maximum Stark shift of $\beta I_0 = 1.0$GHz

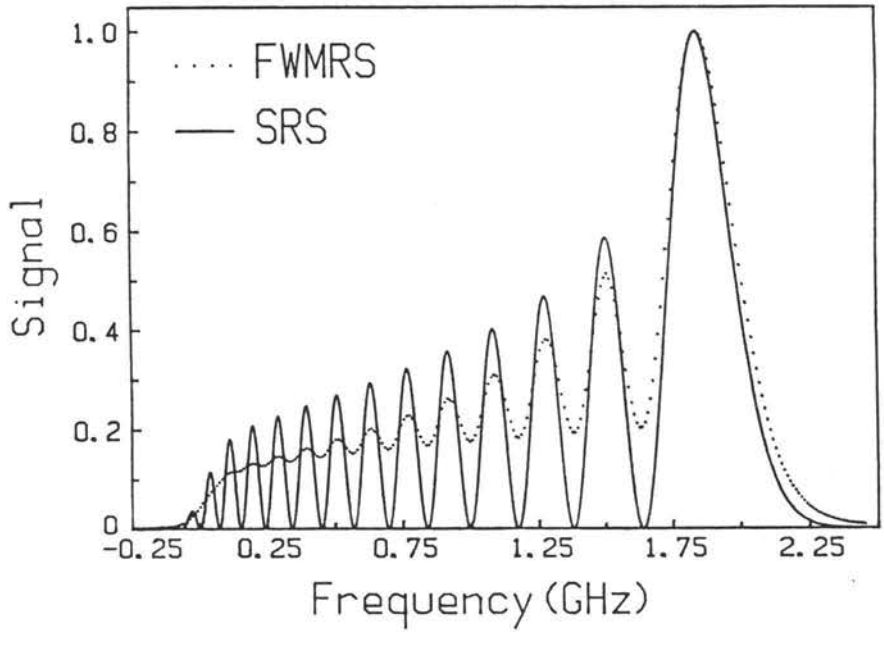

Fig. 4.1d. Phase modulated CRS spectra for an undamped oscillator ($\gamma = 0$) with a maximum Stark shift of $\beta I_0 = 2.0$GHz

In these spectra the maximum signal is produced near the maximum Stark shift βI_0. This agrees with the fact that around $t = 0$ ($I = I_0$) the intensity changes slowly, and the signal produced per unit time is highest. Furthermore the signal of an undamped oscillator ($\gamma = 0$) is strongly modulated as a function of $\Delta\omega$, due to the accumulation of Stark induced phase shift in the factor $\exp\left(i\beta\int_{-\infty}^{t} I(t')dt'\right)$. The peaks occur at identical frequencies $\Delta\omega$, for both SRS and FWMRS. The number of oscillations increases both with the maximum intensity I_0 and the width of the intensity evolution (not shown). FWMRS peaks are slightly wider than SRS peaks, which is due to Gaussian broadening (see Sect. 2.2.2) corresponding to the Fourier transform limited laser linewidth. While SRS spectra are fully modulated, the FWMRS signal has a smaller amplitude of oscillation because the real part of the phase factor is $\pi/2$ out of phase with the imaginary part, therefore flattening out minima and maxima of the oscillation for $|\chi|^2$. This is further demonstrated in Fig. 4.2, which shows, for $\gamma = 0$, $\beta I_0 = 1\text{GHz}$, a comparison of the SRS signal $S_{SRS} = B\int_{-\infty}^{\infty} dt\ \chi''(t)$, and the corresponding signal for the real part of $\chi^{(3)}$, $S_{POL} = B\int_{-\infty}^{\infty} dt\ \chi'(t)$. This signal corresponds to a polarized version of stimulated Raman spectroscopy (see Sect. 2.2.1). One clearly notes the different peak positions and zeros for the spectra of real and imaginary part of $\chi^{(3)}$. We want to

point out however, that the FWMRS signal $S_{FWMRS} = C \int_{-\infty}^{\infty} dt \left| \chi^{(3)}(t) \right|^2$ is clearly not proportional to the sum of S_{SRS}^2 and S_{POL}^2.

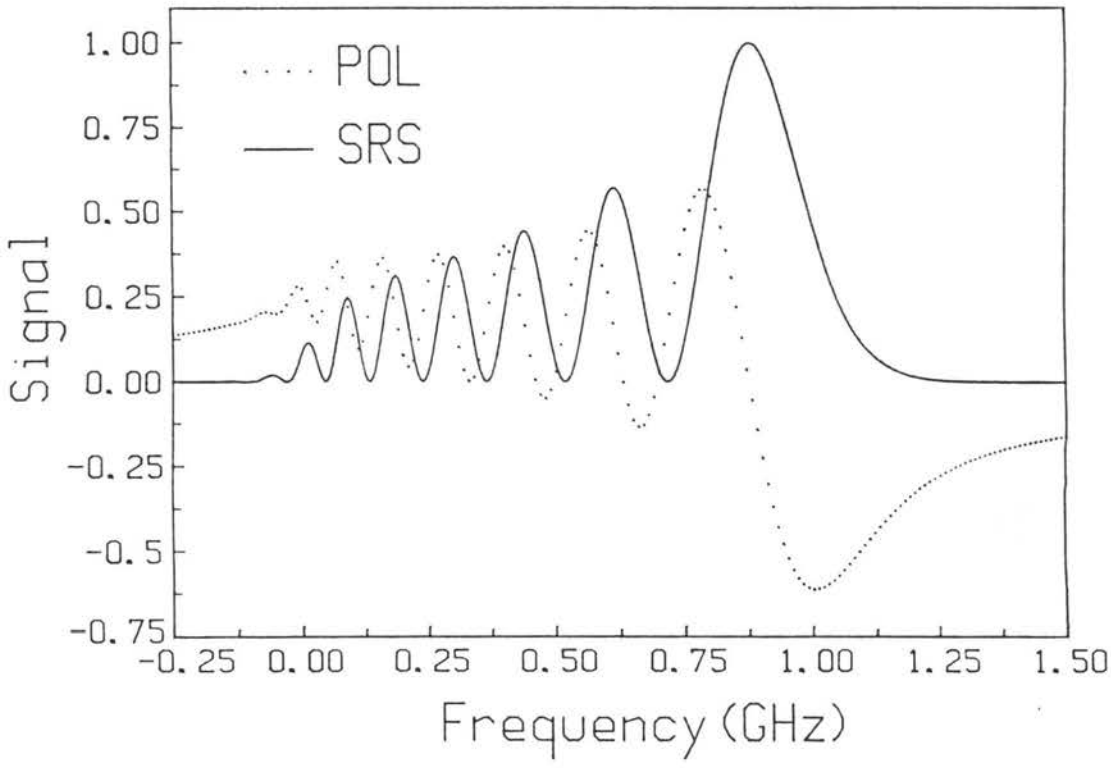

Fig. 4.2. Comparison between spectra of the imaginary (SRS, solid curve) and real (POL, dotted curve) part of $\chi^{(3)}(t)$, for a maximum Stark shift βI_0 of 1GHz and no damping ($\gamma = 0$).

The introduction of a non-zero damping constant γ into the calculation corresponds to a limitation on the accumulation of Stark induced phase shift. If we think in terms of pressure broadening, we can imagine that each collision leads to a random phase shift, the molecule literally forgets about the previously accumulated phase.

Figure 4.3a and 4.3b show this for SRS and FWMRS spectra with βI_0 = 1GHz.

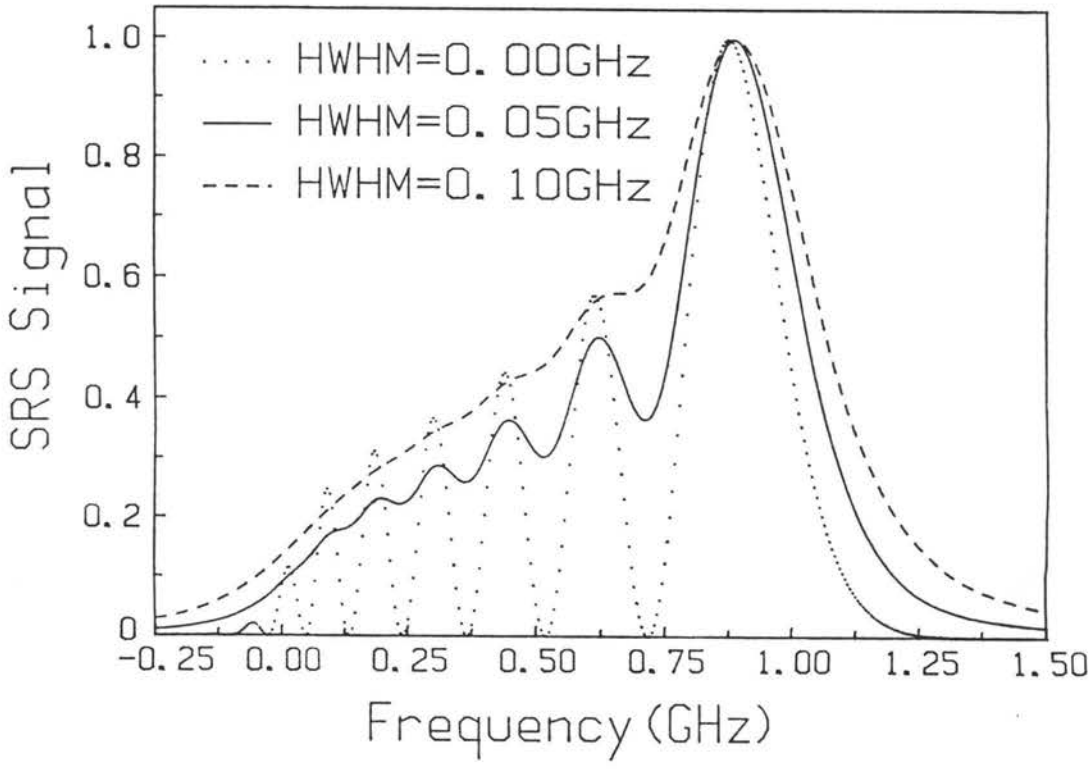

Fig. 4.3a. SRS spectra with a maximum Stark shift of 1GHz and a damping constant γ of γ = 0 (dotted curve), γ = 0.05GHz (solid curve) and γ = 0.1GHz (dashed curve)

With increasing Lorentzian broadening the phase modulation is gradually smeared out. In the case of SRS the broadened spectrum is simply a convolution of a Lorentzian and the original phase modulated spectrum, as can be seen from Eq. (4.8c). Increasing Lorentzian broadening therefore leads to a continuous overall increase in width.

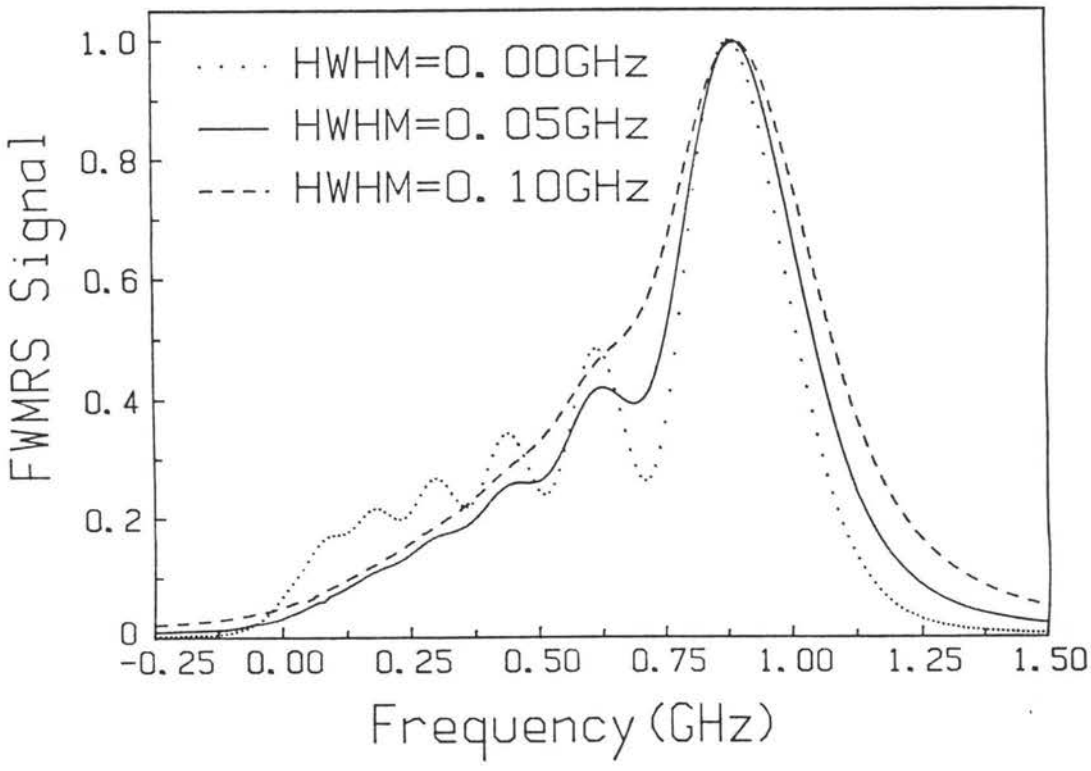

Fig. 4.3b. CSRS spectra with a maximum Stark shift of 1GHz and a damping constant γ of $\gamma = 0$ (dotted curve), $\gamma = 0.05$GHz (solid curve) and $\gamma = 0.1$GHz (dashed curve)

For FWMRS, the broadened spectrum is clearly not represented by such a simple convolution (Fig. (4.3b)). The relatively strong FWMRS signal at a small detuning $\Delta\omega$ is due to the constructive interference of χ', the real part of $\chi^{(3)}$ (Fig. (4.2)). For Lorentzian broadening this constructive interference is destroyed, leading to a decrease in overall width for small broadening (Fig. (4.3b), HWHM = 0.05GHz). For a larger HWHM the Lorentzian broadening starts to dominate and the overall width increases continually (HWHM = 0.1GHz).

Finally we compare our approximation for strong damping (Eq.'s (4.7c, 4.8d, 4.9c)) with the exact calculation (Eq.'s (4.7b, 4.8c, 4.9b)). Figure 4.4 shows a comparison between exact calculations (solid line) and approximations for both SRS and FWMRS at a Lorentzian HWHM (damping constant) of 0.1GHz and 0.2GHz.

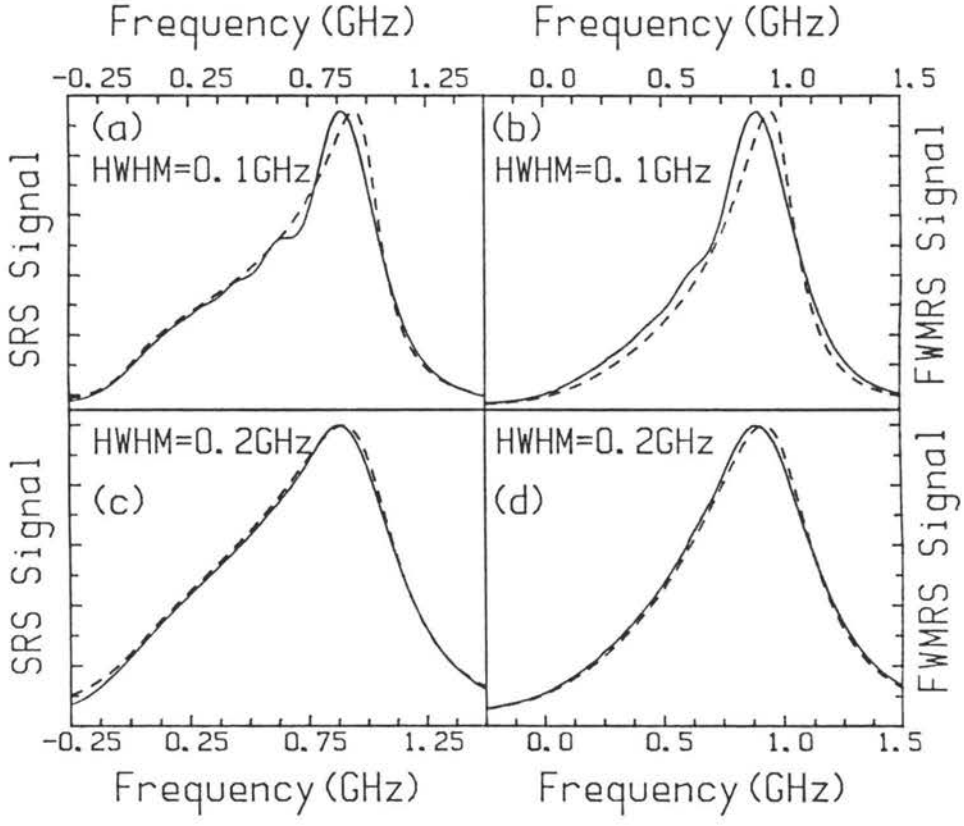

Fig. 4.4. Comparison between exact calculations (solid curves) and the approximation for strong damping (dashed curves).

(a) SRS spectra for γ = 0.1GHz.

(b) FWMRS spectra for γ = 0.1GHz.

(c) SRS spectra for γ = 0.2GHz.

(d) FWMRS spectra for γ = 0.2GHz.

At a HWHM of 0.1GHz most of the phase modulation is already averaged out and both curves show good agreement. Increasing the HWHM to 0.2GHz leads to complete agreement between the exact calculations and the approximation for strong damping. Our experimental spectra (Sect. 3.2.2) include a Lorentzian broadening of about 0.135GHz, thereby justifying the use of the strong damping approximation. In our experiments the phase modulation is averaged out even more due to strong spatial inhomogeneities, non-degenerate directional sub-levels and Doppler broadening, leading to complete agreement between approximation and exact calculation. To observe the phase modulation in an experiment the following conditions have to be fulfilled: small spatial intensity inhomogeneities, strong Raman transition without multiple sub-levels, small Doppler and pressure broadening and a Fourier transform limited pump laser. Small spatial inhomogeneities may be realized with an experimental scheme introduced by L. Rahn et. al [4.2], which uses different beams as pump beam and as a source of the Stark field. Strong non-degenerate transitions may be found in H_2 and D_2, where the molecular $l = 0$ level is strongly populated. Doppler and pressure broadening can be minimized by working at low temperature and pressure. Finally a Fourier transform limited high power pump laser has recently become commercially available with the introduction of an injection locked Nd-Yag lasers. While all these conditions can be fulfilled, the experiment has to be carefully designed in order to observe the Stark induced phase modulation in coherent Raman spectroscopy.

4.2 Contributions of $\chi^{(5)}$ to the FWMRS signal

In section 2.2 we have expanded the susceptibility χ in terms of the electrical field as (Eq. 2.67)

$$\chi = \chi^{(1)} + \chi^{(2)}E + \chi^{(3)}E^2 + \chi^{(4)}E^3 + \chi^{(5)}E^4 + \ldots,$$

where all even χ terms are zero for a medium with inversion symmetry, such as a gas. While we have previously shown that $\chi^{(3)}$ is the lowest order contributor to the FWMRS signal (Sec. 2.2.1), we have not examined any higher order contribution. In this section we estimate the contribution of the fifth order susceptibility $\chi^{(5)}$.

The general theoretical expression for $\chi^{(3)}(\omega_1,\omega_2,\omega_3)$ may be written as [4.3]

$$\chi^{(3)}_{ijkl} = \frac{1}{4\pi\epsilon_0}\frac{N}{3!\,h^3}\sum_{abcd}\frac{R^i_{ab}R^j_{bc}R^k_{cd}R^l_{da}}{(\omega_{ba}-\omega_1-\omega_2-\omega_3)(\omega_{ca}-\omega_2-\omega_3)(\omega_{da}-\omega_3)}, \qquad (4.10)$$

where the R's are the transition matrix elements between the levels a,b,c,d, the ω's are the respective frequencies and the damping constants have been neglected. This expression can be pictured as a sum over 24 non-time-ordered single-sided Feynman diagrams, or more correctly a sum over 48 time-ordered double-sided Feynman diagrams [4.4]. In the case of two-beam FWMRS, a and c are the levels of the Raman transition, $\omega_1 = \omega_3 > 0$, $\omega_2 < 0$ and the second term in the denominator determines the Raman resonance. In this case only the four double-sided diagrams shown in Fig. 4.5 result in a Raman resonance and contribute significantly to the FWMRS signal. Using the rather crude approximations

$$R = R^i_{ab} = R^j_{bc} = R^k_{cd} = R^l_{da}, \qquad (4.11a)$$

$$\omega_{nr} = \omega_{ba} - \omega_1 - \omega_2 - \omega_3 = \omega_{da} - \omega_3, \qquad (4.11b)$$

and the identity

$$\omega_r = \omega_{ca} - \omega_2 - \omega_3, \tag{4.11c}$$

we may write Eq. (4.10) for FWMRS as

$$\chi^{(3)}_{ijkl} = \frac{4}{4\pi\epsilon_0} \frac{N}{3!\, h^3} \frac{R^4}{\omega_r \omega_{nr}^2}, \tag{4.11d}$$

where the factor 4 comes from the summation over the four diagrams.

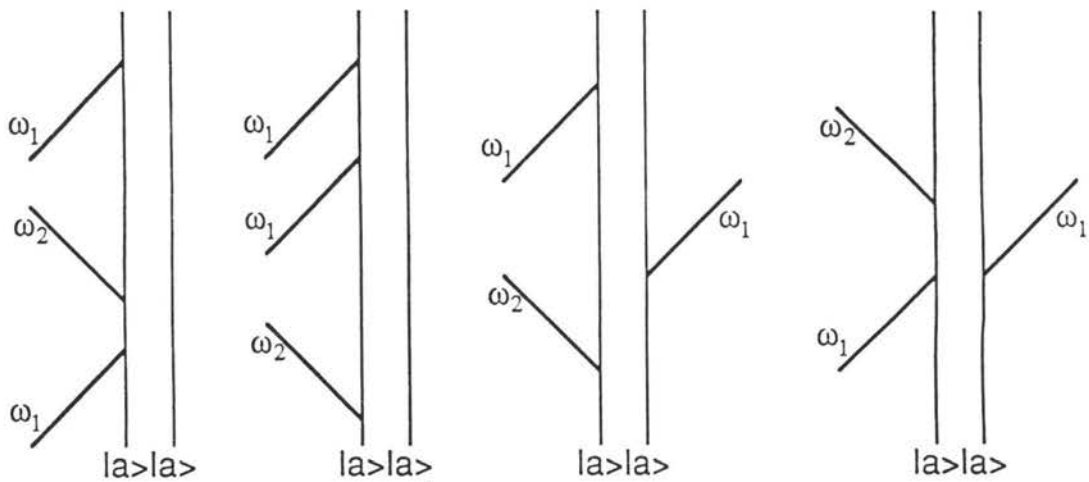

Fig. 4.5. Double-sided time-ordered Feynman diagrams of third order nonlinear processes which contribute significantly to the FWMRS signal

Comparing this expression with Eq. (2.90d), which expresses $\chi^{(3)}$ in terms of the transition polarizabilities $a^{v}_{v'}$, we can calculate $R^2/(h\omega_{nr})$ for the $v = 0 \rightarrow v = 1$ vibrational Q-branch in N_2, using the values of a^0_1 given in table 2.2 and identifying ω_r with $\Delta\omega - i\gamma$, as

$$\frac{R^2}{h\omega_{nr}} = 3^{1/2}\pi\, \epsilon_0\, a^0_1 = 3.3\ 10^{-41}\ \frac{C^2 m^2}{J}. \tag{4.12}$$

Similar to $\chi^{(3)}$, we can express $\chi^{(5)}$ in double-sided Feynman diagrams. Only four of them (Fig. (4.6)), which correspond on a one-to-one basis to the $\chi^{(3)}$ diagrams in Fig. (4.5), result in $\chi^{(5)}$ terms with an additional resonance denominator and contribute significantly to FWMRS. Essentially we have added a Rayleigh interaction to the upper Raman level c, as can be seen from a comparison of Fig. (4.5) with Fig. (4.6).

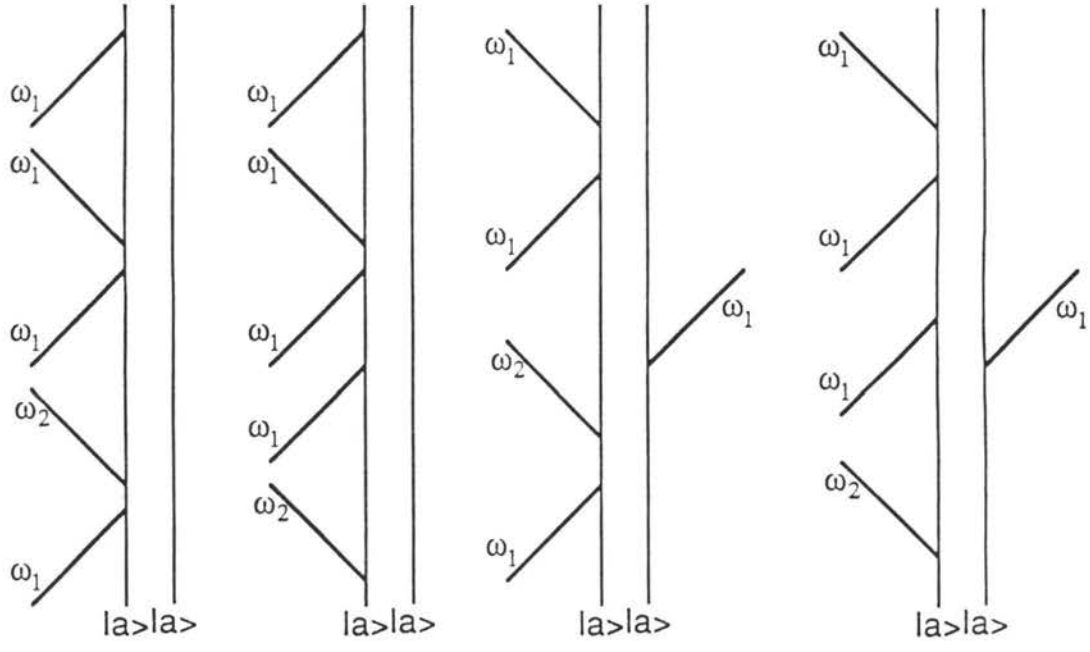

Fig. 4.6. Double-sided time-ordered Feynman diagrams of fifth order nonlinear processes which contribute significantly to the FWMRS signal

Using the approximations of Eq. (4.11) we write the part of $\chi^{(5)}$ which contributes to the FWMRS signal as

$$\chi^{(5)}_{ijkl} = \frac{4}{4\pi\epsilon_0}\,\frac{N}{5!\,h^5}\,\frac{R^6}{\omega_r^2\,\omega_{nr}^3}. \tag{4.13}$$

With the help of Eq. (2.67) the nonlinear susceptibility relevant to FWMRS becomes

$$\chi = E^2\chi^{(3)}\left(1 + \frac{|E|^2}{20h\omega_r}\,\frac{R^2}{h\omega_{nr}}\right), \tag{3.14a}$$

which may be rewritten with the help of Eq. (2.32b) as

$$\chi \sim I\chi^{(3)}\left(1 + A\,\frac{I}{\omega_r}\right), \tag{3.14b}$$

with $A = \frac{1}{10c\,\epsilon_0 h}\,\frac{R^2}{h\omega_{nr}} = 1.9\ 10^{-6}\,\frac{m^2}{J} = 1.9\,\frac{mm^2}{J} = 1.9\,\frac{GHz\ mm^2}{GW}$ (3.14c)

for the vibrational Q-branch of molecular nitrogen. This equation provides a theoretical justification for using Eq. (3.11) in section 3.2.2.3. The theoretically evaluated A is within one order of magnitude of the experimental value of $0.3mm^2/J$. Taking the crudeness of our approximations into account, the agreement is rather good and it further supports our suggestions about the influence of $\chi^{(5)}$ on FWMRS, made in section 3.2.2.3.

References Chapter 4

4.1 M. Péalat, M. Lefebvre, J.-P.E. Taran, and P.L. Kelley, "Sensitivity of Quantitative Vibrational CARS Spectroscopy to Saturation and Stark Shifts," Phys. Rev. A (to be published).

4.2 L.A. Rahn, R.L. Farrow, M.L. Koszykowski and P.L. Mattern, "Observation of an Optical Stark Effect on Vibrational and Rotational Transitions," Phys. Rev. Lett. **45**, 620 (1980).

4.3 P.N. Butcher, Nonlinear Optical Phenomenon, (Ohio State University Press, Columbus, 1965), p.80.

4.4 Y. Prior, "A Complete Expression for the Third-Order Susceptibility ($\chi^{(3)}$) - Pertubative and Diagrammatic Approaches," IEEE J. Quantum Electron. **QE-20**, 37 (1984).

Chapter 5

Conclusions

5. Conclusions

With our theoretical and experimental investigations, we have made progress in the understanding of coherent Raman spectroscopy (CRS) line shapes for both low and high laser intensities in the interaction region. The line shapes of the two most important CRS's, stimulated Raman spectroscopy (SRS) and four-wave mixing Raman spectroscopy (FWMRS) have been compared in detail, using a novel experimental setup capable of utilizing both spectroscopic techniques simultaneously.

At low laser intensities we have studied the influence of inhomogeneous (Doppler) broadening on both spectroscopies. The confusion about which of the two spectroscopies is broadened more by Doppler broadening, as evident in earlier works, has been unambiguously resolved by our experiments. Our experiments have shown clearly that FWMRS has broader spectral lines than SRS, which is in perfect agreement with our theoretical analysis. Nonetheless, there is a need for future experiments to quantitatively determine the ratio of SRS and FWMRS linewidths as a function of the ratio of homogeneous (pressure) and inhomogeneous (Doppler) broadening. A theoretical prediction of this function appears in section 2.2.2 (Fig. (2.7)). Repeating our experiments on molecular hydrogen at different

temperatures and pressures would be an ideal test. The low mass of hydrogen molecules leads to both strong Doppler broadening at moderate temperatures and widely spaced vibrational rotational Raman lines which reduces the undesirable interference of neighboring lines for this test.

Furthermore, we have investigated the influence of neighboring lines on both types of CRS's. Both experiment and the previously well known theory have been shown to be in good agreement. FWMRS line shapes are influenced much more by neighboring lines than those of SRS. This is due to the influence of the real part of the third order nonlinear susceptibility χ' on FWMRS but not on SRS. Due to the slowly decaying influence of neighboring χ's, FWMRS peaks are shifted away from the main concentration of strong Raman transitions.

From these results it becomes clear that the use of SRS for high-resolution measurements of peak positions, linewidths and line shape is more straightforward and has less potential for systematic errors. On the other hand, there may be situations where the larger influence of neighboring lines on the FWMRS spectrum can be used advantageously for diagnostic purposes, for example temperature measurements.

At high laser intensities, we have studied the influence of optical Stark effect, due to the high pump laser intensity in focused Gaussian beams, on both types of CRS's. For the theoretical calculation of Stark broadened spectra, we have developed a new theory of FWMRS signal generation in Gaussian beams. This theory and the respective theory for SRS, which is well known, have then been combined with our calculation of Stark coefficients and transition

strengths for the individual orientational sublevels in N_2, to yield theoretical Stark broadened line shapes for both SRS and FWMRS. Experimentally we have rapidly alternated between the simultaneous measurement of SRS and FWMRS spectra at low (mild focusing) and high (tight focusing) pump laser intensities. This alternation together with a sophisticated frequency reference scheme has enabled us to make a rather direct comparison between Stark broadened and non-Stark broadened spectra.

The experimental results show a very small peak shift for FWMRS and a larger peak shift in the order of 10% of the maximum Stark shift, βI_0, for SRS. The wings of the Raman lines are very asymmetrically broadened in the direction of the theoretical Stark shift for both CRS's. This asymmetric wing is somewhat more pronounced for SRS than for FWMRS, where it shows a characteristic kink. The SRS results are in excellent agreement with our theory, while the FWMRS results show only partial agreement with the theory. We suspect two reasons for the discrepancy. First, FWMRS spectra are more susceptible to deviations of our pump laser beam from the ideal Gaussian shape in time and space, which has been assumed in the theory. Second, we have analysed a potential contribution of the fifth-order nonlinear susceptibility $\chi^{(5)}$ to the FWMRS signal and show that its inclusion leads to an improved agreement between experiment and theory. This possibility should motivate further experiments, specifically designed to test the contribution of $\chi^{(5)}$ to FWMRS signals.

Additionally, we have theoretically analysed the occurrence of a new kind of phase modulation, which is induced by rapid Stark tuning

of the molecular transition frequency. We show that this modulation is stronger for SRS than for FWMRS. Our analysis of the influence of homogeneous broadening on the phase modulation shows that while the broadening process is more complicated for FWMRS than for SRS, sufficient broadening will average out the effect of phase modulation in both SRS and FWMRS spectra, making it unobservable for our experimental conditions. This leaves the possibility of actually observing this new effect to future experiments.